A Transfer to the Continuum formalism for the study of (p, pn) and $(p, 2p)$ reactions on unstable nuclei

PhD thesis

Mario Gómez Ramos

Departamento de Física Atómica, Molecular y Nuclear
Universidad de Sevilla

October 2018

A Transfer to the Continuum formalism for the study of (p, pn) and $(p, 2p)$ reactions on unstable nuclei

(Un formalismo de Transferencia al Continuo para el estudio de reacciones (p, pn) y $(p, 2p)$ sobre núcleos inestables)

Memoria para optar al título de Doctor en Física Nuclear

Mario Gómez Ramos

Dirigida por el Doctor

D. Antonio Matías Moro Muñoz

Departamento de Física Atómica, Molecular y Nuclear
Universidad de Sevilla

Octubre 2018

A mi familia, en todas sus acepciones

Agradecimientos

Este documento es el resultado de un proyecto desarrollado durante cuatro años, o incluso cinco, contando con el primer año de máster, que me sirvió como introducción al mundo de la investigación. Que sólo mi nombre aparezca en la portada de esta memoria de tesis no hace justicia al gran número de personas que lo han hecho posible, por su apoyo académico, profesional y/o personal. Espero que los siguientes párrafos sirvan como una muestra de reconocimento a este apoyo, si bien incompleta en el número de personas que aparecen y en la contribución que se les reconoce.

Mis agradecimientos no pueden sino comenzar con mi director de tesis, Dr. Antonio M. Moro Muñoz, sin el cual este trabajo no habría sido posible. Su contribución va más allá de la meramente académica, esencial para el desarrollo de este trabajo, extendiéndose a una paciente labor como mentor en el extraño mundo de la investigación, con una dedicación y disponibilidad más allá de lo razonable, que a la pregunta "¿Tienes tiempo?" siempre respondía con un "Bueno dime", aun cuando la respuesta objetiva fuera un rotundo "No".

Este agradecimiento debe extenderse a todo el departamento, en el que he encontrado un excelente ambiente en el que afrontar esta nueva etapa. Aunque objetivamente son los miembros más "senior" del departamento aquellos que más me han aportado, en términos de experiencia y consejos, debo hacer una mención especial a todos los compañeros doctorandos con los que he compartido la experiencia predoctoral. He tenido la fortuna de coincidir durante estos cuatro años con multitud de colegas, en los que he visto reflejadas mis dudas y esperanzas, alegrías y frustraciones. Sin duda, en esta guerra que es la obtención del título doctoral, una de las facetas más positivas es la camaradería que se forma en las trincheras, extendida también a aquellos que aun habiendo terminado su batalla aún recuerdan el olor de

la pólvora.

Durante estos cuatro años, he tenido la oportunidad de realizar dos estancias en el extranjero, una en el centro RCNP de la Universidad de Osaka, Japón, supervisada por el Dr. K. Ogata, y otra en la Universidad de Surrey, supervisada por la Dra. N. Timofeyuk. Ambas estancias me han permitido explorar regiones nuevas, tanto físicamente como en el mundo de la física nuclear, y probablemente hayan sido de los periodos más fructíferos en el ámbito formativo. Tanto al Dr. Ogata como a la Dra. Timofeyuk les estoy inmensamente agradecido por su acogida y su dedicación durante estas estancias.

También aprovecho esta oportunidad para agradecer a los doctores A. Deltuva, K. Yoshida, K. Ogata, L. Atar y P. Díaz Fernández, que han proporcionado cálculos y resultados que se presentan en esta memoria de tesis, por permitirme usar sus resultados y por las fructíferas discusiones asociadas a ellos.

En el ámbito económico, este proyecto ha estado financiado por la beca de Formación de Profesorado Universitario, otorgada por el pasado Ministerio de Educación, Cultura y Deporte. Este programa de becas es una de las fuentes de financiación para investigación predoctoral en ciencia fundamental más fiables y establecidas sin el cual la carrera de cientos de investigadores cada año se vería arrancada de raíz. Dados los probados beneficios de la investigación para la sociedad, programas como este deben verse apoyados, manteniendo si no incrementando el número de becas, siendo la responsabilidad de los beneficiarios el honrar la confianza inherente a esta inversión con dedicación y trabajo duro.

Descendiendo a un plano más personal, tengo que agradecer a mi familia por su apoyo en todos los planos: económico, personal, anímico... Es gracias a ellos, en particular a mis padres, que he podido llegar a presentar este documento superando dificultades y dudas que sin su ayuda me habrían parecido insuperables. A lo largo de estos años ha habido muchas situaciones en las que no les he demostrado el agradecimiento y reconocimiento que se merecían. Espero que estas líneas compensen un poco esta falta.

Unas últimas palabras las tengo que dedicar a los amigos que me han acompañado estos años (los que haya mencionado antes ya tenéis vuestro párrafo, no seáis avariciosos), soportando las ausencias y desplantes que resultan de la dedicación a la labor investigadora, y a la paciencia que han

demostrado ante las quejas y plañidos propios del estudiante predoctoral. En especial, tengo que agradecer a Silvia y José, que han estado conmigo desde mucho antes de empezar esta aventura, dándome muchos momentos inolvidables que han acompañado los éxitos y paliado los desencantos de esta etapa. Su confianza ciega en mí y mis capacidades ha supuesto un apoyo férreo cuyo inmenso valor sólo he sido capaz de valorar en retrospectiva. Gracias de verdad.

Es probable que haya muchos que no se hayan visto reflejados en estas líneas y que aun así merezcan un reconocimiento por su aporte en el proceso que ha llevado a producir esta memoria. También a ellos debo darles las gracias y pedirles perdón por no encontrar la destreza para mostrar un agradecimiento más explícito.

Mario

Octubre 2018

Abstract

In this work, a new formalism, the Transfer to the Continuum, is developed for the description of $(p, 2p)$ and (p, pn) reactions. The motivation behind its development lies in a renewed interest in the nuclear physics community on this kind of reactions, which has materialized in recent experimental campaigns devoted to them. Apart from the marked spectroscopic utility of nucleon removal (p, pN) reactions, one of the main reasons behind this revival of such reactions can be found in the open problem of the asymmetry dependence of the "quenching factors" which resulted from systematic campaigns of nucleon knockout with heavy targets at medium energies performed in the late 90s and early 2000s. The contested results found for these reactions claimed for clearer reactions with better-understood mechanisms, such as (p, pN) reactions.

However, the traditional description of (p, pN) use similar approximations to those used in the description of heavy-target nucleon knockout. A different treatment, avoiding these approximations, is desirable to obtain robust results with which to tackle this open problem. Such a treatment is developed in this work, extending the coupled-channel methods used at low energies, for which the nuclear physics group at the University of Seville has developed a renowned expertise. It provides not only a robust standalone method to study (p, pN) reactions but also a testing ground for the assumptions on the reaction mechanism used in other descriptions of (p, pN) processes.

A description of the state of the art on (p, pN) reactions as well as on the "quenching-factor" problem is given in Chapter 1, as well as a brief description of other methods used to describe these reactions. The new Transfer to the Continuum formalism is described in Chapter 2, devoting special interest to the modifications that must be introduced in standard coupled-channel

formalisms and codes in order to properly describe (p, pN) reactions, which mostly relate to the inclusion of relativistic effects. Chapter 3 presents some benchmark calculations performed with other reaction theories used in the literature to describe (p, pN) reactions, which serve both as a test of the new formalism and as an exploration on the assumptions included in it as well as the compared reaction models. Chapter 4 presents comparisons to experimental results, with the main interest being the asymmetry dependence of the obtained "quenching factors", which is studied systematically for all recently published data on (p, pN) reactions. Apart from this main topic, momentum distributions are presented as a test of the adequacy of the treatment of the reactions. Reactions at lower energies are also studied to showcase the applicability of the method at those low energies. Finally, Chapter 5 extends the formalism to reactions with Borromean nuclei, which allow for the study of unbound systems, exploring the interesting but elusive nucleon drip-lines. Results of the study of the $^{11}\mathrm{Li}(p, pn)^{10}\mathrm{Li}$ reaction are presented, showing the necessity of a solid reaction formalism for the obtention of reliable information on the structure of unbound nuclei such as $^{10}\mathrm{Li}$. The conclusions of this work are summarized in Chapter 6.

Contents

List of Figures

List of Tables

Chapter 1

Introduction

Every new beginning comes from some
other beginning's end

Seneca

The present work focuses on the development of a new reaction formalism for the analysis of recent (p, pn) and $(p, 2p)$ reactions performed in inverse kinematics on stable and unstable nuclei. In this introductory chapter, a historical review of (p, pn) and $(p, 2p)$ reactions will be presented, along with other closely related nucleon knockout reactions, such as $(e, e'p)$, highlighting the nuclear properties that can be extracted from them and the nuclear structure models used to predict them. The closely-related open question of the dependence of the "quenching factors" on proton-neutron asymmetry will also be introduced. Finally, other formalisms used in the literature for the study of (p, pn) and $(p, 2p)$ will be briefly described.

1.1 Background

The atomic nucleus is an exquisitely complex quantal system formed by a mesoscopic number of strongly-interacting fermions bound together by the strong nuclear force, but which also feel strongly the electromagnetic and weak nuclear forces. As such, its description escapes the perturbative and statistical tools that are so fruitful in other fields of physics.

Given its complexity, it is rather remarkable that the rather simple nuclear shell model [1], developed in the 40s and 50s by several physicists, such

as E. P. Wigner, M. G. Mayer and H. D. Jensen, gives a good prediction for a large number of nuclei of nuclear properties such as the angular momentum and parity of the ground and excited states, as well as their binding energies. Perhaps, the most notorious and defining prediction of the nuclear shell model is the existence of nuclear "magic numbers": numbers of proton and neutrons with deeper binding energies than those in their surroundings.

In its simplest version, the Independent Particle Model (IPM), the nuclear shell model describes nucleons as independent particles embedded in a mean field, which populate the energy levels of this field following Pauli exclusion principle. As such, magic numbers indicate the number of nucleons which fill groups of levels which are relatively close in energy (See Fig. 1.1) and the occupancy of each level is determined by the angular momentum j associated to that level, leading to an occupation number of $(2j + 1)$. For more sophisticated models, the occupation number of each level is no longer simply $(2j + 1)$ and is expressed through the spectroscopic factor (SF) of the level. We leave a more precise definition of SF for Chapter 2.

This mean-field approach is not unlike the one used to describe the behaviour of electrons in the atom, but is more questionable in the nuclear case. In the nucleus, the particles which generate the mean field are also those which populate the energy levels. As such, it is their interactions among themselves the ones generating the mean field, which at a first glance seems antithetical with the assumption that they behave independently. An assumption must be made that each nucleon interacts with the rest of the nucleus through an average interaction, the mean field, without being too sensitive to the particular properties of the other nucleons.

Such an assumption is rather questionable for the atomic nucleus, specially given the strength of the nucleon-nucleon interaction at short distances. Therefore, it needs to be tested against experimental data to assess its validity. Given the IPM deals with independent particles, the best features of the nucleus to be related to it are the single-particle properties, those describing the behaviour of only one of the nucleons in the nucleus, usually the most loosely bound, which is experimentally more easily explored.

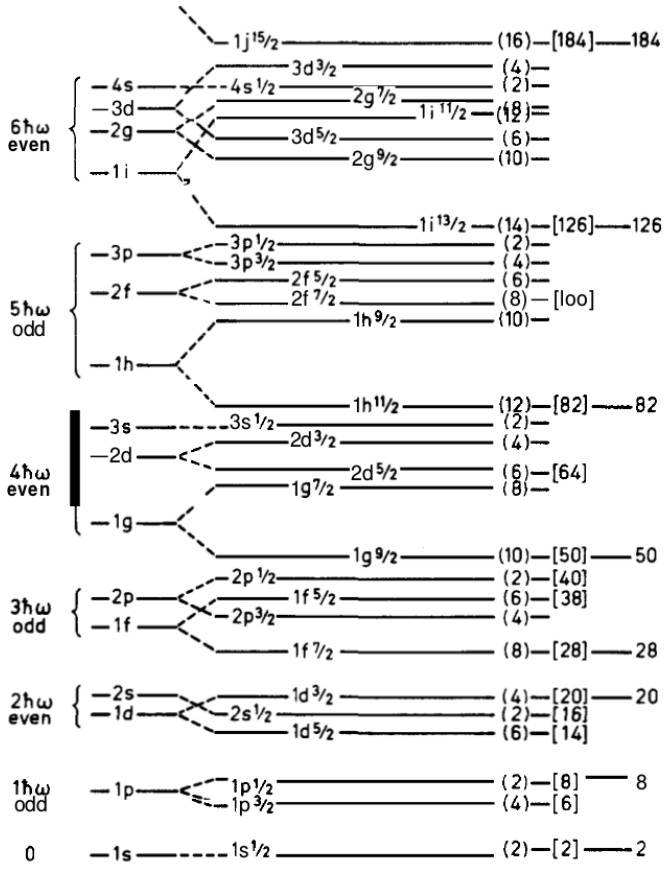

Figure 1.1: Sequence of single-particle orbitals. Figure from [2].

1.1.1 Nucleon removal reactions: $(e, e'p)$ and $(p, 2p)$

Since the very discovery of the atomic nucleus by the experiment conducted by Geiger and Marsden in 1909, nuclear reactions have proven to be an excellent probe to test the properties of the nucleus. For single-particle properties, this keeps being the case, with nucleon removal reactions being the tool of choice for their study for several decades. In nucleon removal reactions a projectile impinges in the nucleus of interest (with A nucleons) and removes one of the nucleons of the nucleus, leaving a residual nucleus (core) from whose properties (energy and momentum) information about the removed nucleon can be inferred.

This is best shown assuming quasi-free scattering (QFS). This is an approximation in which the projectile is assumed to interact only with the

removed nucleon, with both projectile and nucleon separating from the core without modifying its state of motion. With this assumption, we can envision the target nucleus A as being composed by the struck nucleon N and the core C, $A = N + C$. In the laboratory system, where A is at rest, if N has a momentum $\mathbf{p}_N$ "inside" A, core C must have the opposite momentum $\mathbf{p}_C = -\mathbf{p}_N$ to have A be at rest. Therefore, after the reaction, since C does not change its state of motion, by measuring $\mathbf{p}_C$, we can recover $\mathbf{p}_N$, the momentum of the nucleon inside A, so the momentum distribution of the outgoing core can be related to the wavefunction of the removed nucleon in momentum space. Fig. 1.2 shows a schematics of the process.

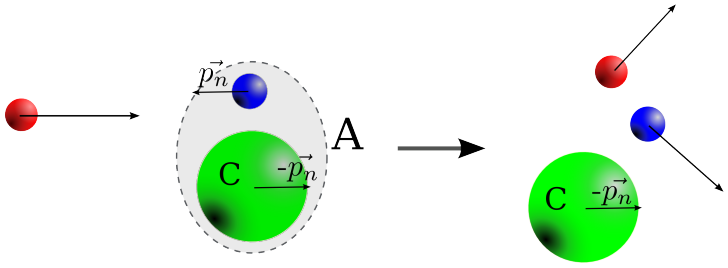

Figure 1.2: Description of the (p, pN) process in the quasi-free picture. Note that the momentum of the core C is not altered during the reaction.

From this momentum distribution (or any observable that can be related to it through conservation of energy and momentum), information can be extracted from experimental data that can be compared to nuclear structure models through a single-particle reaction calculation. The single-particle prediction is computed assuming that exactly one nucleon is removed from a definite nuclear level. The shape of the prediction as a function of angle, energy or momentum is usually very sensitive to the quantum numbers defining the level, in particular its orbital angular momentum, as can be seen in Fig. 1.3 for the core momentum distributions of a (p, pn) reaction.

Within the simple assumption that the reaction takes place by removing the nucleon from the corresponding level without changing the rest of the nucleus, the cross section for the removal will be proportional to the occupation number of the level (loosely speaking, the spectroscopic factor SF), which can then be extracted as the ratio between the total cross section and the single-particle one:

$$SF = \frac{\sigma_{exp}}{\sigma_{sp}}. \tag{1.1}$$

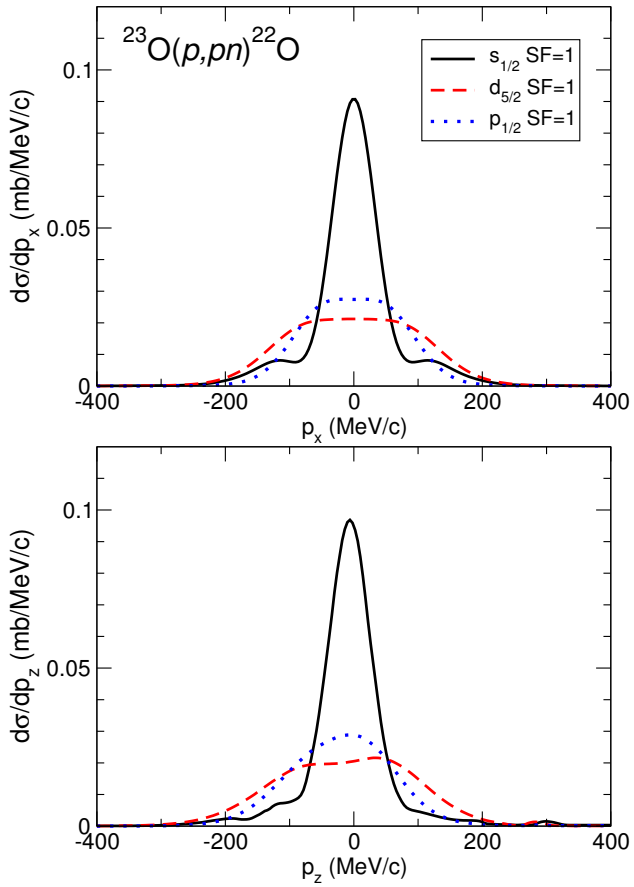

Figure 1.3: Single-particle transversal (top) and longitudinal (bottom) momentum distributions for $^{23}\mathrm{O}(p,pn)^{22}\mathrm{O}$ computed for the removal of a neutron from different nuclear levels. Figure from [3].

Let us highlight here the multiple assumptions involved in this formula: the reaction is assumed to remove a nucleon only from the least bound level, without affecting the rest of the nucleus, whose structure does not influence the reaction, except by setting the number of nucleons in the least-bound level, from which they may be removed.

Of course, the QFS picture described above for nucleon removal reactions is too simplistic and flat-out inconsistent, since it assumes no interaction between the outgoing N and C, although this interaction has to exist to bind them into A in the first place. However, it indicates which features an experiment must show in order for information on the removed nucleon to be clearly extracted. The main of this features is the minimization of the interaction between the projectile and the core, while keeping a strong

interaction between projectile and nucleon. This criterion suggests the use of light projectiles, whose interactions with the core are expected to be less intense than those of heavier projectiles.

Another feature that should be required is the minimization of the interaction between the outgoing nucleon and the core. This favours experiments with a beam energy of hundreds of MeV, for which the nucleon-nucleon interaction presents a minimum, as can be seen in Fig. 1.4. At these energies, the mean free path of the outgoing nucleon in nuclear matter is maximal, so the effects of its interaction with the core should be minimized. This condition also imposes a degree of peripherality to the reaction, since nucleons removed from the interior of the nucleus will have to cover a larger distance on their "way out" of the nucleus, which make nucleon-core interactions more likely.

These features make $(e, e'p)$ and (p, pN) (N being either a proton or a neutron) reactions at hundreds of MeV an excellent probe to study single-particle of nuclei. $(e, e'p)$ reactions present a smaller interaction between electron and core (smaller distortion), since only the electromagnetic interaction will take place between them, but at the same time the interaction between electron and proton is small, so the overall cross section will be reduced. As such, $(e, e'p)$ reactions require beams with high luminosity which can only be achieved in reactions with stable targets.

On the other hand, (p, pN) reactions have stronger distortion effects, but the strong nuclear interaction between the incoming proton and the removed nucleon provides a larger cross section.

In cases with high enough statistics, distortion effects can be further reduced by performing exclusive measurements, keeping fixed the angles and/or energies of the outgoing projectile and nucleon, selecting a geometry for which the QFS condition is best fulfilled. We note that, if both projectile and removed nucleon are detected, it is not necessary to measure the core, since its momentum and energy are conditioned by conservation laws. Of course, the detection of the core serves as a validation of the reaction mechanism.

From as early as the 1960s, exclusive measurements of $(e, e'p)$ [5] and $(p, 2p)$ [6] reactions have been performed to extract information on single-particle properties of stable nuclei, with experiments still being carried out to this day, with a special focus on nucleon removal from deep levels [7].

In the comparison of the results from these experiments to the IPM, it

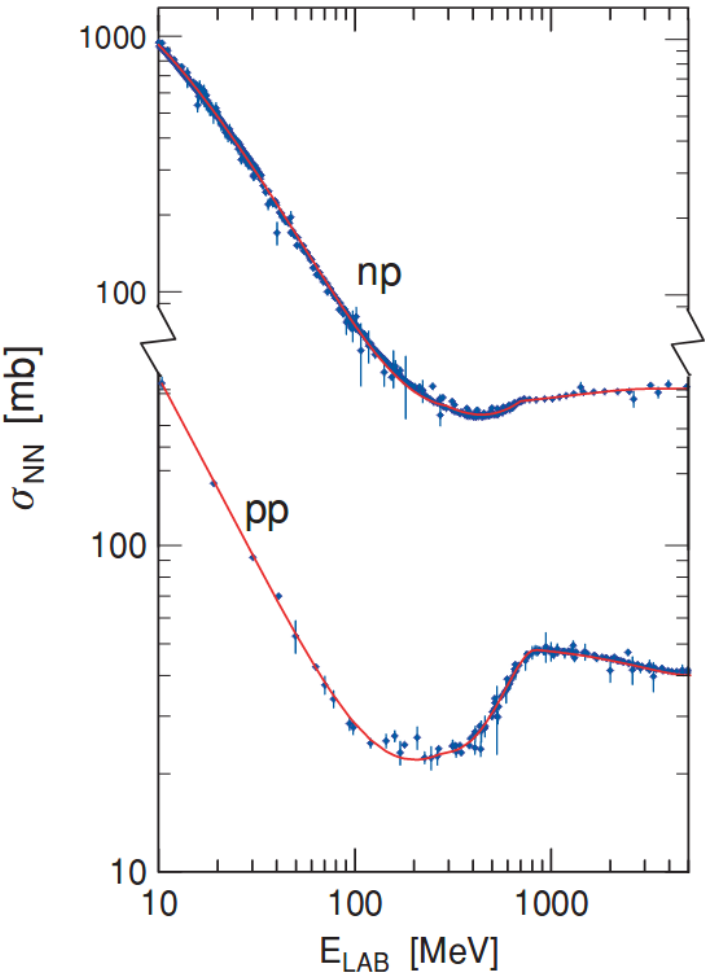

Figure 1.4: Nucleon-nucleon cross section as a function of projectile energy. Notice the minimum at hundreds of MeV. Figure taken from [4].

was found that the model was successful in predicting the ordering of nuclear levels. However, the occupation of the levels was found to be smaller than the $(2j+1)$ value predicted by the IPM by 30-40% in a systematic study for $(e, e'p)$ reactions [8] (see Fig. 1.5), leading to a "quenching factor" (the ratio between experimental and theoretical cross sections, $R_s = \frac{\sigma_{exp}}{\sigma_{th}}$) of 0.6-0.7.

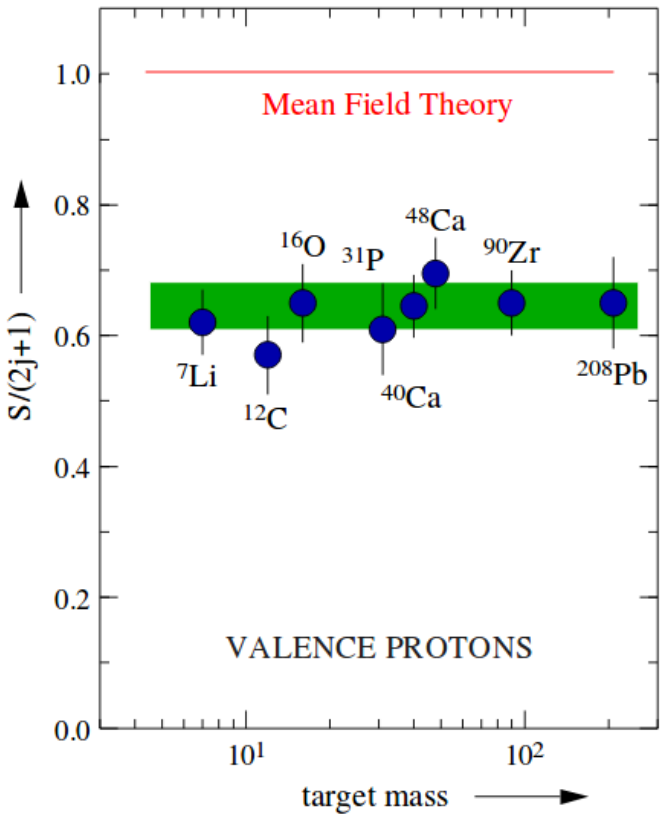

Figure 1.5: "Quenching factors" compared to IPM as a function of the nucleus mass, obtained from $(e, e'p)$ reactions [8]. Figure taken from [9].

1.1.2 Nucleon-nucleon correlations and nuclear structure models

This "quenching" of the occupation numbers when compared to the IPM has been consistently reproduced in other "single-nucleon" reactions, such as transfer [10], where the nucleon is transferred from the projectile to a bound state of the target or vice versa, and $(p, 2p)$ reactions [7, 11], although the amount of this quenching varies depending on the reaction and the nucleus studied.

Given the rather naïf picture of the IPM, these discrepancies with experiments should come as no surprise and are a clear indication of beyond-mean-field effects in nuclei. From these effects, those behind the depletion of the spectroscopic factors are believed to be mostly related to nucleon-nucleon correlations, appearing through the interaction between a pair of

nucleons. Nucleon-nucleon correlations are usually separated in short-range correlations (SRC) and long-range correlations (LRC). These correlations couple different single-particle levels, reducing the occupancy of the levels below the Fermi energy (the energy of the least-bound nucleon in the nucleus), which is transferred to energies over the Fermi energy. This effect is illustrated in Fig. 1.6 for nuclear matter and for ^{208}Pb. It must be noted that in this figure are presented both level occupancy and the related quasi-hole strength, which is better related to nucleon removal reactions in systems with correlations. Further information can be found in [12].

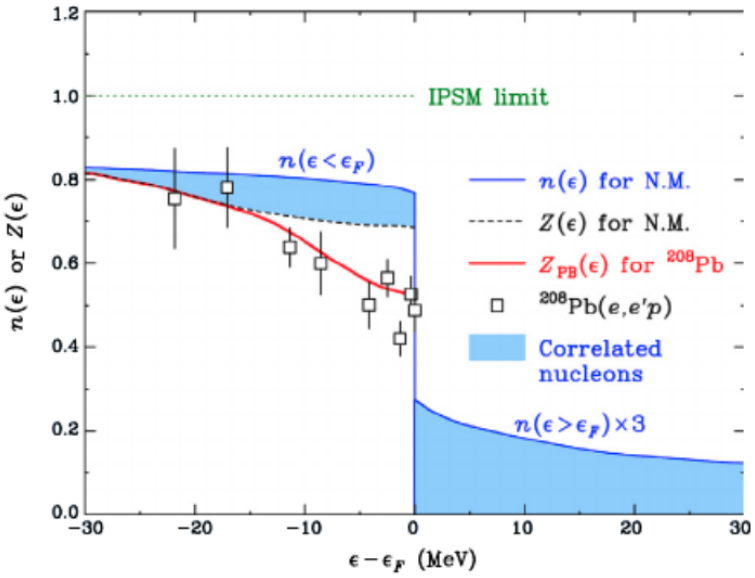

Figure 1.6: Occupation probability ($n(\epsilon)$) and quasi-hole strength ($Z(\epsilon)$) for nuclear matter and ^{208}Pb. The transfer of quasi-hole strength from levels below the Fermi energy ϵ_F to levels above it due to nucleon-nucleon correlations is apparent. Figure taken from [13].

SRC are believed to originate in the strong tensor term and repulsive core of the nucleon-nucleon interaction, coupling states with low energy to states with high energy, and are believed to account for ∼15% of the "quenching' of the spectroscopic factors. LRC couple single-particle motion to low-lying states of the nucleus, which appear due to collective motion of the nucleons in the nucleus resulting in effects such as nuclear deformation or superfluidity, and are assumed to provide another ∼20% reduction in the single-particle spectroscopic factors, resulting in a total reduction of ∼35%, as found in

$(e, e'p)$ experiments [9].

Nuclear structure models including at least some of these effects have been developed to better describe the properties of nuclei. A list of various nuclear structure models, which is not meant to be exhaustive nor comprehensive, is presented in the following:

- **Interacting Shell Model (ISM)**: An extension of the IPM, keeping the shell model scheme, is the inclusion of a residual interaction which couples different IPM levels, resulting in a Hamiltonian whose diagonalization gives the energy of the ground and excited states, whose associated eigenvectors are a combination of different single-particle states, such that the coefficient of the single-particle state can be related to its spectroscopic factor. The diagonalization of the Hamiltonian is usually performed in a truncated basis space (the valence space) from which the nucleons from deep shells are excluded, forming an inert core. The empty levels with energies far above the Fermi energy are also excluded, assuming that they couple weakly to occupied levels. As such, the valence space usually only involves occupied and empty levels around the Fermi energy (ϵ_F). This truncation of the space requires the use of an effective nucleon-nucleon interaction to take into account the effect of the excluded channels, which is adjusted to reproduce the properties of nuclei in the region of interest. Due to the exclusion of the high-energy levels, this prescription is expected to treat worse SRC (which can couple these excluded states) than LRC. Many effective interactions have been generated to produce predictions for energy levels and spectroscopic factors for a wide variety of nuclei [14–16]. This model has become the standard tool for calculating spectroscopic factors, thanks to its early development [17] and the accesibility of computer codes which implement it, such as OXBASH [18] or ANTOINE [19], so much that it is now usually referred to simply as shell model (SM).

- **Ab initio No-Core Shell Model (NCSM)**: The use of a truncated valence space in SM introduces a rather strong approximation in the description of nuclei and leads to serious problems when states outside the valence space interfere strongly with those included in the calculation. As such, an improvement on SM which has been made

available thanks to the increased computing capabilities of modern computers is the inclusion of all nucleons in the valence space, as well as extending the valence space in energy to include the relevant high-energy states, in the No-Core Shell Model (NCSM). This model is based on realistic nucleon-nucleon which reproduce two-nucleon phase-shifts up to an energy of ∼350 MeV. These interactions usually present strong repulsive cores, so they have to be renormalized so that the phase space does not become too large [20, 21]. Three-body forces are also included in the calculation. The Hamiltonian generated by the two- and three-body forces among the A nucleons in the system is diagonalized in a harmonic oscillator basis, to preserve translational invariance, though this basis yields incorrect behaviour in the tails of the wavefunction. This method is able to produce nuclear properties from nucleon-nucleon interactions without introducing extra approximations. However it is extremely computationally intensive, so results can only be produced for nuclei with $A \lesssim 16$, without introducing some approximation, such as an inert core [22].

- **Self-Consistent Green Function (SCGF)**: In the Self-Consistent Green Function method (SCGF), one aims to obtain the single-particle propagator $g_{\alpha\beta}(\omega)$, from which the occupancy of a certain level can be obtained:

$$n_\alpha = \int_{-\infty}^{E_0^A - E_0^{A-1}} \mathrm{d}\omega \frac{1}{\pi} \mathrm{Im}(g_{\alpha\alpha}). \tag{1.2}$$

The propagator can be obtained from an equation such as

$$g_{\alpha\beta}(\omega) = g^{(0)}_{\alpha\beta}(\omega) + \sum_{\gamma\delta} g^{(0)}_{\alpha\gamma}(\omega)\Sigma^*_{\gamma\delta}(\omega)g_{\delta\beta}(\omega), \tag{1.3}$$

where $g^{(0)}_{\alpha\beta}(\omega)$ is obtained from a Hartree-Fock IPM calculation and $\Sigma^*_{\gamma\delta}(\omega)$, usually called the self-energy, is produced from $g^{(0)}_{\alpha\beta}(\omega)$ and includes coupling between single-particle states and high-energy states through SRC and between single-particle states and low-lying collective states through LRC. An iterative procedure can be employed where the resulting $g_{\alpha\beta}(\omega)$ is taken as an input to produce $\Sigma^*_{\gamma\delta}(\omega)$ and solve Eq. 1.3 until convergence. The results can be proven to be independent from the starting propagator $g^{(0)}_{\alpha\beta}(\omega)$. Calculations have been produced

to describe $(e, e'p)$ experiments [9] and to produce spectroscopic factors for various oxygen isotopes [23].

- **Gamow Shell Model**: For nuclei near the evaporation lines, the effect of the continuum on nuclear structure becomes increasingly important. However, the harmonic oscillator basis commonly used in shell model calculations is not able to describe the continuum properly. For these cases, a better description can be obtained by working with Berggren states, which include bound states and resonances as well as the non-resonant continuum, discretized along a contour surrounding the resonant states in the complex energy plane. As in the Interacting Shell Model case, in the Gamow Shell Model, a valence space must be defined and an effective nucleon-nucleon interaction used through which to generate the matrix elements which will couple different Berggren states. Gamow Shell Model has been used to compute the structure of nuclei with different levels of exoticity, such as ^{18}O or ^{6}He [24].

- **Nilsson model**: The description of collective effects by the shell model, whose main degrees of freedom are single-particle, requires a large number of states, which is computationally heavy and sometimes infeasible. However, the collective effect of nuclear deformation (nuclei presenting non-spherical shapes) is commonplace in medium-heavy nuclei and found even for some lighter nuclei such as ^{10}Be. For these nuclei, the spherical harmonic oscillator basis is not the best one to describe the nucleus. Instead, the eigenstates of a Hamiltonian such as

$$H = T + \frac{1}{2}\left(\omega_{\parallel}^2 z^2 + \omega_{\perp}^2(x^2+y^2) + v_{s.o.}\hbar\omega_0(\mathbf{l}\cdot\mathbf{s}) + v_{ll}(\mathbf{l}^2 - \frac{1}{2}N(N+3))\right) \tag{1.4}$$

are more suitable for such a description. For these states the relevant quantum numbers are $[N, n_{\parallel}, \Lambda, \Omega]$, with N the principal quantum number, as in the harmonic oscillator, $n_{\parallel}$ the number of quanta corresponding to the parallel direction z and Λ and Ω the projection of the orbital and total angular momenta along z. These states separate from the spherical values with an increasing deformation length δ:

$$\delta = 3\frac{\omega_{\perp} - \omega_{\parallel}}{2\omega_{\perp} + \omega_{\parallel}}, \tag{1.5}$$

as can be seen in Fig. 1.7. We note that these states are not rotationally invariant. The restoration of this symmetry results in the different states developing a rotational band. The Nilsson model has shown remarkable success in reproducing the spectra of medium-heavy deformed nuclei, and it has been applied to more exotic nuclei, such as halo nuclei with a deformed core, like ^{11}Be [25] or in the so-called island of inversion [26].

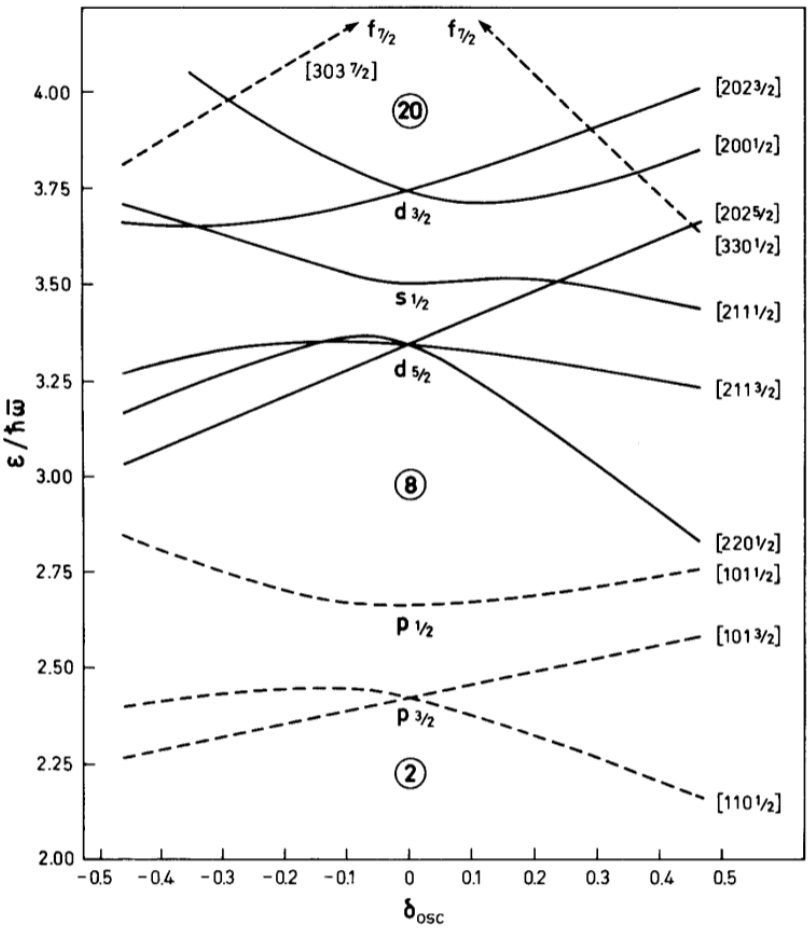

Figure 1.7: Spectrum of single-particle levels as a function of the deformation length δ. Levels are labelled as $[N, n_{\|}, \Lambda, \Omega]$. Figure taken from [27].

These structure models have been used extensively to compare to experimental data, in particular the phenomenological shell model, due to being developed earlier as well as being computationally less demanding, and in general it was found that, although SM produced spectroscopic factors

which were smaller than those from IPM, some additional quenching was still required to reproduce experimental findings, which has been understood as the effect of the correlations that are not included in SM, in particular SRC.

1.1.3 Experiments on exotic beams: Nucleon knockout with heavy targets

With the advent of radioactive beam facilities, more exotic nuclei became accessible to experiment. However, reactions such as $(e, e'p)$ are no longer available with exotic unstable nuclei, for two reasons: first, exotic nuclei are produced as part of a secondary beam after the collision of a primary stable beam with some target. As such, the luminosity for these exotic beams is rather small. This small luminosity, coupled to the rather small $(e, e'p)$ cross sections, makes the statistics for these reactions on exotic beams too small for reliable information to be extracted from them. Secondly, due to the short lifetimes, exotic nuclei cannot be used as targets since they would decay during the preparation of the target. Instead they must be used as beams, making difficult the use of electrons as probes, since this would require the collision of the beam of exotic nuclei and a beam of electrons.

Transfer reactions are also difficult to study systematically, since they depend on stringent matching conditions of energy and angular momentum, which are best fulfilled at energies of tens of MeV. The exotic beams are produced from primary beams at energies of hundreds of MeV, so to reduce their energy to the range where transfer reactions have significant cross sections requires a significant moderation of the beam which reduces significantly the luminosity of the beam. As such, transfer experiments on exotic beams are difficult, although some experiments have been performed [28].

Since the 1990s, one of the most successful probes for the study of exotic beams has been nucleon knockout with composite targets (heavier than p), such as ^{12}C and ^{9}Be. In these reactions, as with $(e, e'p)$ and $(p, 2p)$ reactions, the projectile nucleus A collides with the target so that one of its nucleons is removed, and only a residual core with $A - 1$ nucleons remains. These experiments are inclusive in nature, so that only the residual core is measured, its momentum distribution being the main observable of interest, since, as mentioned in Sec. 1.1.1 it can be used to infer relevant information of the removed nucleon. These reactions present high cross section and are

highly peripheral, due to the highly absorptive nature of the targets at the relevant energies ($\sim$ 100 MeV). This peripherality allows for the use of some assumptions to simplify the description of the reaction mechanism. The most extended formalism to describe knockout reactions [29, 30] relies on two such assumptions: the sudden approximation and the eikonal approximation. Assuming that the projectile nucleus is composed of two distinct subsystems, the removed nucleon N and the residual core C, the sudden approximation assumes that the knockout reaction takes place by a collision between the nucleon N and the target in such a short time that the state of core C is not modified by the reaction. This approximation is not unlike the description of $(e, e'p)$ and $(p, 2p)$ reactions in Sec. 1.1.1. The eikonal approximation is a high-energy approximation that assumes that the projectile, and its constituents N and C follow straight-line trajectories during the reaction. Such an approximation is valid for high energies and light targets, since Coulomb repulsion may alter the trajectory of the projectile, and assumes a small distortive effect due to the projectile-target interaction, or, at least, that a strong interaction between projectile and target leads to absorption so that processes with strong projectile-target interaction do not contribute to the cross section.

With these approximations, the cross section leading to the emission of core C can be expressed as the sum of two incoherent contributions, the stripping contribution and the diffractive contribution. The stripping contribution corresponds to processes in which the nucleon N interacts non-elastically with the target while the core C "survives" and is detected. For a projectile A with spin I, it can be expressed as:

$$\sigma_{str} = \frac{1}{2I+1} \sum_{M} \int \mathrm{d}\mathbf{b} \left\langle \phi^c_{IM} | (1 - |\mathcal{S}_n|^2) | \mathcal{S}_c |^2 | \phi^c_{IM} \right\rangle , \tag{1.6}$$

where $\mathbf{b}$ is the impact parameter, ϕ^c_{IM} is the wave function of the knocked out nucleon leaving the core in a certain state normalized to 1 (A more accurate description of this function will be presented in Chapter 2) and $\mathcal{S}_n, \mathcal{S}_c$ are the S-matrices of the nucleon-target and core-target systems, computed for each impact parameter and assuming eikonal trajectories for both. In a hand-wavy description, $\mathcal{S}_n, \mathcal{S}_c$ relate to the probability of survival of nucleon and core, while the integral over ϕ^c_{IM} gives the probability of finding the nucleon at a certain impact parameter to be knocked out.

The diffractive contribution is related to the elastic breakup of the projectile, corresponding to processes where both nucleon and core "survive" and leave the target in its ground state. It can also be computed with the same ingredients as the stripping contribution:

$$\sigma_{diff} = \frac{1}{2I+1}\int \mathrm{d}\mathbf{b}\left[\sum_{M}\langle\phi^{c}_{IM}||\mathcal{S}_n\mathcal{S}_c|^2|\phi^{c}_{IM}\rangle - \sum_{M,M',i'}|\langle\phi^{c}_{I'M'}(i)|\mathcal{S}_n\mathcal{S}_c|\phi^{c}_{IM}\rangle|^2\right], \tag{1.7}$$

which can be understood as the probability of both core and nucleon surviving (first term) subtracting the probability of them leaving in any of the bound states i of the projectile, since that would not result in the detection of the core. Both contribution are summed incoherently, leading to the single-particle cross section.

Systematic studies of nucleon knockout reactions on stable and exotic nuclei during the 90s and 2000s showed a remarkable tendency for the "quenching" of the spectroscopic factors, which were found to be markedly dependent on the asymmetry of the studied nucleus [31, 32], as is shown in Fig. 1.8. In it the x-axis corresponds to ΔS, the difference between the separation energy of the species that was removed $S_{p(n)}$ and the separation energy of the other nuclear species $S_{n(p)}$. Therefore, for proton knockout $\Delta S = S_p - S_n$ while for neutron knockout $\Delta S = S_n - S_p$. Since the separation energy of neutrons or protons is related to their relative abundance in the nucleus (excess neutrons or protons are less bound), more symmetric nuclei are situated near $\Delta S = 0$, while more asymmetric nuclei move to large $|\Delta S|$, going to negative values when the less bound species is removed and to positive values when the more bound species is.

As can be seen in the figure, despite a sizeable dispersion in the values of the "quenching factors" R_s, a clear linear dependence is found between them and ΔS, with the least bound nuclei in asymmetric species showing R_s close to 1 while the most bound ones show R_s close to 0.2, showing a loss of single-particle strength of 70-80%. We note that one must refrain from comparing this figure to Fig. 1.5 due to the x-axis representing a different value, in Fig. 1.5 being the nuclear mass and in Fig. 1.8 being the separation energy asymmetry ΔS. In fact, all results from Fig. 1.5 would be concentrated near 0, since they are all referring to stable, fairly symmetric nuclei. Another point of difference is the definition of R_s. In Fig. 1.5, the calculations were

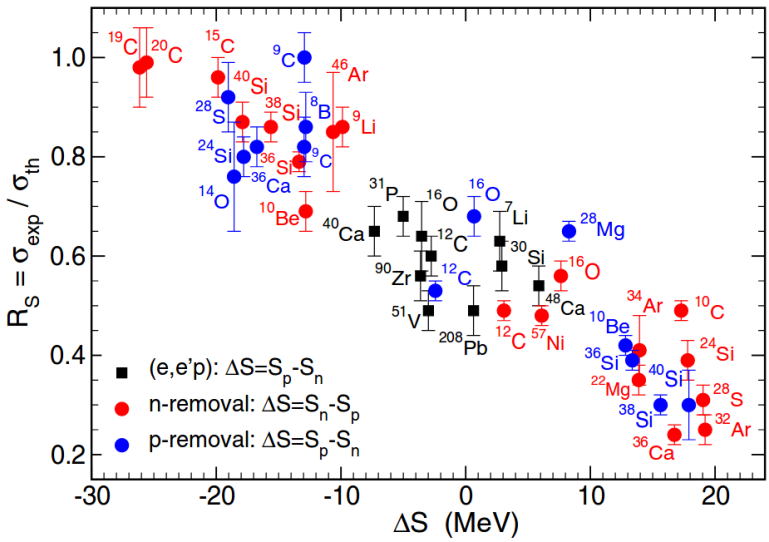

Figure 1.8: "Quenching factors" as a function of the difference in separation energies $\Delta S = S_{p(n)} - S_{n(p)}$ for nucleon knockout reactions with heavy targets at intermediate energies. Figure taken from [32].

referred to IPM spectroscopic factors, while in [32], the spectroscopic factors were computed using the Shell Model, which can be rather different from those of the IPM.

The reason for this asymmetry dependence is not clear. It suggests a stronger effect of nucleon-nucleon correlations for the deficient species in a nucleus, which may stem from it having a higher binding energy and thus being confined to smaller radii, where the density of the nucleus is larger and the interaction between nucleons may result stronger. Standard shell model calculations would not be able to describe these correlations properly since most of the observables they have been adjusted to reproduce relate to nucleons in the valence orbits and not those in deeper levels. On the other hand, nucleons in excess exhibit low binding energies and spatially extended wavefunctions, so their wavefunctions explore regions with a reduced nuclear density where the effect of short-range correlations would be smaller and better described by the SM.

1.1.4 Recent transfer experiments on exotic beams

Despite the difficulties of carrying out transfer experiments on exotic nuclei, some systematic experiments have been published covering transfer from stable as well as unstable nuclei. Here we note two recent publications:

- In [33], a (p, d) transfer reaction was reported at 33 MeV/A on different argon isotopes: ^{34}Ar, ^{36}Ar, ^{46}Ar. The reaction was analyzed using the Adiabatic Distorted Wave Approximation (ADWA) [34, 35]. It was found that although the values of the "quenching factors" R_s were heavily dependent on the optical potentials used for the analysis of the reaction, no clear dependence on ΔS (which spanned from -10 to 15 MeV) was found, and certainly not of the magnitude presented in nucleon knockout experiments. This reduced dependence on the asymmetry agrees with previous results of the same authors [36], although in these results, the large dispersion of the R_s impeded solid conclusions.

- In [37], $(d,^3\mathrm{H})$ and $(d,^3\mathrm{He})$ transfer reactions were reported at an energy of ∼18 MeV/A on different oxygen isotopes: ^{14}O, ^{16}O and ^{18}O. The experimental data were analized using the Coupled Reaction Channels (CRC) formalism [38, 39]. The wave function for the transferred nucleon has been computed through two methods: generating the radial wavefunction from a Woods-Saxon potential normalizing it with the spectroscopic factor obtained from a shell model calculation, and from SCGF calculations. The resulting R_s of both analysis are presented in Fig. 1.9. As can be seen the quantitative values of the R_s are similar for ^{16}O although somewhat different for ^{14}O (no ^{18}O SCGF calculation is presented). Even so, the overall tendency, showing no dependence on ΔS is observed in both analysis, despite a rather large range for ΔS: -20 to 20 MeV. Further analyses of the sensitivity of the R_s on the inputs of the calculations show relatively large variations of the values of R_s although the small dependence on ΔS is found to resist the variations in inputs [40].

The results of these transfer experiments as well as some other systematic studies on more stable species [10] point to the R_s as being independent on the neutron-proton asymmetry ΔS. This result is in conflict with that presented earlier for knockout reactions and raises questions on the origin of

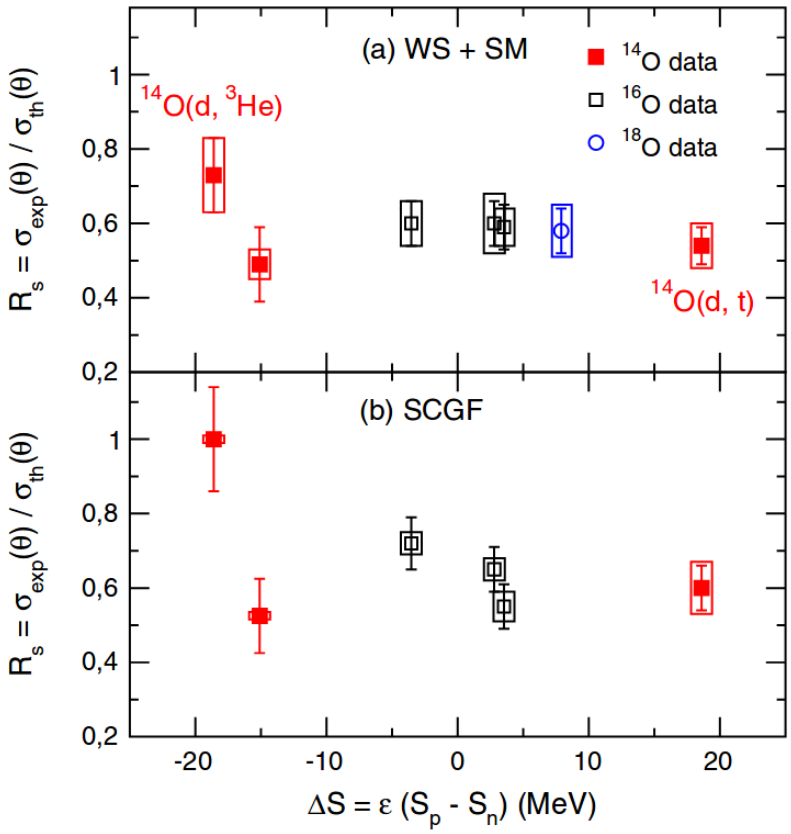

Figure 1.9: "Quenching factors" as a function of the difference in separation energies $\Delta S = S_{p(n)} - S_{n(p)}$ for $(d,^3\mathrm{H})$ and $(d,^3\mathrm{He})$ reactions. Figure taken from [37]. The top panel corresponds to calculations where the transferred nucleon wavefunction has been computed from a Woods-Saxon potential and normalized to the spectroscopic factor from SM. The bottom panel corresponds to nucleon wavefunctions from SCGF.

the observed "quenching": If the "quenching" originated in nucleon-nucleon correlations as has been assumed, it should depend on the characteristics of the explored nucleus and not on the probe used to study it. Even if some disagreement is expected between analyses due to theoretical uncertainties, such a discrepancy in the behaviour of the R_s is difficult to explain from nuclear structure arguments.

Therefore, it has been considered whether the reaction formalisms used to study these reactions are properly justified. For the analysis of mid-energy nucleon knockout reactions, the sudden approximation (which assumes the state of the core not to be modified during the reaction) has been put into

question for the knockout of deeply-bound nucleons. These nucleons have to be extracted from deeper regions inside the nucleus, so it is difficult for the target to interact with these nucleons without altering the rest of the projectile (the core) [23, 37].

As for transfer reactions, the marked dependence of the results on the ingredients of the calculation, in particular in the rather involved CRC formalism, may introduce large uncertainties in the final R_s which may cloud the extraction of overall tendencies [41].

1.1.5 (p, pn) and $(p, 2p)$ reactions on exotic nuclei

The asymmetry dependence of the "quenching factors" R_s remains an open problem in the nuclear physics community up to date. Further experimental data studying nuclei with varying values for ΔS are desirable in order to build a reliable systematics. The experiment should also involve a reaction mechanism that is well understood in order to minimize the uncertainties of the reaction calculation, so that the asymmetry dependence can be solidly related to the properties of the studied nuclei.

In order to clarify the situation, very recently experimental campaigns on $(p, 2p)$ and (p, pn) reactions have been performed both by the R^3B collaboration in the GSI facility in Germany as well as by the group at RIBF/RIKEN in Japan. (p, pN) reactions are particularly attractive because the nucleon-nucleon interaction is well-known, so it is expected that a better description of the reaction mechanism can be obtained than for knockout with heavier targets. The QFS condition described in Sec. 1.1.1 is also pursued in order to have a "cleaner" reaction. For this reason, reactions have been performed at beam energies of 200-450 MeV/A, for which the nucleon mean free path is maximal.

Experimental analyses of these reactions must deal with the problem of low luminosity inherent to the use of exotic beams. In order to increase statistics, the R^3B collaboration has focused on inclusive observables, in particular inclusive momentum distributions of the emitted core, in which the angle and energy of the outgoing nucleons is not restricted. The two outgoing nucleons are detected in order to ensure that the residual core is in fact the product of a (p, pN) reaction, but are only taken as "gating" of the relevant events. Results from this experimental campaign have very

recently been published [23, 42, 43], and are subject of analysis in Sec. 4.2 so a comment on them is left for the corresponding section.

The measurements at RIBF have instead produced exclusive cross sections, where the quantities of interest were the energy and angle distributions of the emitted nucleons, using the detection of a proper residual core as "gating" for the events of interest. Results for different isotopes of oxygen (^{14}O, ^{16}O, ^{18}O, ^{22}O, ^{24}O) have been recently presented [44]. The obtained R_s as a function of ΔS are presented in Fig. 1.10. Two results employing different optical potential parametrizations in the theoretical analysis are presented: The red triangles correspond to potentials from the phenomenological Dirac parametrization [45, 46] while the blue ones use potentials obtained from the folding of the nuclear densities with the Melbourne g-matrix effective interaction [47]. As can be seen in Fig. 1.10, both results agree rather reasonably between themselves and with the results from $(e, e'p)$ and heavy-ion knockout reactions presented in the figure. Despite a somewhat large dispersion of the R_s, no clear R_s asymmetry dependence can be appreciated, so these results seem to favour those from transfer as opposed to those from heavy-ion knockout.

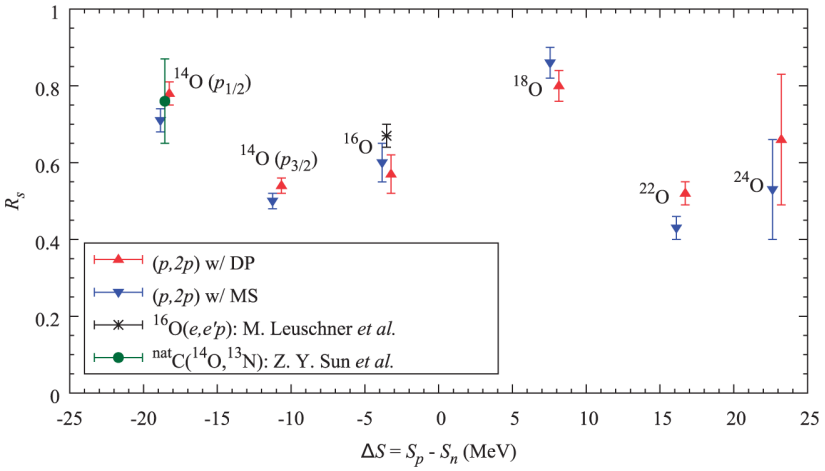

Figure 1.10: "Quenching factors" as a function of the difference in separation energies $\Delta S = S_{p(n)} - S_{n(p)}$ for exclusive $(p, 2p)$ reactions. Red and blue triangles denote calculations with different optical potentials, while the green circle and black asterisk are results from heavy-ion knockout and $(e, e'p)$ shown for comparison. Figure taken from [44].

The extraction of the R_s relies heavily on the reaction formalism used

to describe the reaction from which spectroscopic information is extracted, since the distortion and absorption effects taking place during the reaction influence heavily the experimental observables. As such, a proper description of these effects is paramount to obtain a good description of the reaction and in particular, of the magnitude of the cross section, which is essential for the evaluation of "quenching". In the following section, different formalisms used to analyze (p, pn) and $(p, 2p)$ reactions in recent works are presented.

1.2 Reaction formalisms for (p, pn) and $(p, 2p)$ reactions

In this section some reaction formalisms used in the literature for the analysis of (p, pn) and $(p, 2p)$ reactions are briefly described:

1.2.1 Plane-Wave Impulse Approximation (PWIA)

Although it is a rather unrealistic approximation, the plane-wave impulse approximation is a useful model to shed some light on the dynamics of the (p, pN) process. It assumes a similar portrayal of the reaction as that taken in the QFS model from Sec. 1.1.1, in which both the incoming proton and the outgoing proton, nucleon and core can be described by plane waves, thus ignoring the interactions among them.

In this approximation, and assuming an infinitely massive core, whose internal degrees of freedom are not altered by the reaction, the matrix element for the reaction can be expressed as:

$$\mathcal{T}_{if} = \left\langle e^{-i\mathbf{k}_p\cdot\mathbf{r}_p} e^{-i\mathbf{k}_N\cdot\mathbf{r}_N} |T_{pN}| e^{i\mathbf{k}_0\cdot\mathbf{r}_p} \varphi_{nljm}(\mathbf{r}_N) \right\rangle , \tag{1.8}$$

where we ignore the spins of the nucleons for simplicity and where the p, N and 0 subscripts correspond to the outgoing proton and nucleon and the incoming proton respectively and φ_{nljm} denotes the wave function of the bound nucleon. T_{pN} is the transition matrix between the initial and final states corresponding only to the V_{pN} interaction.

Next, the Impulse Approximation approximates T_{pN} by the free nucleon-nucleon t-matrix between proton and nucleon. This neglects the interaction of the proton with the rest of the target nucleus, as well as ignoring the effect

of the binding energy during the collision:

$$T_{pN} = \left\langle \kappa'_{pN} | t_{pN} | \kappa_{pN} \right\rangle , \tag{1.9}$$

with κ_{pN} the relative momentum between proton and neutron. Assuming a slow variation of t_{pN} with κ_{pN}, it is possible to perform a factorization of T_{pN} which results in a zero-range approximation:

$$\mathcal{T}_{if} = \left\langle e^{-i\mathbf{k}_p \cdot \mathbf{r}_p} e^{-i\mathbf{k}_N \cdot \mathbf{r}_N} | \delta(\mathbf{r}_p - \mathbf{r}_N) | e^{i\mathbf{k}_0 \cdot \mathbf{r}_p} \varphi_{nljm}(\mathbf{r}_N) \right\rangle \left\langle \kappa'_{pN} | t_{pN} | \kappa_{pN} \right\rangle , \tag{1.10}$$

which can be related to the Fourier transform of φ_{nljm}:

$$\mathcal{T}_{if} = \int \mathrm{d}\mathbf{r}_N e^{-i\mathbf{Q} \cdot \mathbf{r}_N} \varphi_{nljm}(\mathbf{r}_N) \left\langle \kappa'_{pN} | t_{pN} | \kappa_{pN} \right\rangle , \tag{1.11}$$

with $\mathbf{Q} = \mathbf{k}_p + \mathbf{k}_N - \mathbf{k}_0$. Since we have neglected the effect of binding energy and distorting potentials, the elements $\left\langle \kappa'_{pN} | t_{pN} | \kappa_{pN} \right\rangle$ must be on-shell due to conservation of energy. This allows to relate them to the free nucleon-nucleon cross section.

$$| \left\langle \kappa'_{pN} | t_{pN} | \kappa_{pN} \right\rangle |^2 = \frac{(2\pi\hbar^2)^2}{\mu_{pN}^2} \frac{\mathrm{d}\sigma_{pN}}{\mathrm{d}\Omega_{pN}}(E_{pN}, \theta_{pN}), \tag{1.12}$$

where E_{pN} and Ω_{pN} are the proton-nucleon relative energy and scattering angle and are computed from κ_{pN} and κ'_{pN}. From here the cross section for the (p, pN) is found to be proportional to the product of the free nucleon-nucleon cross section and the square of the Fourier transform of $\varphi_{nljm}(\mathbf{r}_N)$:

$$\frac{\mathrm{d}\sigma}{\mathrm{d}\mathbf{k_p}\mathrm{d}\mathbf{k_N}} \propto \frac{\mathrm{d}\sigma_{pN}}{\mathrm{d}\Omega_{pN}}(E_{pN}, \theta_{pN}) \frac{1}{2j+1} \sum_m \left| \int \mathrm{d}\mathbf{r}_N e^{-i\mathbf{Q} \cdot \mathbf{r}_N} \varphi_{nljm}(\mathbf{r}_N) \right|^2 . \tag{1.13}$$

If, as usual, we normalize $\varphi_{nljm}(\mathbf{r}_N)$ to 1, and extract its norm as a spectroscopic factor, we find:

$$\frac{\mathrm{d}\sigma}{\mathrm{d}\mathbf{k_p}\mathrm{d}\mathbf{k_N}} \propto SF_{nlj} \frac{\mathrm{d}\sigma_{pN}}{\mathrm{d}\Omega_{pN}}(E_{pN}, \theta_{pN}) \frac{1}{2j+1} \sum_m \left| \int \mathrm{d}\mathbf{r}_N e^{-i\mathbf{Q} \cdot \mathbf{r}_N} \varphi_{nljm}(\mathbf{r}_N) \right|^2 , \tag{1.14}$$

which shows that, in the PWIA limit, the cross section is sensitive in its magnitude to the spectroscopic factor of the level from which the nucleon

is removed, and in its shape, to its Fourier transform, and therefore to its angular momentum. This marks the remarkable spectroscopic power of the reaction. We note that the plane-wave approximation is too extreme to give a good description of the reaction, in particular of the magnitude of the cross section. However, it has seen an extensive use in $(e, e'p)$ reactions [48].

1.2.2 Distorted-Wave Impulse Approximation (DWIA)

The DWIA formalism faces the description of the $A(p, pN)C$ reaction through the so-called Impulse Approximation, as PWIA. It however includes the effects of distortion originating in the interaction between proton and target, proton and core and nucleon and core, which are included in the T matrix by substituting the plane waves by distorted waves:

$$\mathcal{T}_{if} = \left\langle \chi^{(-)}_{p,\mathbf{k}_p} \chi^{(-)}_{N,\mathbf{k}_N} | t_{pN} | \chi^{(+)}_{p,\mathbf{k}_0} \varphi_{nljm} \right\rangle . \tag{1.15}$$

Here $\chi^{(\pm)}$ denote distorted waves corresponding to an incoming proton with momentum $\mathbf{k}_0$, and outgoing proton and nucleon with momenta $\mathbf{k}_1$ and $\mathbf{k}_2$ respectively. In order to present more realistic formulae, in this section the formalism for a core with finite mass is presented. The neglect of off-shell effects is still maintained. We will be following the formulation in [49]. With these approximations, the core momentum distribution in the system where nucleus A is at rest is given by the expression:

$$\begin{aligned} \frac{\mathrm{d}\sigma}{\mathrm{d}\mathbf{p}_C^A} = C_0 S F_{nlj} \int \mathrm{d}\mathbf{p}_1 \mathrm{d}\mathbf{p}_2 \eta^A_{M\phi 1} \delta(E_f^A - E_i^A) \delta(\mathbf{p}_f^A - \mathbf{p}_i^A) \frac{\mathrm{d}\sigma_{pN}}{\mathrm{d}\Omega_{pN}} \\ \times \sum_m (2\pi)^2 \left| \int \mathrm{d}\mathbf{R} \chi^{(-)*}_{p,\mathbf{k}_p} \chi^{(-)*}_{N,\mathbf{k}_N} \chi^{(+)}_{p,\mathbf{k}_0} \varphi_{nljm} e^{-i\mathbf{k}_0 \cdot \mathbf{R}/A} \right|^2 , \end{aligned} \tag{1.16}$$

where the δ impose conservation of energy and momentum, the superscript A denotes that the quantities are computed in the rest frame of A and where

$$C_0 = \frac{E_0^A}{(\hbar c)^2 p_0^A} \frac{1}{2l+1} \frac{\hbar^5}{(2\pi)^3 \mu_{pN}^2} \tag{1.17}$$

and

$$\eta^A_{M\phi 1} = \frac{E_1 E_2 E_B}{E_1^A E_2^A E_B^A}, \tag{1.18}$$

$\eta^A_{M\phi 1}$ being the Möller factor, which stems from the transformation from the $N-N$ frame to the $N-A$ frame. Here the quantities without superscript are computed in the center of mass system. More information can be found in [50]. We note that this expression is similar to the PWIA one,but with a distorted Fourier transform of the nucleon wavefunction.

The DWIA formalism has been used in the analysis of [44].

1.2.2.1 Eikonal DWIA

Due to the large energies involved in the (p, pn) and $(p, 2p)$ reactions measured in GSI and RIBF, it is possible to simplify somewhat the calculations by using the eikonal approximation [51], which assumes the particles involved to describe linear trajectories during the reaction.

Following [52], in the eikonal approximation the distorted waves for the incoming proton and outgoing proton and nucleon can be expressed as plane waves multiplied by "survival amplitudes" $\mathcal{S}_{in(out)}$, which are functions of the impact parameter b:

$$\chi^{in(out)}_{p(N)}(\mathbf{r}) = \mathcal{S}_{in(out)}(b) e^{i\mathbf{k^{in(out)}_{p(N)}}\cdot\mathbf{r}}, \tag{1.19}$$

$$\mathcal{S}_{in(out)}(b) = \exp\left[-\frac{i}{\hbar v}\int_{a_{in(out)}}^{b_{in(out)}} \mathrm{d}z' U^{in(out)}_{p(N)}(\mathbf{r}')\right], \tag{1.20}$$

where, for the incoming proton the integral is performed between the point where it starts to feel the interaction with the nucleus (formally $-\infty$) and the collision point, and for the outgoing proton and nucleon the integral starts at the collision point until they stop feeling the interaction with the core (formally ∞). It must be remarked that the incoming proton and outgoing nucleons describe straight-line trajectories. However, they are not parallel, as in standard eikonal theory, since the collision between two particles of similar mass (the proton and the nucleon) can lead to a strong change in direction. As such z' and b have a different value for each distorted wave.

The cross section as a function of $\mathbf{Q} = \mathbf{k_p} + \mathbf{k_N} - \frac{A-1}{A}\mathbf{k_0}$, the transferred momentum (which corresponds to the definition in Sec. 1.2.1 in the infinite-

mass limit), can be expressed as:

$$\frac{\mathrm{d}\sigma}{\mathrm{d}\mathbf{Q}} = \frac{1}{(2\pi)^2}\frac{SF_{nlj}}{2j+1}\sum_m \left\langle \frac{\mathrm{d}\sigma_{pN}}{\mathrm{d}\Omega_{pN}} \right\rangle_Q \left| \int \mathrm{d}\mathbf{r} e^{-i\mathbf{Q}\cdot\mathbf{r}} \left\langle \mathcal{S}(b) \right\rangle_Q \varphi_{nljm}(\mathbf{r}) \right|^2 . \quad (1.21)$$

In this expression the brakets denote an average over all the configurations that lead to a transferred momentum $\mathbf{Q}$, and $\mathcal{S}(b)$ is the product of the three survival amplitudes corresponding to the incoming proton, the outgoing proton and the outgoing nucleon. Since the transferred momentum can be easily identified with the momentum of the core in the frame of reference where A is at rest, this cross section can be immediately translated the momentum distribution of the core. This formalism has been used in the analysis of [23, 42] and further details can be found in [52].

1.2.3 Faddeev/AGS formalism

The Faddeev/AGS [53, 54] formalism allows to obtain the exact solution of a non-relativistic three-body problem, through the evaluation of the operators $U^{\beta\alpha}$, whose on-shell matrix elements correspond to the transition amplitudes and which are obtained solving the three-body AGS integral equations. As opposed to the previous formalisms, it does not consider any approximation beyond the assumption that the nucleus A can be treated as a two-body system, and thus the $p+A$ reaction can be treated as a three-body problem. The operators $U^{\beta\alpha}$ fulfil:

$$U^{\beta\alpha} = \bar{\delta}_{\beta\alpha} G_0^{-1} + \sum_\gamma \bar{\delta}_{\beta\gamma} t_\gamma G_0 U^{\gamma\alpha}, \quad (1.22)$$

where α, β, γ denote states corresponding to one of the three possible partitions of the problem: $p+(n+C)$, $C+(p+n)$, $n+(p+C)$ or to the breakup state $p+n+C$, $\bar{\delta}_{\beta\alpha} = 1 - \delta_{\beta\alpha}$ and t_γ corresponds to the two-body t-matrix in the 3-body medium:

$$t_\gamma = v_\gamma + v_\gamma G_0 t_\gamma, \quad (1.23)$$

where the odd-one out notation is used so for example, assigning 1 to the $p + (n + C)$ partition $v_1 = V_{pn} + V_{pC}$. Finally G_0 is the free resolvent $G_0 = (E + i\epsilon - H_0)^{-1}$ in the limit $\epsilon \to 0$. Breakup observables are obtained from the on-shell matrix elements of $U^{0\alpha}$: $T^{0\alpha} = \langle \mathbf{qp}|U^{0\alpha}|\psi_\alpha\rangle$, where α corresponds to the initial state: $p+(n+C)$, and $\mathbf{p}, \mathbf{q}$ are chosen as the Jacobi

momenta for the $C + (p + n)$ partition. From here the double differential cross section for the energy and angle of the core can be computed as:

$$\frac{\mathrm{d}\sigma}{\mathrm{d}E_C \mathrm{d}\Omega_C} = (2\pi)^4 \frac{m_n + m_C}{K_{lab}} m_C k_C \frac{m_n m_p}{m_n + m_p} \int \mathrm{d}\hat{p} \mathcal{F} |T^{0\alpha}|^2, \tag{1.24}$$

with k_C the momentum of the core, K_{lab} that of the projectile in the laboratory frame and

$$\mathcal{F} = \sqrt{2\frac{m_n m_p}{m_n + m_p} E - \frac{m_n m_p M}{m_C (m_n + m_p)^2} \left(k_C^2 + \frac{m_C^2}{M^2} K_T - 2\frac{m_C}{M} \mathbf{k}_c \cdot \mathbf{k}_T \right)}, \tag{1.25}$$

where $M = m_p + m_n + m_C$ and K_T is the total momentum, which is 0 in the center of mass frame and K_{lab} in the laboratory frame. More information can be found in [55–57]. The Faddeev/AGS formalism has been used in the analysis of [43].

It is the objective of this work to develop a new reaction formalism able to compute $(p, 2p)$ and (p, pn) reactions at low, intermediate and high energies. For this, it will not be based on the impulse approximation, thus allowing for its use at lower energies than PWIA and DWIA, and it includes relativistic kinematics, which are not present in the Faddeev/AGS formalism presented in the previous section and which are found to introduce important modifications in the cross section at high energies. This formalism is called Transfer to the Continuum and is presented and developed in Chapter 2. Then, in Chapter 3, it is benchmarked to other reaction formalisms, DWIA and Faddeev, in the regions and with the approximations to make the comparison meaningful. In Chapter 4, calculations using this new formalism are compared with experimental data and special interest is devoted to the analysis of the "quenching factors" R_s for the experiments carried out by the R^3B collaboration [23, 42, 43]. In Chapter 5, the formalism is extended to study the energy distributions of the fragments obtained in (p, pn) reactions on Borromean nuclei and results are presented for ^{11}Li. Finally, an overall summary of the results of the present project is presented in Chapter 6, establishing an outlook for future developments.

Chapter 2

Formalism: Transfer to the continuum

Someone told me that each equation I
included in the book would halve the sales

Stephen Hawking

The formalism used throughout this work is referred to as Transfer to the Continuum (TC) and has been used previously to study breakup reactions at low and intermediate energies [58, 59]. In short, it can be described as a CCBA-like (Coupled-Channel Born Calculation) calculation akin to a transfer reaction leading to continuum states of the projectile. In the next section, the formalism is detailed, highlighting the modifications required for its extension to high-energy reactions, where relativistic effects are of importance.

2.1 Coupled equations

A reaction of the type $A(p, pN)C$ can be studied within a three-body model where the relevant bodies are the incoming proton p, the removed nucleon N and the residual nucleus or *core* C. Of these, only the core C may have internal degrees of freedom ξ, which will be assumed to be collective, in nature. The excitation of the nucleons to a Δ resonance requires too much energy to be of relevance in the range of energies considered. As such, the

three-body Hamiltonian is as follows:

$$H_{3b} = T + H_C(\xi) + V_{pN}(r_{pN}) + U_{pC}(\mathbf{r}_{pC}, \xi) + U_{NC}(\mathbf{r}_{NC}, \xi), \tag{2.1}$$

where, as usual, $\mathbf{r}_{ab}$ denotes the relative position between particles a and b. Since the core C is in reality a many-body system composed of $A-1$ nucleon, the interactions U_{pC} and U_{nC} must be taken as effective nucleon-nucleus interactions that model the interaction between the nucleon and the $A-1$ nucleons forming the core C. These effective interactions include an imaginary part that accounts for the loss of flux to reaction channels not included in the formalism.

In Eq. (2.1), T corresponds to the kinetic energy of the three bodies p, N and C. In the center of mass system, it can be expressed as

$$T = -\frac{\hbar^2 \nabla^2_{R^{(i)}}}{2\mu_{ab-c}} - \frac{\hbar^2 \nabla^2_{r^{(i)}}}{2\mu_{ab}} = T_{R^{(i)}} + T_{r^{(i)}}, \tag{2.2}$$

where $r^{(i)}$ is the relative coordinate between the bodies a and b and R^i is the relative coordinate between the center of mass of the $a-b$ system and body c. μ_{ab} and μ_{ab-c} are the reduced masses, defined as follows:

$$\mu_{ab} = \frac{m_a m_b}{m_a + m_b} \qquad\qquad \mu_{ab-c} = \frac{(m_a + m_b) m_c}{m_a + m_b + m_c}. \tag{2.3}$$

These coordinates are proportional to the Jacobi coordinates [60], and as such, the shape of the kinetic energy is the same for whichever bodies are chosen as a, b and c. In the 3-body case, 3 possible sets of Jacobi coordinates are possible, which are illustrated in Fig. 2.1. Of these, set (1) is specially relevant for the (p, pn) reaction because it is the set where the initial state (where nucleon N is bound to the core C forming nucleus A) is most naturally described. In fact, in standard Continuum-Discretized Coupled-Channel (CDCC) calculations it is the only set of coordinates considered [61, 62]. For Transfer to the Continuum calculations, set (2) is also relevant, since it corresponds to the states to which nucleon N is "transferred" to. Set (3) is not taken into account in our reaction formalism although it is considered in formalisms using the Faddeev/AGS equations [53, 54] where all Jacobi sets are treated on an equal footing. In the following we will use the notation shown in Fig. 2.1, that is $\mathbf{R} = \mathbf{R}_{NC-p}$, $\mathbf{r} = \mathbf{r}_{NC}$, $\mathbf{R'} = \mathbf{R}_{pN-C}$ and $\mathbf{r'} = \mathbf{r}_{pN}$.

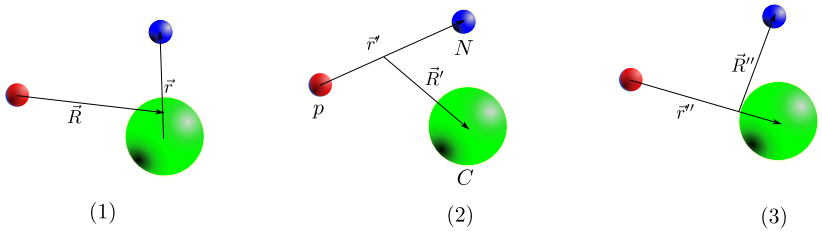

Figure 2.1: Different Jacobi coordinates for a 3-body system.

Let us now express the Hamiltonian using Jacobi set (1) of Fig. 2.1:

$$H_{3b} = T_R + T_r + H_C(\xi) + V_{pN}(r_{pN}) + U_{pC}(\mathbf{r}_{pC}, \xi) + U_{NC}(\mathbf{r}, \xi). \tag{2.4}$$

The full 3-body wave-function for a certain center of mass energy E fulfills the following Schrödinger equation:

$$\begin{aligned}(T_R + T_r + H_C(\xi) + V_{pN}(r_{pN}) + U_{pC}(\mathbf{r}_{pC}, \xi) \\ +U_{NC}(\mathbf{r}, \xi) - E_+)\, \Psi^{3b(+)}(\mathbf{R}, \mathbf{r}, \xi) = 0,\end{aligned} \tag{2.5}$$

where as usual $E_+ = E + i\epsilon$ and the superscript $^{(+)}$ denotes outgoing boundary conditions. For the (p, pN) reaction, we are interested on the transition matrix for an incoming wave of the type $e^{i\mathbf{K}_{\mathrm{pA}}\mathbf{R}}\phi_A(\mathbf{r}, \xi)$, where $\phi_A(\mathbf{r}, \xi)$ is the wavefunction of the ground state of nucleus A and $\mathbf{K}_{pA}$ is the relative wave number between the proton and nucleus A in the incoming channel. As such for very long distances the three-body wavefunction must behave as:

$$\Psi^{3\mathrm{b}(+)}(\mathbf{R}, \mathbf{r}, \xi) \underset{R\gg}{\longrightarrow} \phi_A(\mathbf{r}, \xi) e^{i\mathbf{K}_{\mathrm{pA}}\mathbf{R}} \; + \; \text{outgoing waves.} \tag{2.6}$$

We will now approximate $\Psi^{3\mathrm{b}(+)}(\mathbf{R}, \mathbf{r}, \xi)$ by a model wavefunction:

$$\Psi^{3\mathrm{b}(+)}(\mathbf{R}, \mathbf{r}, \xi) \simeq \Psi_{\mathrm{model}} = X_A(\mathbf{R})\phi_A(\mathbf{r}, \xi) + \Psi_b, \tag{2.7}$$

with X_A having the asymptotic behaviour

$$X_A(\mathbf{R}) \underset{R\gg}{\longrightarrow} e^{i\mathbf{K}_{\mathbf{pA}}\mathbf{R}} + f_{A,A}(\theta)\frac{e^{iK_{pA}R}}{R}, \tag{2.8}$$

where we can recognise the second term as outgoing waves in the elastic channel, leaving nucleus A in its ground state.

On the other hand, Ψ_b contains outgoing waves associated with the bound

states of system pN (that is, the deuteron when N is a neutron) and in the breakup states only. We note that by using this model wavefunction we are excluding from our model space many reaction channels such as possible excitations of A or multinucleon transfer. However, these channels will only contribute to the (p, pn) cross section through coupling to the breakup channels, which we expect to be small, due to the suddenness of the reaction, which results from the high energy of the projectile.

By projecting Eq. (2.5) over $\langle\phi_A|$ (where, as per usual, the *braket* denotes integration over internal variables only) we obtain the following equation:

$$\langle\phi_A|H - E|\Psi_b\rangle + \langle\phi_A|H - E|X_A\phi_A\rangle = 0 \tag{2.9}$$

Now we will introduce the approximation that $\langle\phi_A|H - E|\Psi_b\rangle$ can be neglected in Eq. (2.9). This is a sort of Born approximation, in which we will assume that the coupling potential between $X_A\phi_A$ (the incoming channel) and Ψ_b (the outgoing channels) is small, so the elastic channel will not be modified by the outgoing channels. As such, Eq. (2.9) is reduced to:

$$\begin{aligned}\langle\phi_A(\mathbf{r},\xi)\,|T_R + T_r + H_C + V_{pN}(r_{pN}) + U_{pC}(\mathbf{r_{pC}},\xi) + U_{NC}(\mathbf{r},\xi)\\ -E|\ X_A(\mathbf{R})\phi_A(\mathbf{r},\xi)\rangle = 0,\end{aligned} \tag{2.10}$$

Now, from the assumption that A is composed of the core C and nucleon N with U_{NC} binding N and C forming the ground state of A, we recognize $H_A = T_r + H_C + U_{NC}$, so

$$\langle\phi_A(\mathbf{r},\xi)|T_r + H_C + U_{NC}(\mathbf{r},\xi)|\phi_A(\mathbf{r},\xi)\rangle = E^A, \tag{2.11}$$

where E_A can be taken as the binding energy of nucleus A, although as for now the exact value of this energy is not important. This leaves Eq. (2.10) as

$$\langle\phi_A(\mathbf{r},\xi)|T_R + V_{pN}(r_{pN}) + U_{pC}(\mathbf{r_{pC}},\xi) - E_{cm,i}|X_A(\mathbf{R})\phi_A(\mathbf{r},\xi)\rangle = 0, \tag{2.12}$$

with $E_{cm,i} = E - E^A$. We will now express the integral of $U_{pC} + V_{pN}$ over $\mathbf{r}$ and ξ as:

$$U_{pA}(\mathbf{R}) = \langle\phi_A(\mathbf{r},\xi)|V_{pN}(r_{pN}) + U_{pC}(\mathbf{r_{pC}},\xi)|\phi_A(\mathbf{r},\xi)\rangle\,, \tag{2.13}$$

so that we are left with an equation for X_A such as

$$(T_R + U_{pA}(\mathbf{R}) - E_{cm,i})\, X_A(\mathbf{R}) = 0. \tag{2.14}$$

Now we must propose an expression for Ψ_b, which leaves it in a form that is more amenable to treatment with standard reaction theory and that also allows us to define clearly the final state we are interested in. First, we note that in the final state for a (p, pN) reaction, core C is detected and can be in any of its possible excited states. As such we can decompose Ψ_b as

$$\Psi_b = \Psi^{3b}_{b,\alpha}(\mathbf{R}', \mathbf{r}')\Phi^C_\alpha(\xi) + \sum_{\alpha' \neq \alpha} \Psi^{3b}_{b,\alpha'}(\mathbf{R}', \mathbf{r}')\Phi^C_{\alpha'}(\xi), \tag{2.15}$$

where Φ^C_α denotes the wavefunction of core C in a state α, and where we have chosen α as the final asymptotic state of C (the state in which it is detected) and α' as all other possibles states for C. In this decomposition $\Psi^{3b}_{b,\alpha}$ is a three-body wavefunction that only depends on the relative coordinates between p, N and C with C in state α. We choose to represent $\Psi^{3b}_{b,\alpha}$ in the set of coordinates corresponding to Jacobi set (2) of Fig. 2.1.

The next step on the derivation is the simplification of $\Psi^{3b}_{b\alpha}$, which, being a complex three-body wavefunction, is not amenable to be solved with standard reaction calculations. We choose to expand $\Psi^{3b}_{b\alpha}$ on eigenstates of V_{pN} with defined angular momentum and parity of the $p - N$ subsystem:

$$\Psi^{3b}_{b\alpha}(\mathbf{R}', \mathbf{r}') \simeq \sum_{j^\pi} \int \mathrm{d}k \phi_{j^\pi}(k, \mathbf{r}') X_{j^\pi \alpha}(\mathbf{K}', \mathbf{R}'), \tag{2.16}$$

where $\mathbf{K}'$ and k are related through conservation of energy:

$$\frac{\hbar^2 K'^2}{2\mu_{pN-C}} + \frac{\hbar^2 k^2}{2\mu_{pN}} = E^n_{cm,f} + e^n_{pN} = E - E^C_\alpha, \tag{2.17}$$

where E^C_α is the binding energy of C in state α, verifying:

$$H_C \Phi^C_\alpha = E^C_\alpha \Phi^C_\alpha. \tag{2.18}$$

It must be noted that the bound states of the $p - N$ system are included in the expansion so in the (p, pn) case the transfer to the deuteron is computed consistently with the (p, pn) breakup.

There is an infinite number of $\phi_{j^\pi}(k, \mathbf{r}')$, and they are all infinitely oscillating. Therefore, in order to obtain an expression which is mathematically tractable, it is necessary to employ a method of continuum discretization, which allows to express the infinite possible final states through a finite number of representative states.

There are two main methods to discretize the continuum that have been used in the literature: the first one is referred to as the pseudostate method [63–66]. In it the Hamiltonian of interest is diagonalized in a basis of functions that form a normalizable basis of $\mathcal{L}^2$, that is, that are orthogonal and of finite norm and which form a complete basis of the space, verifying the closure relation:

$$\sum_n |n\rangle\langle n| = \mathcal{I}. \tag{2.19}$$

This method is specially suitable to describe structures in the continuum such as resonances and has been applied successfully to study breakup at low and intermediate energies [63–66].

The second method is the so-called *binning* procedure, in which the continuum is represented by a set of wave packets, called bins, built through the linear superposition of the eigenstates of the potential for momenta between two limit values k_l and k_h with a certain weight factor.

$$\begin{aligned} \tilde{\phi}_n^{j\pi}(\mathbf{r}') &= \sqrt{\frac{2}{\pi N_n}} \int_{k_l}^{k_h} \mathrm{d}k f_n^{j\pi}(k) \phi_{j^\pi}(k, \mathbf{r}') \\ N_n &= \int_{k_l}^{k_h} \mathrm{d}k \left| f_n^{j\pi}(k) \right|^2 . \end{aligned} \tag{2.20}$$

A nominal momentum is given to the bin, usually the average of its lower and upper limits $k_n = (k_h + k_l)/2$ and it can be shown that, by construction, bins for disjunct intervals $k_l - k_h$ are orthogonal.

Since the $p-N$ continuum in the relevant energies for the studied reaction does not present features that require special treatment, we have opted to use the relatively simpler binning procedure, which is already available in standard reaction codes such as FRESCO [67].

When using the binning procedure, the width of the bins $\Delta k_n = k_h - k_l$ as well as the maximum momentum k_{max} considered must be checked for

convergence. In general the weight function has been considered as

$$f_n^{j^\pi}(k) = e^{-i\delta(k)}, \tag{2.21}$$

where $\delta(k)$ is the $p-N$ phase-shift. This choice of the weight guarantees that the bin wavefunction will be real when the bin has only one channel and close to real in the multichannel case.

Applying the binning procedure to Eq. (2.16) we obtain

$$\Psi_{b\alpha}^{3b} \simeq \Psi_{b\alpha}^{\text{bin}} = \sum_{j^\pi n} \tilde{\phi}_n^{j^\pi}(\mathbf{r}') X_{j^\pi n\alpha}(\mathbf{K}'_{\mathbf{n}}, \mathbf{R}'), \tag{2.22}$$

where $\mathbf{K}'_{\mathbf{n}}$ is obtained from conservation of energy from the nominal momentum of the bin k_n. With this approximation Ψ_b can be approximated as:

$$\begin{aligned}\Psi_b \simeq \tilde{\phi}_n^{j^\pi}(\mathbf{r}') X_{j^\pi n\alpha}(\mathbf{K}'_{\mathbf{n}}, \mathbf{R}')\Phi_\alpha^C(\xi) + \sum_{j'^{\pi'} n' \neq j^\pi n} \tilde{\phi}_{n'}^{j'^{\pi'}}(\mathbf{r}') X_{j'^{\pi'} n'\alpha}(\mathbf{K}'_{\mathbf{n}}, \mathbf{R}')\Phi_\alpha^C(\xi) \\ + \sum_{\substack{\alpha' \neq \alpha \\ j'^{\pi'} n'}} \tilde{\phi}_{n'}^{j'^{\pi'}}(\mathbf{r}') X_{j'^{\pi'} n'\alpha}(\mathbf{K}'_{\mathbf{n}}, \mathbf{R}')\Phi_{\alpha'}^C(\xi),\end{aligned} \tag{2.23}$$

where as before we select n, j^π as the quantum numbers for the bin corresponding to the final state we are interested in. Now, we will project Eq. (2.5) on $\left\langle \Phi_\alpha^C \tilde{\phi}_n^{j^\pi} \right|$

$$\begin{aligned}\left\langle \Phi_\alpha^C \tilde{\phi}_n^{j^\pi} | H - E | \tilde{\phi}_n^{j^\pi} X_{j^\pi n\alpha} \Phi_\alpha^C \right\rangle + \sum_{j'^{\pi'} n' \neq j^\pi n} \left\langle \Phi_\alpha^C \tilde{\phi}_n^{j^\pi} | H - E | \tilde{\phi'}_{n'}^{j'^{\pi'}} X_{j'^{\pi'} n'\alpha} \Phi_\alpha^C \right\rangle \\ + \sum_{\substack{\alpha' \neq \alpha \\ j'^{\pi'} n'}} \left\langle \Phi_\alpha^C \tilde{\phi}_n^{j^\pi} | H - E | \tilde{\phi'}_{n'}^{j'^{\pi'}} X_{j'^{\pi'} n'\alpha'} \Phi_{\alpha'}^C \right\rangle + \left\langle \Phi_\alpha^C \tilde{\phi}_n^{j^\pi} | H - E | X_A \phi_A \right\rangle = 0\end{aligned} \tag{2.24}$$

We will firstly consider the approximation where the internal degrees of freedom of the core C are "frozen", that is, that they will not be modified during the reaction. This approximation is supported by the sudden nature of the reaction, where, due to the high energy of the incoming proton, the reaction takes place in such a short time that its energy cannot be transferred

to the collective degrees of freedom of the core. From this the dependence of the potentials on the internal degrees of freedom ξ can be ignored, assuming a similar interaction between the nucleon p or N and all relevant states of the core C and the third term of Eq. (2.24) can be eliminated, since no coupling will take place between different states of C.

$$\left\langle \Phi^C_\alpha \tilde{\phi}^{j^\pi}_n | H - E | \tilde{\phi}^{j^\pi}_n X_{j^\pi n \alpha} \Phi^C_\alpha \right\rangle + \sum_{j'^{\pi'} n' \neq j^\pi n} \left\langle \Phi^C_\alpha \tilde{\phi}^{j^\pi}_n | H - E | \tilde{\phi'}^{j'^{\pi'}}_{n'} X_{j'^{\pi'} n' \alpha} \Phi^C_\alpha \right\rangle$$
$$+ \sum_{\substack{\alpha' \neq \alpha \\ j'^{\pi'} n'}} \left\langle \Phi^C_\alpha \tilde{\phi}^{j^\pi}_n | H - E | \tilde{\phi'}^{j'^{\pi'}}_{n'} X_{j'^{\pi'} n' \alpha'} \Phi^C_{\alpha'} \right\rangle + \left\langle \Phi^C_\alpha \tilde{\phi}^{j^\pi}_n | H - E | X_A \phi_A \right\rangle = 0. \tag{2.25}$$

Let us now focus on the last term.

$$\left\langle \Phi^C_\alpha \tilde{\phi}^{j^\pi}_n | H - E | X_A \phi_A \right\rangle = \left\langle \Phi^C_\alpha \tilde{\phi}^{j^\pi}_n | T_R + T_r + H_C + V_{pN} + U_{pC} + U_{NC} - E | X_A \phi_A \right\rangle =$$
$$= \left\langle \Phi^C_\alpha \tilde{\phi}^{j^\pi}_n | T_R + V_{pN} + U_{pC} - E_{cm,i} | X_A \phi_A \right\rangle, \tag{2.26}$$

where we have performed the same transformation as in Eq. (2.12). Now we can add and subtract U_{pA} to the equation, noting that we can cancel $T_R + U_{pA} - E_{cm,i}$ since X_A verifies Eq. (2.14):

$$\left\langle \Phi^C_\alpha \tilde{\phi}^{j^\pi}_n | H - E | X_A \phi_A \right\rangle = \left\langle \Phi^C_\alpha \tilde{\phi}^{j^\pi}_n | V_{pN} + U_{pC} - U_{pA} | X_A \phi_A \right\rangle, \tag{2.27}$$

forming the so-called source term of Eq. (2.25).

We note that the only terms dependent on the internal variables of the core ξ are $\Phi^C_\alpha(\xi)$ and $\phi_A(\mathbf{r}, \xi)$. Therefore we can perform the integral over them:

$$\int \mathrm{d}\xi \Phi^*_{C_\alpha}(\xi) \phi_A(\mathbf{r}, \xi) = \sum_{lj} \tilde{\varphi}^{AC}_{lj\alpha}(\mathbf{r}), \tag{2.28}$$

obtaining the overlap function $\tilde{\varphi}^{AC}_{lj\alpha}(\mathbf{r})$ that only depends on coordinate $\mathbf{r}$. l, j correspond to the orbital and total angular momentum of the removed nucleon that couple A in its ground state and C in state α. The integral from Eq. (2.28) involves in principle the position of all nucleons in nucleus C so it is in general infeasible in most calculations. As such, it is usual to approximate it by a single-particle wavefunction obtained from a simple potential and normalized to 1, $\varphi^{AC}_{lj\alpha}(\mathbf{r})$. The norm is obtained from a nuclear

structure calculation which gives the spectroscopic amplitude, $A^{AC}_{lj\alpha}$, whose square is the spectroscopic factor, $S^{AC}_{lj\alpha}$.

$$\tilde{\varphi}^{AC}_{lj\alpha}(\mathbf{r}) \sim A^{AC}_{lj\alpha}\varphi^{AC}_{lj\alpha}(\mathbf{r}) \tag{2.29}$$

$$S^{AC}_{lj\alpha} = |A^{AC}_{lj\alpha}|^2 \tag{2.30}$$

Let us remark that in this derivation no attention has been paid to the antisymmetrization of identical protons and neutrons. This will gain relevance in Sec. 2.4, but for the present discussion we believe a disgression to treat it would be counterproductive. Furthermore, we will assume that only one l, j configuration will be relevant for the reaction, in order to simplify the notation. With this approximation, Eq. (2.25) results in

$$\begin{aligned}&\left\langle \Phi^C_\alpha \tilde{\phi}^{j^\pi}_n | H - E | \tilde{\phi}^{j^\pi}_n X_{j^\pi n\alpha} \Phi^C_\alpha \right\rangle + \sum_{j'^{\pi'} n' \neq j^\pi n} \left\langle \Phi^C_\alpha \tilde{\phi}^{j^\pi}_n | H - E | \tilde{\phi'}^{j'^{\pi'}}_{n'} X_{j'^{\pi'} n'\alpha} \Phi^C_\alpha \right\rangle \\ &+ A^{AC}_{lj\alpha} \left\langle \tilde{\phi}^{j^\pi}_n | V_{pN} + U_{pC} - U_{pA} | X_A \varphi^{AC}_{lj\alpha} \right\rangle = 0,\end{aligned} \tag{2.31}$$

which expanding the hamiltonian H can be expressed as

$$\begin{aligned}&\left\langle \Phi^C_\alpha \tilde{\phi}^{j^\pi}_n | T_R + T_r + H_C + V_{pN} + U_{pC} + U_{NC} - E | \tilde{\phi}^{j^\pi}_n X_{j^\pi n\alpha} \Phi^C_\alpha \right\rangle + \\ &\sum_{j'^{\pi'} n'} \left\langle \tilde{\phi}^{j^\pi}_n \Phi^C_\alpha | T_R + T_r + H_C + V_{pN} + U_{pC} + U_{NC} - E | \tilde{\phi}^{j'^{\pi'}}_{n'} X_{j'^{\pi'} n'\alpha} \Phi^C_\alpha \right\rangle + \\ &A^{AC}_{lj\alpha} \left\langle \tilde{\phi}^{j^\pi}_n | V_{pN} + U_{pC} - U_{pA} | X_A \varphi^{AC}_{lj\alpha} \right\rangle = 0.\end{aligned} \tag{2.32}$$

Now, for the first and second terms, we note that the kinetic term can be reexpressed as a function of the coordinates in Jacobi set (2): $T_R + T_r = T_{R'} + T_{r'}$. We can then use the fact that the bin wavefunctions are approximately eigenfunctions of the V_{pn} potential:

$$\left\langle \tilde{\phi}^{j^\pi}_n | T_{r'} + V_{pN} | \tilde{\phi}^{j'^{\pi'}}_{n'} \right\rangle = \delta_{nj^\pi, n'j'^{\pi'}} e^n_{pN}. \tag{2.33}$$

We also note that the only dependence on ξ lies in Φ^C_α and H_C, and from

Eq. (2.18) we easily get

$$\left\langle \Phi_\alpha^C | H_C | \Phi_\alpha^C \right\rangle = E_\alpha^C, \tag{2.34}$$

and now from Eq. (2.17) $E_\alpha^C + e_{pN}^n - E = -E_{cm,f}^n$, which can be related to $E_{cm,i}$ through

$$\begin{aligned} E_{cm,f}^n &= E - E_\alpha^C - e_{pN}^n \qquad E_{cm,i} = E - E^A \\ E_{cm,f}^n &= E_{cm,i} + E^A - E_\alpha^C - e_{pN}^n = E_{cm,i} - S_N^A - \varepsilon_\alpha - e_{pN}^n, \end{aligned} \tag{2.35}$$

where S_N^A is the nucleon separation energy for nucleus A and ε_α is the excitation energy of state α of core C.

In order to simplify the notation we will also define $U_{\beta\beta'}(\mathbf{R})$ as

$$U_{\beta\beta'}(\mathbf{R}') = \int \mathrm{d}\mathbf{r}' \tilde{\phi}_n^{j^\pi *}(\mathbf{r}') \left[U_{pC}(\mathbf{r}_{pC}) + U_{NC}(\mathbf{r}_{NC}) \right] \tilde{\phi}_{n'}^{j'^{\pi'}}(\mathbf{r}'), \tag{2.36}$$

where β denotes the numbers required to define the final bin: n, j^π. After these transformations the equations result as

$$\begin{aligned} &\left(T_{R'} - E_{cm,f} + U_{\beta\beta}\right) X_{\beta\alpha} + \sum_{\beta' \neq \beta} U_{\beta\beta'} X_{\beta'\alpha} + \\ &A_{lj\alpha}^{AC} \left\langle \tilde{\phi}_n^{j^\pi} \middle| V_{pN} + U_{pC} - U_{pA} \middle| X_A \varphi_{lj\alpha}^{AC} \right\rangle = 0. \end{aligned} \tag{2.37}$$

It can be put into question whether $\Psi_{b\alpha}^{\mathrm{bin}}$ is a good description of the original three-body wavefunction $\Psi_{b\alpha}^{3b}$. It is long known that wavefunctions obtained through discretization and truncation of the continuum do not reproduce the correct asymptotic behaviour of breakup components [68]. However we note that in the reaction under study we are interested in the wavefunction in the region where $V_{pN} + U_{pC} - U_{pA}$ is large. Since U_{pA} and U_{pC} are effective interactions between the proton and nuclei A and C respectively, we expect them to be similar and thus the so-called *remnant* term $U_{pC} - U_{pA}$ will be quite small. Therefore, we are only interested in the wavefunction in the region where V_{pN} is strong, that is, for small values of r', the relative coordinate between p and N. Since we have chosen the bins to be computed based on the eigenfunctions of V_{pN}, we expect an expansion on them to work well for small values of V_{pN}, which is our region of interest, so $\Psi_{b\alpha}^{\mathrm{bin}}$ should describe well the reaction of interest. In order to verify the adequacy of

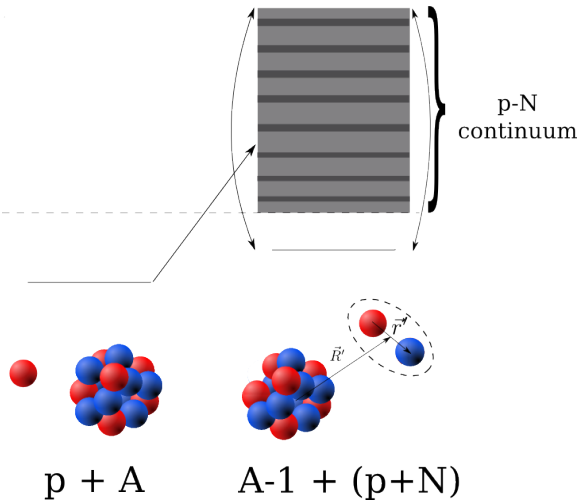

Figure 2.2: Schematics of the Transfer to the Continuum framework. Note that the initial partition $p+A$ serves as the source term for the final partition $(pn)+(A-1)$ as denoted by the single-direction arrow, while all channels in the final partition are coupled to all orders, as denoted by the two-directional arrows.

this approximation, benchmarks with the more rigorous three-body Faddeev formalism have been performed and will be presented in Chapter 3. In Fig. 2.2 the features of the formalism are shown schematically, remarking how the initial $p+A$ serves as a source for the $(pn)+(A-1)$ partition, in which all channels are coupled to all orders.

2.2 Cross sections and momentum distributions

Using standard reaction theory, it is possible to compute the angular differential cross section to a given bin:

$$\frac{\mathrm{d}\sigma_{j^\pi n}}{\mathrm{d}\Omega} = \frac{1}{(2s_p+1)(2J_A+1)} \frac{\mu_{pA}\mu_{pn-C}}{(2\pi\hbar^2)^2} \frac{K'_n}{K_{pA}} \sum_m \left|\mathcal{T}_{if}^{j^\pi n}\right|^2, \tag{2.38}$$

where s_p is the spin of the proton and J_A the one of nucleus A and m denotes the spin projections of the incoming p and A and the outgoing C and pN system. Ω denotes the scattering angle of the core in the center of mass frame. From this cross section it is possible to obtain a double differential cross section on Ω and the energy of the pN system by dividing the cross section by the energy width of the bin $\Delta\epsilon_n = \epsilon_h - \epsilon_l$, assigning the obtained

value of the cross section to the nominal energy of the bin:

$$\left.\frac{\mathrm{d}\sigma_{j^\pi}}{\mathrm{d}\epsilon_{pN}\mathrm{d}\Omega}\right|_{\epsilon_{pN}=\epsilon^n_{pN}} \simeq \frac{1}{\Delta\epsilon_n}\frac{\mathrm{d}\sigma_{j^\pi n}}{\mathrm{d}\Omega}. \tag{2.39}$$

From here we can obtain the distribution on the energy of the core and its scattering angle through energy conservation:

$$\begin{aligned} E_{cm,f} &= E - \epsilon_{C_\alpha} - S^A_N - \epsilon_{pN} \\ E_C &= \frac{m_{pN}}{m_{pN}+m_C}E_{cm,f} \\ \frac{\mathrm{d}\sigma_{j^\pi}}{\mathrm{d}E_C\mathrm{d}\Omega} &= \frac{m_{pN}+m_C}{m_{pN}}\frac{\mathrm{d}\sigma_{j^\pi}}{\mathrm{d}\epsilon_{pN}\mathrm{d}\Omega}, \end{aligned} \tag{2.40}$$

and of course, we can obtain the total double differential cross section summing over all considered angular momenta and parities of the $p{-}n$ subsystem:

$$\frac{\mathrm{d}\sigma}{\mathrm{d}E_C\mathrm{d}\Omega} = \sum_{j^\pi}\frac{\mathrm{d}\sigma_{j^\pi}}{\mathrm{d}E_C\mathrm{d}\Omega} \tag{2.41}$$

Since the cross section is now expressed as a function of the energy and scattering angle of the core, it is rather simple to obtain the momentum distribution of the core in the center of mass:

$$\begin{aligned} E_C &= \frac{p_C^2}{2m_C} \\ \mathrm{d}E_C\mathrm{d}\Omega &= \frac{p_C}{m_C}\mathrm{d}p_C\mathrm{d}\Omega = \frac{1}{m_C p_C}\mathrm{d}^3\mathbf{p_C} \\ \frac{\mathrm{d}\sigma}{\mathrm{d}^3\mathbf{p_C}} &= \frac{1}{m_C p_C}\frac{\mathrm{d}\sigma}{\mathrm{d}E_C\mathrm{d}\Omega}. \end{aligned} \tag{2.42}$$

2.3 Relativistic prescription

Since the reactions we are interested in correspond to a proton accelerated to ∼200-400 MeV, it reaches a speed of 0.57-0.71c. Therefore, relativistic effects are relevant to the reactions involved and must be taken into account in order to obtain a satisfactory description of the experimental results. Relativistic effects appear in two distinct parts of our calculations: in the calculation of the coupled Schrödinger equations and in the kinematic transformations leading to the energy and momentum distributions.

2.3.1 Relativistic corrections to the coupled equations

In Section 2.1, the derivations considered to arrive to the set of coupled equations from Eq. (2.37) were performed assuming non-relativistic kinematics. This is specially apparent in the fact that the equation to be solved is Schrödinger's equation and not Dirac's. In this respect, analyses of various observables from proton-nucleus elastic scattering using Schrödinger and Dirac formalisms were performed in the 90s [69] using the "best" ingredients available at the time and it was found that the description of the observables was equally good for both formalisms, with proton energies ranging from 20 to 800 MeV. We believe these results validate the use of non-relativistic equations to describe (p, pN) reactions at the energies of interests, or paraphrasing [69], relativistic *dynamics* are not necessary to describe these. reactions. On the contrary, relativistic *kinematics*, with the nomenclature from [69], must be taken into account when studying these reactions. In order to have a clearer view on how this affects our coupled equations, let us take the still non-relativistic Eq. (2.37) and multiply it all by $2\mu_{pN-C}/\hbar^2$ keeping in mind that $T_{R'} = -\hbar^2\nabla^2_{R'}/2\mu_{pN-C}$:

$$\begin{aligned}&\sum_{j'\pi' n'}\left(\left(-\nabla^2_{R'} - {K'}^2_n\right)\delta_{\beta\beta'} + \frac{2\mu_{pN-C}}{\hbar^2}U_{\beta\beta'}\right)X_{j'\pi' n' C_\alpha} + \\ &\sqrt{S^{AC}_{lj\alpha}}\frac{2\mu_{pN-C}}{\hbar^2}\left\langle\tilde{\phi}^{j\pi}_n|V_{pN} + U_{pC} - U_{pA}|X_A\varphi_{AC_\alpha}\right\rangle = 0.\end{aligned} \tag{2.43}$$

Unfortunately, there is not a unique prescription to include relativistic kinematics in Schrödinger's equation.

Following the relativistic prescription from [69], we will compute K'_n relativistically from the laboratory energy of the projectile, through standard relativistic formulas which are given in Appendix B. Energy conservation in the initial and final partitions must also be imposed relativistically. The next step in the relativistic prescription is to substitute the reduced mass μ_{pN-C} by the reduced energy ϵ_{pN-C}, defined as

$$\epsilon_{pN-C} = \frac{\epsilon_C\epsilon_{pN}}{\epsilon_C + \epsilon_{pN}}, \tag{2.44}$$

where ϵ_C corresponds to its relativistic energy in the center of mass system

$$\epsilon_C = \sqrt{m^2_C c^4 + \hbar^2 c^2 {K'_n}^2}. \tag{2.45}$$

The same is true for the pN system. However, since we are considering bins which can have a relatively high relative energy between p and N this energy must be included in the nominal mass of the pN system:

$$\epsilon_{pN} = \sqrt{m^{*2}_{pN}c^4 + \hbar^2 c^2 {K'_n}^2} = \sqrt{\left(m_p c^2 + m_N c^2 + e^n_{pN}\right)^2 + \hbar^2 c^2 {K'_n}^2}. \tag{2.46}$$

Let us now introduce a factor γ_β, defined as

$$\gamma_\beta = \frac{\epsilon_{pN-C}}{\mu_{pN-C}}, \tag{2.47}$$

so the substitution of the reduced mass by the reduced energy can be expressed by a multiplication of the potentials by the factor γ_β:

$$\begin{aligned} &\sum_{j'\pi' n'} \left(\left(-\nabla^2_{R'} - {K'}^2_n \right) \delta_{\beta\beta'} + \gamma_\beta \frac{2\mu_{pN-C}}{\hbar^2} U_{\beta\beta'} \right) X_{j'\pi' n' C_\alpha} + \\ &\sqrt{S^{AC}_{lj\alpha}} \gamma \frac{2\mu_{pN-C}}{\hbar^2} \left\langle \tilde{\phi}^{j^\pi}_n | V_{pN} + U_{pC} - U_{pA} | X_A \varphi_{AC_\alpha} \right\rangle = 0, \end{aligned} \tag{2.48}$$

which is a specially convenient way to write the equation since it shows it is possible to modify non-relativistic equations to include relativistic equations by multiplying the involved potentials by the factor γ_β. Note that factor γ depends on the channel considered β and thus changes for different equations.

Let us also remember that X_A was obtained from a Schrödinger's equation which also requires a relativistic modification:

$$\left(-\nabla^2_R + \frac{2\mu_{pA}}{\hbar^2} \gamma_A U_{pA} - K^2_{pA} \right) X_A = 0. \tag{2.49}$$

where K_{pA} is computed relativistically and now γ_A is computed from the reduced energies of p and A.

Another prescription to include relativistic kinematics in Schrödinger's equation can be found in [70] and is very similar to the one described before. The equations are also solved considering the relativistic momentum, but the factor γ_β becomes instead:

$$\gamma_\beta = \frac{2(E - m_A)}{E - m_A + m_p} \quad \text{or} \quad \frac{2(E - m_C)}{E - m_C + m^*_{pN}}, \tag{2.50}$$

where E is the total relativistic center of mass energy.

Different relativistic prescriptions may yield different cross sections and it is not easy to determine which one is most suitable for the different cases. In the following a consistency criterion has been taken: the nucleon-nucleus potentials used in the calculations have been taken from parametrizations which generate the potentials assuming certain relativistic prescriptions for elastic scattering. When using these potentials, the relativistic prescription assumed for their construction has been followed, which is in general the one where $\gamma_\beta = \frac{\epsilon_{pN-C}}{\mu_{pN-C}}$

2.3.2 Relativistic corrections to cross sections and momentum distributions

After including the modifications indicated above in the coupled-channel equations, care must be taken when computing the cross sections and momentum distributions, since, once again, the relativistic relation between energy and momentum must be applied. The relativistic density of states for a certain energy is of special relevance in the relation between the transition matrix and the cross section. Fortunately, there is a rather simple method to correct it in the standard non-relativistic formulas [71], which consists in replacing the reduced mass by the reduced energy defined in Eq. (2.44). As such, the differential cross section can be computed as:

$$\frac{\mathrm{d}\sigma_{j^\pi n}}{\mathrm{d}\Omega} = \frac{1}{(2s_p+1)(2J_A+1)} \frac{\epsilon_{pA}\epsilon_{pn-C}}{(2\pi\hbar^2)^2} \frac{K'_n}{K_{pA}} \sum_m \left|\mathcal{T}_{if}^{j^\pi n}\right|^2, \tag{2.51}$$

where K'_n and K_{pA} are computed relativistically.

The relation between e^n_{pN} and E_C must also be revised, leading to a change in the formula for the cross section Eq. (2.40), where we now define E_C as a the kinetic energy of core C as opposed to its full relativistic energy ϵ_C, and use Mandelstam variable s. More details are found in Appendix B.

$$\frac{\mathrm{d}\sigma_{j^\pi}}{\mathrm{d}E_C \mathrm{d}\Omega} = \frac{\sqrt{s}}{m^*_{pN}} \frac{\mathrm{d}\sigma_{j^\pi}}{\mathrm{d}\epsilon_{pN}\mathrm{d}\Omega}, \tag{2.52}$$

Likewise, the modification for the momentum distribution is rather straightforward:

$$\frac{\mathrm{d}\sigma}{\mathrm{d}^3\mathbf{p_C}} = \frac{1}{\epsilon_C p_C} \frac{\mathrm{d}\sigma}{\mathrm{d}E_C \mathrm{d}\Omega}. \tag{2.53}$$

Here it must be noted that the energy and momentum distributions have been computed for their center of mass values, while there are other reference frames which also appear in the literature, namely, the laboratory frame, where the target nucleus is at rest and the projectile reference frame (*rfp*), where the projectile is at rest. The laboratory frame is the one where the actual measurements take place so it allows for a more direct comparison with experimental data. In experiments in inverse kinematics, where the nucleon is removed from the projectile, the *rfp* frame is of special interest because the effects of the kinematics of the reaction are somewhat removed from the momentum distribution so comparisons of reactions at different energies are most significant in this reference frame. Given the importance of these reference frames, we indicate in the following the relativistic transformations from the center of mass momentum distribution to the ones in laboratory and *rfp* frames. For this let us define p_z, the longitudinal momentum as the component of the momentum parallel to the direction of the projectile beam and p_x and p_y as the perpendicular momentum, that perpendicular to it. Let us note that, as long as neither the projectile nor the target are polarised, the direction of p_x and p_y are irrelevant (given they are perpendicular to the beam) and thus, the distribution on p_x is the same as in p_y. With these definitions we obtain

$$\frac{\mathrm{d}\sigma}{\mathrm{d}p_{Cx}} = \int \mathrm{d}p_{Cy}\mathrm{d}p_{Cz}\frac{\mathrm{d}\sigma}{\mathrm{d}^3\mathbf{p_C}} \tag{2.54}$$

$$\frac{\mathrm{d}\sigma}{\mathrm{d}p_{Cz}} = \int \mathrm{d}p_{Cx}\mathrm{d}p_{Cy}\frac{\mathrm{d}\sigma}{\mathrm{d}^3\mathbf{p_C}} \tag{2.55}$$

$$\left.\frac{\mathrm{d}\sigma}{\mathrm{d}p_{Cx}}\right|_{c.m.} = \left.\frac{\mathrm{d}\sigma}{\mathrm{d}p_{Cx}}\right|_{lab} = \left.\frac{\mathrm{d}\sigma}{\mathrm{d}p_{Cx}}\right|_{rfp} \tag{2.56}$$

$$\left.\frac{\mathrm{d}\sigma}{\mathrm{d}p_{Cz}}\right|_{lab} = \frac{\epsilon_{C(c.m.)}}{\epsilon_{C(lab)}}\left.\frac{\mathrm{d}\sigma}{\mathrm{d}p_{Cz}}\right|_{c.m.} \tag{2.57}$$

$$\left.\frac{\mathrm{d}\sigma}{\mathrm{d}p_{Cz}}\right|_{rfp} = \frac{\epsilon_{C(c.m.)}}{\epsilon_{C(rfp)}}\left.\frac{\mathrm{d}\sigma}{\mathrm{d}p_{Cz}}\right|_{c.m.}, \tag{2.58}$$

$$\tag{2.59}$$

where the momentum and energy of the core C in the different systems are

related to those in the center of mass through standard relativistic formulae:

$$\epsilon_{C(rfp/lab)} = \gamma_{rfp/lab}(\epsilon_{C(c.m.)} - \beta_{rfp/lab} p_{Cz(c.m.)}) \tag{2.60}$$

$$p_{Cz(rfp/lab)} = \gamma_{rfp/lab}(p_{Cz(c.m.)} - \beta_{rfp/lab} \epsilon_{C(c.m.)}) \tag{2.61}$$

$$p_{Cx(rfp/lab)} = p_{Cx(c.m.)}, \tag{2.62}$$

where

$$\beta_{rfp} = \frac{\sqrt{T_p(2m_p + T_p)}}{m_p + T_p + m_A} \qquad \beta_{lab} = -\frac{\sqrt{T_A(2m_A + T_A)}}{m_A + T_A + m_p} \tag{2.63}$$

$$\gamma_{rfp/lab} = \frac{1}{\sqrt{1 - \beta^2_{rfp/lab}}}, \tag{2.64}$$

where T_A is the kinetic energy of nucleus A in the laboratory system (assuming inverse kinematics), while T_p is the kinetic energy of the proton in the *rfp* system, which would give the equivalent direct kinematics, and can be shown to follow the very simple relation:

$$T_p = \frac{m_p}{m_A} T_A. \tag{2.65}$$

2.4 Antisymmetrization: the $(p, 2p)$ case

In this section, we pay special attention to the antisymmetrization of the wavefunction for identical particles in the Transfer to the Continuum reaction formalism, since it has a very important effect in $(p, 2p)$ reactions. We will follow Section 2.11.3 from Satchler's [72]. From Eq. (2.178) in [72] we get that the antisymmetrized transition matrix can be expressed as

$$\mathcal{T}^{(as)}_{\beta\alpha} = \sum_{\Pi_\beta} \epsilon_{\Pi_\beta} \left\langle \Pi_\beta \Psi^{(-)}_\beta | V_\alpha | \Phi_\alpha \right\rangle, \tag{2.66}$$

where for our case $V_\alpha = V_{pn} + U_{pC} - U_{pA}$ and. Π_β corresponds to a permutation between identical particles and the sum is performed over all possible permutations. ϵ_{Π_β} corresponds to $(-1)^{s_{\Pi_\beta}}$ where s_{Π_β} denotes the number of identical-fermion pairs that have been swapped in permutation Π_β. Let us now focus on the $(p, 2p)$ on a nucleus A with Z protons and N neutrons.

For the initial partition $p + A$ there are

$$N_\alpha = \frac{(Z+1)!N!}{Z!1!N!} \tag{2.67}$$

possible permutations (see Eq. (2.167) from [72]), while for the final partition $(2p) + A - 1$, the number of permutations is

$$N_\beta = \frac{(Z+1)!N!}{(Z-1)!2!N!} \tag{2.68}$$

From Eq. (2.174a) from [72] the cross section for the reaction is (non-relativistically)

$$\frac{\mathrm{d}\sigma}{\mathrm{d}\Omega} = \frac{\mu_\alpha \mu_\beta}{(2\pi\hbar^2)^2} \frac{k_\beta}{k_\alpha} \frac{N_\beta}{N_\alpha} \left| \mathcal{T}^{(as)}_{\beta\alpha} \right|^2, \tag{2.69}$$

so

$$\frac{N_\beta}{N_\alpha} = \frac{Z!N!}{(Z-1)!N!} \frac{1!}{2!} = \frac{Z}{2} \tag{2.70}$$

As is standard in transfer reaction theory we must distinguish between the "direct" term and the "exchange" terms. Loosely defined, the "direct" term is the one that requires fewer rearrangements of particle labels to arrive to the final channel. We will now ignore all "exchange terms", deeming our formalism unsuitable to treat them properly. It has been argued before [72] that "exchange" terms contribute little to transfer reactions, and it can be added that the "quasifree" kinematics of the experiments under study further reinforce this approximation, due to the long mean free path of the proton in the nucleus, which will hinder rearrangements during the reaction. Therefore, we expect the exclusion of the "exchange" terms will lead to little effect in the observables. The elimination of the "exchange" terms allows us to keep only the permutations where $Z - 1$ protons and N neutrons are left forming core C in the asymptotic state C_α. This leads to an expression of the final state wavefunction as the 3-body wavefunction $p_1 + p_2 + C$ in the $(p, 2p)$ case, where the nucleons in the core are considered distinct of the incoming and the removed ones.

Therefore, from all possible permutations we are left with only two of them

$$\sum_{\Pi_\beta} \epsilon_{\Pi_\beta} \Pi_\beta \Psi^{(-)} = \Psi^{(-)}(p_1, p_2, C) - \Psi^{(-)}(p_2, p_1, C). \tag{2.71}$$

Now let us recover Eq. (2.28), but now we will use the decomposition found in Eq. (15.34) from [72], which treats properly the antisymmetrization of nucleons inside the nucleus:

$$\Phi_A(\mathbf{r}, \xi) = \frac{1}{\sqrt{A}} \sum_{\alpha, lj} \varphi^{AC}_{lj\alpha}(\mathbf{r}) \Phi^C_\alpha(\xi), \tag{2.72}$$

where the factor $\sqrt{A}$ is included to take into account that there can be A nucleons which can be labelled by the coordinate $\mathbf{r}$. If we distinguish between protons and neutrons we get:

$$\Phi_A(\mathbf{r}, \xi) = \frac{1}{\sqrt{Z}} \sum_{\alpha, lj} \varphi^{AC}_{lj\alpha}(\mathbf{r}) \Phi^C_\alpha(\xi), \tag{2.73}$$

since only a proton wave function may lead from A to C. As before, by imposing that the interaction potentials do not depend on the internal variables of the core we can integrate over them obtaining:

$$\int \mathrm{d}\xi \Phi^{C*}_\alpha(\xi) \phi_A(\mathbf{r}, \xi) = \frac{A^{AC}_{lj\alpha}}{\sqrt{Z}} \varphi^{AC}_{lj\alpha}(\mathbf{r}), \tag{2.74}$$

where as in Sec. 2.1 we will assume that only one l, j configuration for the removed proton can couple the ground state of A and state α of C. Then, the matrix element can be expressed as

$$\mathcal{T}^{(as)}_{\beta\alpha} = \frac{A^{AC}_{lj\alpha}}{\sqrt{Z}} \left\langle \Psi^{3b(-)}_\alpha(p_1, p_2, C) - \Psi^{3b(-)}_\alpha(p_2, p_1, C) | V_\alpha | X_A \varphi^{AC}_{lj\alpha} \right\rangle. \tag{2.75}$$

Now we will try to relate $\Psi^{3b(-)}_\alpha(p_1, p_2, C)$ and $\Psi^{3b(-)}_\alpha(p_2, p_1, C)$. Let us perform the expansion on eigenstates as in Eq. (2.22).

$$\Psi^{3b(-)}_\alpha \simeq \Psi^{\mathrm{bin}(-)}_\alpha = \sum_{j^\pi n} \tilde{\phi}^{j^\pi}_n(\mathbf{r}') X^{(-)}_{j^\pi n\alpha}(\mathbf{K}'_\mathbf{n}, \mathbf{R}'). \tag{2.76}$$

Let us now expand $\tilde{\phi}^{j^\pi}_n(\mathbf{r}')$ employing the LS coupling scheme:

$$\tilde{\phi}^{j^\pi}_n(\mathbf{r}') = \sum_{LS} \tilde{\phi}^{j^\pi}_{nLS}(r') \left[Y_L(\hat{r}') \otimes [\chi_{sp_1} \otimes \chi_{sp_2}]_S \right]_{j^\pi}, \tag{2.77}$$

where χ_{sp} are the spin functions of the protons and Y_L is the spherical harmonic for their relative movement.

If we permute protons 1 and 2 in this model wavefunction we note that $X_{j^\pi n C_\alpha}(\mathbf{K'_n}, \mathbf{R'})$ will not be modified since it only depends on the center of mass of the $p1-p2$ system, which does not change through the permutation. As for $\tilde{\phi}_n^{j^\pi}(\mathbf{r'})$, $\mathbf{r'}$ is the vector going from p_1 to p_2 so it must change sign. This makes a phase $(-)^L$ appear. Also the labels of the spin functions are swapped, but they can be swapped back through Clebsch-Gordan permutation properties:

$$\begin{aligned}\Pi\left(\tilde{\phi}_n^{j^\pi}(\mathbf{r'})\right) &= \sum_{LS} \tilde{\phi}_{nLS}^{j^\pi}(r')\left[Y_L(-\hat{r}')\otimes\left[\chi_{sp_2}\otimes\chi_{sp_1}\right]_S\right]_{j^\pi} \\ &= \sum_{LS}(-)^L(-)^{(-sp_1-sp_2+S)}\tilde{\phi}_{nLS}^{j^\pi}(r')\left[Y_L(\hat{r}')\otimes\left[\chi_{sp_1}\otimes\chi_{sp_2}\right]_S\right]_{j^\pi}.\end{aligned} \tag{2.78}$$

Therefore,

$$\Psi_{C_\alpha}^{3b(-)} \simeq \sum_{j^\pi LSn}(1-(-)^{L+S-1})\tilde{\phi}_n^{j^\pi}(r')\left[Y_L(\hat{r}')\otimes\left[\chi_{sp_1}\otimes\chi_{sp_2}\right]_S\right]_{j^\pi} X^{(-)}_{j^\pi n\alpha}(\mathbf{K'_n}, \mathbf{R'}), \tag{2.79}$$

where we have considered $sp_1 = 1/2$, and it can be seen that for channels where $L+S$ is odd the wavefunction is cancelled, while for $L+S$ even, the wavefunction is doubled. This allows us to relate the antysimmetrized matrix element to the one where particles are distinguishable rather easily

$$\mathcal{T}_{\beta\alpha}^{(as)} = 2\frac{A_{lj\alpha}^{AC}}{\sqrt{Z}}\sum_{j^\pi}^{as}\mathcal{T}_{\beta\alpha}^{j^\pi}, \tag{2.80}$$

where the matrix elements to the right are computed assuming distinguishable particles and the sum over j^π is restricted to values that are not cancelled by the antisymmetrization. Let us express now the cross section from Eq. (2.69):

$$\begin{aligned}\left.\frac{\mathrm{d}\sigma}{\mathrm{d}\Omega}\right|_{(p,2p)} &= \sum_{j^\pi}^{as}\frac{\mu_\alpha\mu_\beta}{(2\pi\hbar^2)^2}\frac{k_\beta}{k_\alpha}\frac{Z}{2}4\frac{SF_{AC_\alpha}}{Z}\left|\mathcal{T}_{\beta\alpha}^{j^\pi}\right|^2 \\ &= 2\sum_{j^\pi}^{as}S_{lj\alpha}^{AC}\frac{\mathrm{d}\sigma^{j^\pi\alpha}}{\mathrm{d}\Omega}.\end{aligned} \tag{2.81}$$

We can see we have reached the very simple result that in order to compute the cross section taking into account antisymmetrization is enough to remove

those channels blocked by antisymmetrization and to double the cross section from the rest of the channels, computed in a standard way considering distinguishable particles.

Let us also note that for the (p, pn) case, once exchange terms are neglected we are left with a $p + n + C$ system, in which the three particles are distinguishable so further antisymmetrization considerations are not necessary:

$$\left.\frac{\mathrm{d}\sigma}{\mathrm{d}\Omega}\right|_{(p,pn)} = \sum_{j^\pi} S^{AC}_{lj\alpha} \frac{\mathrm{d}\sigma^{j^\pi}}{\mathrm{d}\Omega}. \tag{2.82}$$

2.5 Features of the calculation

In this section, some properties of the calculations performed within the Transfer to the Continuum formalism are explored. In particular, we will study the dependence of the cross section on j^π, the effects of distortion and of the relativistic corrections.

2.5.1 Cross section j^π dependence

As was indicated in Chapter 2, the wavefunction corresponding to the final three-body state is expanded in continuum bins with good angular momentum and parity of the $p-N$ subsystem, j^π. Due to the large number of bins, we find that calculations coupling all of them are barely feasible without the use of high-performance-computing facilities. As such, we have chosen to uncouple bins with different total angular momentum and parity j^π. Due to the impossibility of performing the full calculation, it is difficult to assess how strongly this approximation affects the results. As a test to try to evaluate its relevance, a calculation was made for the reaction $^{11}\mathrm{Be}(p, pn)^{10}\mathrm{Be}$ at 200 MeV, as in Sec. 3.2, considering final states only in the $1^\pm$, $2^\pm$ and $3^\pm$ waves. The calculation was performed coupling all six different j^π and its total cross section was compared to the sum of the cross sections from the six calculations resulting from the uncoupling of different j^π. It was found that the total cross sections with coupled and uncoupled states differ only slightly, 0.8%. Admittedly, in order to perform the coupled calculation, the bins had to be broader than in other calculations, so as to decrease the number of coupled channels (in spite of this, the calculation with coupled

channels took one month). As such, in order to be conservative, we consider that the effect of uncoupling the channels with different j^π modifies the cross section for a value of $\sim$5%.

In most of the calculations presented in the following section, we have opted to compute the cross sections for a value of $j^\pi = 5\pm$. For this value, we find the cross section to be adequately converged, as can be seen in Fig. 2.3, where the cross sections leading to states of the $p-N$ subsystem with certain values of j^π are presented in the top panel for the reactions ^{16}O$(p,pn)^{15}$O and ^{16}O$(p,2p)^{15}$N at 451 MeV/A, assuming a removed neutron from the $p_{1/2}$ wave with a spectroscopic factor (SF) of 1.

One feature that becomes apparent from Fig. 2.3 is the lack of 1^+, 3^+ and 5^+ components for the $(p,2p)$ reaction. This is a result from the antisymmetrization of the two outgoing protons, as developed in Sec. 2.4.

In the bottom panel, the cross section for the elastic scattering between proton and neutron and proton and proton (ignoring Coulomb interaction to obtain non-divergent cross sections) is shown as a function of j^π, the relative momentum between the two colliding particles. For this calculation, the Reid93 potential has been considered and the energy of incident particle has been taken as 450 MeV, to reproduce the energy of the ^{16}O(p,pn) and ^{16}O$(p,2p)$ reactions. The similarity of the profiles of (p,pN) and elastic cross sections is remarkable, and is a result of the "quasi-free" nature of the (p,pN) process at these high energies, being the interaction between proton and nucleon the one most strongly affecting the reaction. This also allows us to estimate the effect of the higher j^π excluded from our calculation by computing their contribution to the elastic pn and pp cross section (a much lighter and stable calculation), which confirms that their contribution to the overall cross section is rather small.

2.5.2 Effects of distortion

Given the strength of the potentials at high energies, in particular of their imaginary part, it is expected that they strongly modify the reaction observables. In order to study their effects, in Fig. 2.4, the longitudinal momentum distribution is presented for the reaction ^{15}C$(p,pn)^{14}$C at 420 MeV/A, obtained from a full calculation, as described in Chapter 2 (labelled "Distorted wave"), and from a "plane-wave" calculation, in which all optical potentials

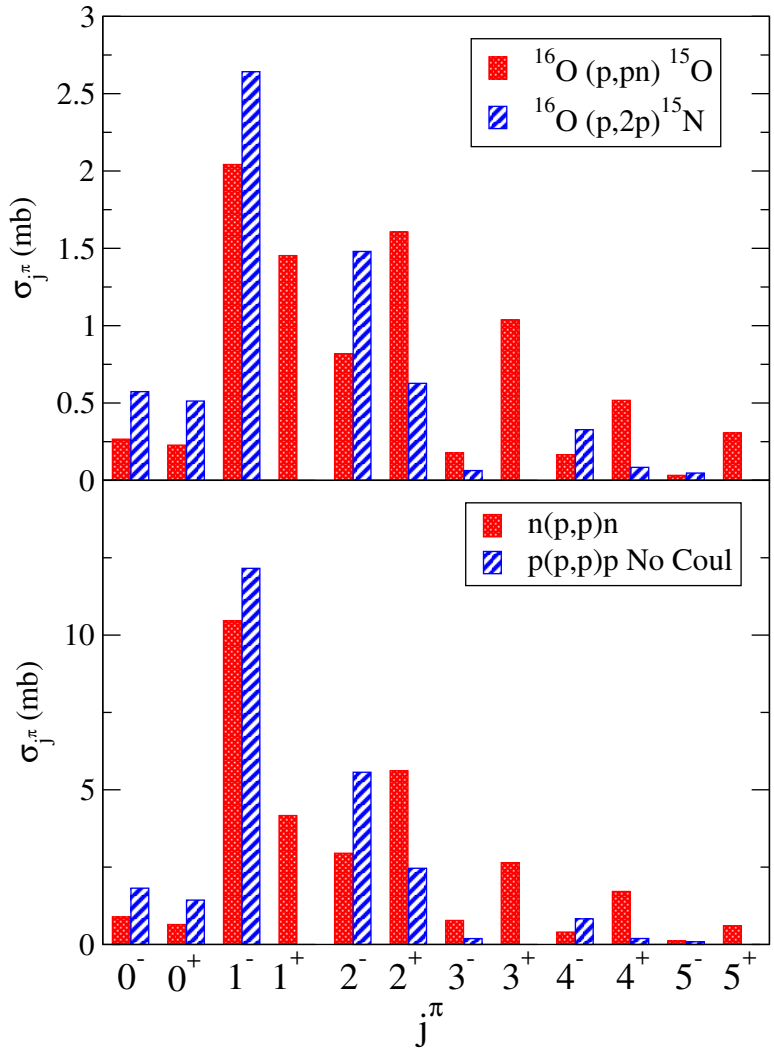

Figure 2.3: Cross section leading to states with a defined j^π, for the $^{16}\mathrm{O}(p,pn)^{15}\mathrm{O}$ and $^{16}\mathrm{O}(p,2p)^{15}\mathrm{N}$ reactions on the top panel, and for the elastic pn and pp cross sections, ignoring Coulomb, in the bottom panel.

$U_{p^{15}\mathrm{C}}$, $U_{p^{14}\mathrm{C}}$ and $U_{p^{14}\mathrm{C}}$ have been removed, only leaving V_{pn} in Eq. (2.37) (labelled "Plane wave"). This is equivalent to a calculation in which a free proton collides with a neutron bound in a wave corresponding to that of the valence neutron of ^{15}C, with neither of them interacting further with the ^{14}C, thus neglecting all distortion and absorption effects. Since no comparison to experimental data will be considered, the removed neutron is assumed to populate a $2s$ state with $SF = 1$.

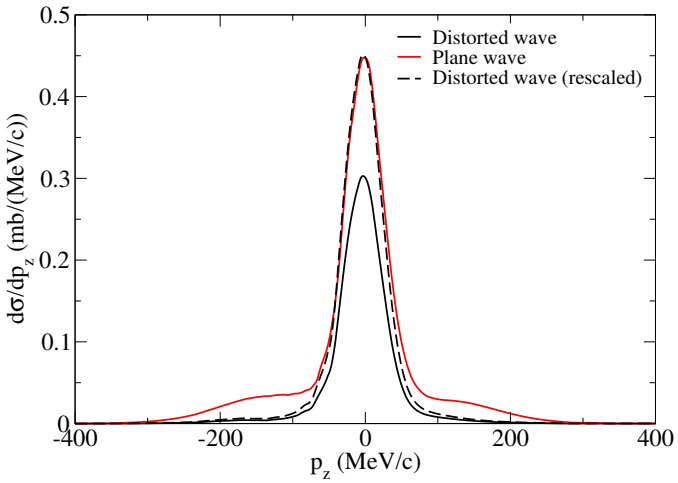

Figure 2.4: Longitudinal momentum distribution for $^{15}\mathrm{C}(p,pn)^{14}\mathrm{C}$ at 420 MeV/A. Calculations including and excluding distorting potentials are presented. The calculation including distortion is also shown rescaled to give the peak of the calculation without distortion.

As can be seen in Fig. 2.4, the inclusion of distortion effects strongly reduces the cross section, which is of 40.6 mb for the plane-wave calculation and falls to 21.9 mb when considering distortion and absorption. It also modifies the shape of the momentum distribution, which can be more clearly seen comparing the plane-wave curve to the rescaled distorted-wave one. The most remarkable modification is the severe reduction of the shoulders of the distribution in the distorted-wave calculation. This reduction can be understood from the PWIA description of the reaction, where the momentum distributions are found to be proportional to the Fourier transform of the wave function of the bound nucleon times the free nucleon-nucleon cross section (times a phase-space factor that should not be too relevant at these high energies [50]). In the Fourier transform, the shoulders seen in the plane-wave calculation appear because the wavefunction presents a node (being a

$2s_{1/2}$ state) at small distances ($\sim$ 2 fm). At these small distances, the effects of absorption are intense so, when they are considered, the reaction loses sensitivity to this part of the wavefunction and the effect of the node (the appearance of shoulders) is reduced in the final momentum distribution.

In ^{15}C the valence neutron has a very low binding energy, $S_n = 1.22$ MeV, and it is an established halo nucleus. As such, its wave function extends to large distances when compared to other nuclei in its vicinity. This makes it likely that the effects of the distorting potentials are somehow reduced, since the "collision" between the proton and the neutron may happen at large distances of the core, where the effects of the potential are not that strong. It would be also desirable to check the effects of distortion on waves which do not include a node, to explore how the shapes of their momentum distributions are modified by distortion.

In order to answer these questions, in Fig. 2.5, the reaction $^{22}\mathrm{O}(p,pn)^{21}\mathrm{O}$ is explored in a similar way to that of Fig. 2.4. For this nucleus the binding energy is larger, $S_n = 6.85$ MeV, and the nucleus is no longer a halo. The valence neutrons for ^{22}O populate both the $2s_{1/2}$ and the $1d_{5/2}$ waves, so that realistic calculations can be performed for both waves. As before, the removed neutron is assumed to populate either the $2s_{1/2}$ or the $1d_{5/2}$ waves with $SF = 1$. In this figure, transversal momentum distributions are presented along longitudinal momentum distributions.

Looking at the longitudinal momentum distribution for the $2s_{1/2}$ wave, it is apparent that the reduction of the cross section is stronger than in the ^{15}C case, the cross section dropping from 44.2 mb without distortion to 8.9 mb with it. As for the shape the same overall features than for ^{15}C are found, with a reduction of the relative importance of the shoulders due to absorption. This can be understood due to the larger binding energy, which restricts the neutron wave function to smaller distances to the core, at which the effects of the potentials, and in particular the absorption, are more intense. There is also a slight shift in the distribution which could also be noticed in the ^{15}C case, being somewhat larger for ^{22}O. This shift can be understood as being due to distortion effects shifting the momentum distribution, as discussed in [50]. However, the shift is so small that it could be a numerical artifact.

The reduction in cross section for the $1d_{5/2}$ is similar, going from 44.5 mb to 8.7 mb. The width of the distribution is reduced by the distorting

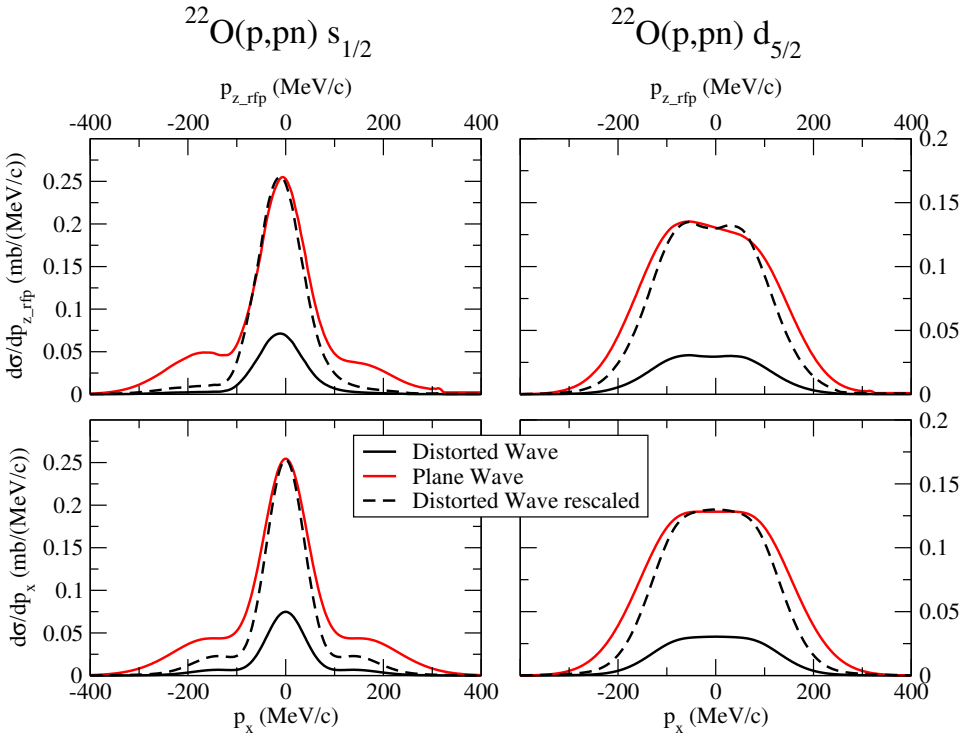

Figure 2.5: Longitudinal and transversal momentum distribution for $^{22}\mathrm{O}(p,pn)^{21}\mathrm{O}$ at 415 MeV/A. Longitudinal momentum distributions are presented in the top row, while transversal momentum distributions are presented in the bottom. The left column corresponds to a neutron removed from the $2s_{1/2}$ wave while the right one corresponds to the $1d_{5/2}$ wave. Calculations including and excluding distorting potentials are presented. The calculation including distortion is also shown rescaled to give the peak of the calculation without distortion.

potentials. This can once again be understood noting that the potential is highly absorptive at small distances. This makes the reaction sensitive only to the value of the wavefunction at large distances, effectively resulting in a "more extended" wave function, whose Fourier transform is narrower. Similar effects have been described for nucleon knockout reactions with heavier targets [73].

The distorted longitudinal momentum distribution for $1d_{5/2}$ shows a smaller asymmetry than the "plane-wave" one. There is no simple picture to describe this behaviour, which results from two competing effects: one is the distortion of the momentum distribution by the real part of the distorting potential (described in [50]) and the other is the absorption of configurations

with uneven energies between proton and neutron. These configurations lead to asymmetry in the "plane-wave" momentum distribution, because they are related to different free nucleon-nucleon cross sections, as shown in Fig. 2.6, but they are strongly absorbed in "distorted-wave" calculations because they result in one of the particles having a small energy with respect to the core, which make it more likely to be absorbed. As such, these asymmetry-generating configurations are reduced in the "distorted-wave" calculation, leading to some restoration of the asymmetry. The asymmetry of the distorted momentum distribution thus depends on a complicated interplay between effects, which does not permit a simple explanation.

Since the momentum distribution for the s-wave is more strongly peaked, it is more accurately described by the quasi-free mechanism, and the effect described above is less likely to become apparent.

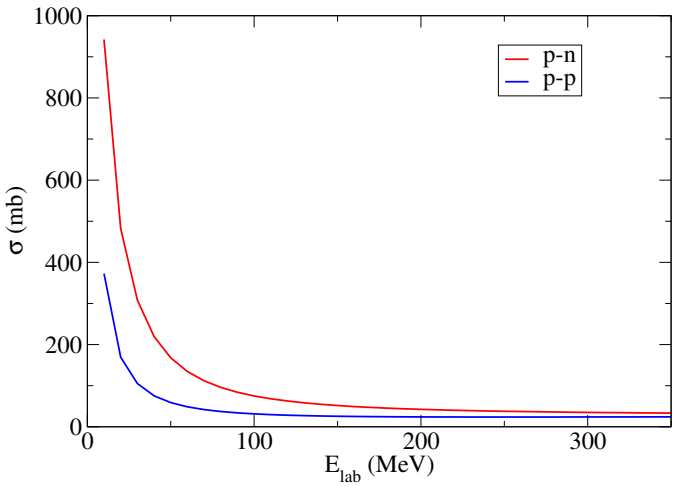

Figure 2.6: Free $p-n$ and $p-p$ cross section (ignoring Coulomb) as a function of the laboratory energy, computed with the Reid93 potential assuming $J = 5$ maximum angular momentum between proton and nucleon.

The transversal momentum distributions show similar features to the longitudinal ones, with the exception of the shift and asymmetry, since transversal momentum distributions are symmetric thanks to rotational invariance.

2.5.3 Relativistic effects

Given the large energies ($\sim$ 200-400 MeV/A) at which (p, pn) and $(p, 2p)$ reactions have been measured, relativistic effects, englobed in the relativistic prescriptions described in Sec. 2.3, are bound to influence strongly reaction observables. In order to quantify their importance, in Fig. 2.7 the longitudinal momentum distribution for $^{15}\mathrm{C}(p, pn)^{14}\mathrm{C}$ is presented for two incident energies, 100 and 420 MeV/A. The longitudinal momentum distribution is computed with and without the relativistic corrections from Sec. 2.3. As can be seen in the figure the effects of the relativistic prescription is much more important for an incident energy of 420 MeV/A, where their inclusion increases the cross section by 45%, than for an incident energy of 100 MeV/A, where the cross section is modified only 3%. If compared to the results from Fig. 3.5, which correspond to the same reaction, the effects of relativistic corrections are somewhat larger in this comparison. This arises from the choice of optical potentials, which are taken from Dirac parametrization here, while in Fig. 3.5 were taken from Köning-Delaroche (KD) parametrization. Since Dirac potentials are deeper than KD ones, the effect of relativistic corrections (multiplying by γ from Eq 2.47) over them is more important when using Dirac potentials.

It is remarkable that the shape of the distributions are not modified much by the relativistic corrections giving virtually coinciding shapes. This can be understood because the factor γ does not change much for the different final states considered. Therefore, to a first approximation it can be seen as a global factor which affects the overall cross section, not modifying much the shape of the momentum distributions.

It is also of note how different the two momentum distributions are, despite corresponding to a neutron removed from the same orbital. The reason is twofold: first, at 100 MeV, the impulse approximation, which allows to establish a clear relation between the momentum distribution and the Fourier transform of the bound nucleon wave function, breaks down. Secondly, even if we assume that the momentum distribution can still be described as the wave function Fourier transform times the nucleon-nucleon cross section, at lower incident energies the nucleon-nucleon cross section is evaluated at lower energies, which, as can be seen in Fig. 2.6, correspond to a much steeper variation of the cross section, which alters heavily the

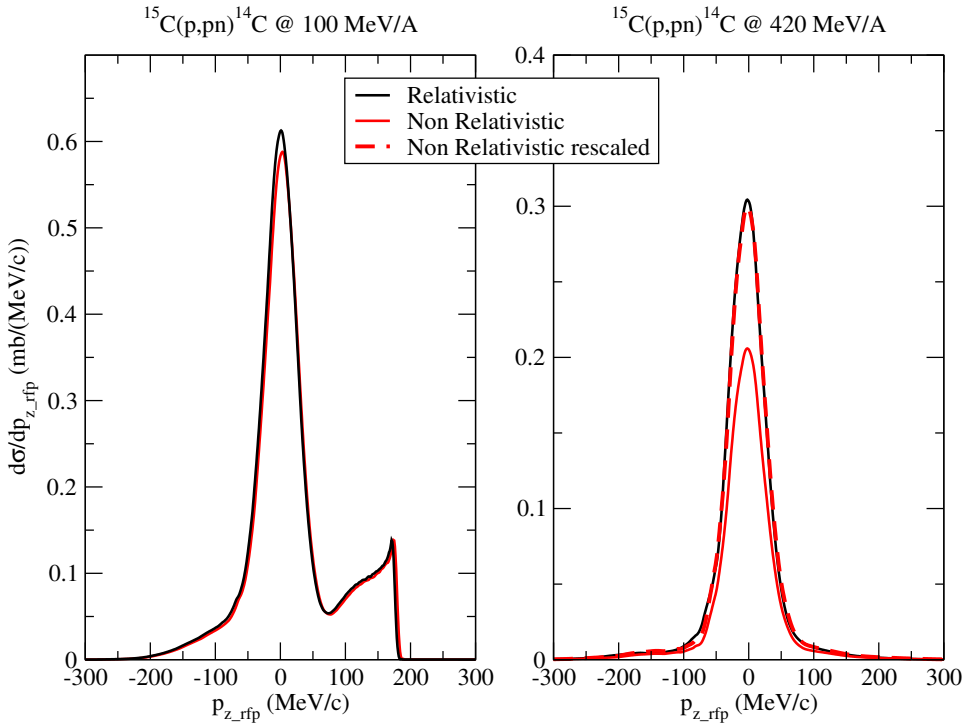

Figure 2.7: Longitudinal momentum distribution for the $^{15}\mathrm{C}(p,pn)^{14}\mathrm{C}$ reaction at 100 MeV/A and 420 MeV/A with and without the relativistic corrections described in Sec. 2.3. For the energy 420 MeV/A the calculation without relativistic corrections is shown rescaled to reproduce the cross section of the calculation with relativistic corrections for the sake of comparison.

momentum distribution. In particular, this explains the increase of the cross section at high momenta for the incident energy of 100 MeV/A, since these high momenta correspond roughly to a high energy of the core in the center of mass system, which in turn, through conservation of energy, relates to a small proton-nucleon energy, which leads to a high cross section.

Chapter 3

Benchmark with other reaction formalisms

Science is really about individual experts
reaching a consensus

Alan Stern

Before comparing with experimental data, we assess the reliability and accuracy of the proposed reaction formalism against other methods used in the literature for the analysis of (p, pN) data.

As such, benchmark calculations are presented in this chapter for (p, pn) reactions where the Transfer to the Continuum (TC) formalism is compared to other reaction formalisms. Two reactions are analysed, ^{15}C$(p, pn)^{14}$C for a proton energy of 420 MeV/c, which is compared to DWIA (Distorted-Wave Impulse Approximation) and to published results employing the Faddeev/AGS formalism [57]; and ^{11}Be$(p, pn)^{10}$Be at 200 MeV per nucleon, which is compared to the Faddeev/AGS formalism. For each reaction a description of the different inputs of the calculation is presented followed by the results of the calculations, which will be focused on the momentum distributions of the outgoing core.

3.1 ^{15}C$(p, pn)^{14}$C at 420 MeV/A

The DWIA calculations shown in this section were performed by Dr. K. Yoshida and Dr. K. Ogata, to whom the author of this thesis is greatly

thankful.

3.1.1 Inputs and details for the calculation

In this subsection, the inputs for the Transfer to the Continuum calculation performed for the benchmark are presented, as well as specific details of the calculation.

The bound state for the neutron has been computed as the eigensate of a Woods-Saxon potential:

$$V(r) = \frac{V_0}{1 + e^{\frac{r - r_0 A^{1/3}}{a_0}}}, \tag{3.1}$$

corresponding to the quantum numbers $2s_{1/2}$. The parameters for the potential are taken as $r_0 = 1.25$ fm, $a_0 = 0.65$ fm and $A = 14$, corresponding to the outgoing core. The depth of the potential V_0 is varied in order to obtain the desired separation energy. The ^{14}C core is assumed to have angular momentum and parity 0^+, so that the ground state of ^{15}C corresponds to a $1/2^+$ state.

The distorting potentials p–^{15}C, p–^{14}C and n–^{14}C are taken from the EDAD2 parameter set from Dirac phenomenological parametrization [45, 46]. These potentials are produced for a Schrödinger equation following the relativistic prescription from [69]. Therefore, this same prescription is followed in the TC calculations. This prescription gives potentials which are energy dependent. In the initial partition, p+^{15}C, the energy is defined by the laboratory energy of the proton, which is taken as 420 MeV. For the final partition, $p + n$+^{14}C, however, the energy between p and ^{14}C and between n and ^{14}C, is not defined for the final states considered in TC, where the energy that is defined is the one between ^{14}C and the pn pair. The "quasifree" nature of the (p, pn) reaction at high proton energies results in the most likely outcome of the reaction being an equal distribution of energy between the incoming proton and the removed neutron. As such, we have chosen for the outgoing potential of the p+^{14}C and n+^{14}C pairs the one resulting from the EDAD2 Dirac parametrization at half the proton incident energy, that is, 210 MeV. In the DWIA formalism, the outgoing energies of the proton and neutron are well defined for the final states studied. This allows us to study the effect of the described choice of the outgoing potential in the reaction

observables.

The $p-N$ potential is paramount for the description of the (p, pn) reaction, since it is the main interaction that drives the reaction. For it, we have chosen the Reid93 [74] parametrization, a revision and extension of the Reid Soft Core potential [75], developed by the Nijmegen group. This potential consists of central, spin-orbit and central terms and it has been fitted to describe elastic $p-n$ and $p-p$ scattering observables for energies up to 350 MeV (see Appendix C). Although the energy of the incoming proton (420 MeV) is higher than the maximum for which the Reid93 potential was fitted, given the smooth energy dependence of the $p-n$ scattering cross section, we expect this potential to describe accurately the $p-n$ interaction at the energies of interest.

In order to have a more meaningful comparison with the DWIA formalism, the so-called *remnant* of the transfer vertex is neglected in the TC calculations: $U_{pC} - U_{pA} = 0$.

In the TC calculations, the maximum angular momentum of the $p-n$ subsystem was taken as $J_{max} = 5$. In order to be consistent between the DWIA and TC formalisms, the double differential cross section in energy and angle was produced for the free $p-n$ reaction with the restriction $J_{max} = 5$ and read in the DWIA calculation. Given the small contribution of higher angular momenta to the free $p-n$ cross section, it is expected that the contributions left out are small and will not modify the conclusions of the benchmark.

As described in Sec. 2.5.1, we uncouple the states with different $p-n$ angular momentum and parity. Given the uncertainties in the cross sections due to the choice of potentials and the limits of the calculations, we deem this approximation to be well justified.

Different binning meshes for the outgoing channels have been taken for the calculations for different angular momenta and parities of the final $p-n$ system. For the angular momenta and parities $j^\pi = 0, 1, 2^\pm$ the bins are evenly spaced in energy with a width $\Delta E = 10$ MeV for a $p-n$ energy between 30 and 330 MeV. For $j^\pi = 3^\pm$, the width was increased to $\Delta E = 15$ MeV while for $j^\pi = 4, 5^\pm$ it was taken as $\Delta E = 25$ MeV. The reason for the increase in the width is twofold: first, the majority of the cross section was found to correspond to $j^\pi = 1, 2^\pm$, so a smaller width should be taken for these states in order to have a better description of these states, which

will give most of the cross section. Second, calculations are both heavier and more unstable for larger j^π, due to the increase of channels coupled for each total angular momentum and to the steeper centrifugal barrier faced by the bin wavefunctions. A reduction in the number of channels through the use of fewer broader bins helps to achieve numerical stability for the calculations.

The maximum total angular momentum for the calculation was taken as $J_{max} = 60$, where the contribution to the cross section was less than 0.05% of the total cross section. Larger total angular momenta proved very unstable, in particular for calculations with the bigger $p - n$ angular momenta.

3.1.2 Results

In this section the results for the benchmark calculation are presented. Most of these results have been published in [49]. First, in Fig. 3.1, we present the results corresponding to the benchmark employing the experimental neutron separation energy for ^{15}C, $S_n = 1.22$ MeV. The observable studied is the longitudinal momentum p_z distribution of the outgoing ^{14}C in the rest frame of ^{15}C. In the figure, the panel to the left corresponds to the full calculation as described in the previous section. We can see that the agreement between TC and DWIA calculations is excellent both in shape and magnitude. A few minor differences can be seen, but they are likely to be produced by the interpolations and averages trough which the differential cross section is computed from the TC calculation (see Sec. 2.2).

In order to explore the effect of the distorting potentials in the degree of agreement, a "plane-wave" calculation has been performed in which the distorting potentials have been switched off. This also allows us to explore the effect of absorption and distortion in the cross section for this case. The results are presented in the right panel of Fig. 3.1. As can be seen, the agreement keeps being excellent, though the peak seems to be a bit larger in the plane-wave impulse approximation (PWIA) calculation and the left shoulder presented by the distribution is a little larger as well. However we find the differences too small to be significant.

In the figure the effect of the distorting potentials can be also analysed. We see that the shape of the cross section is changed: the "plane-wave" calculation presents two very marked shoulders which are greatly reduced in the full calculation. The cross section is highly reduced as well. For the TC

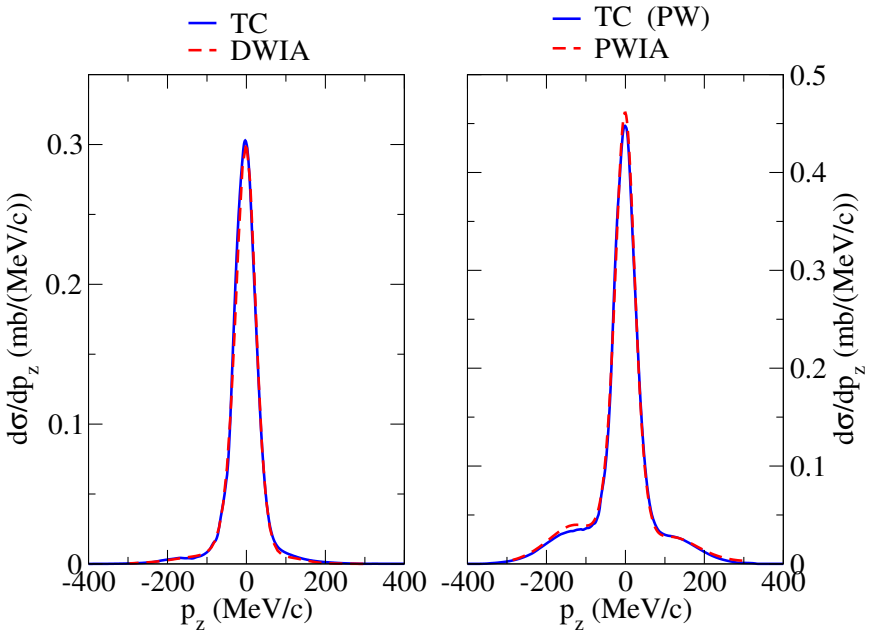

Figure 3.1: Benchmark calculation between TC and DWIA formalisms for ^{15}C$(p, pn)^{14}$C at a proton energy of 420 MeV. The left panel corresponds to the full calculation where the distorting potentials have been considered as described in Sec. 3.1.1. The right panel corresponds to a "plane-wave" calculation, where the distorting potentials are set to 0.

calculation, the cross section computed is of 40.6 mb for the "plane-wave" calculation, while for the full calculation it is reduced to basically half this value: 21.9 mb. Both effects can be understood by the highly absorptive nature of the distorting potentials: This absorption greatly reduces the outgoing flux, and with it the overall cross section for the considered (p, pn) channel. As for the shoulder structure, it can be seen that it originates from the Fourier transform of the wavefunction of the removed nucleus, and in particular from it corresponding to a $2s$ state, whose wave function presents a node. In order for the cross section to be sensitive to that node, it is necessary that the small distances where it can be found are explored by the reaction. Since absorption increases at small distances between the proton and ^{15}C, the proton is likely to be absorbed prior to exploring such deep parts of the neutron wavefunction. Therefore, the ratio of the shoulders, which can be related to the inner parts of the wavefunction, to the peak, which explores the outermost parts of the wavefunction, is reduced when including absorption in the calculation.

Nucleus ^{15}C has a low neutron binding energy which in turn results in a halo structure where, for the geometry chosen for this work, the root mean square radius has the very large value of 5.5 fm. At these large distances the effects of distorting potentials are diminished and the reaction can be understood through a simply geometrical description, where the cross section is merely related to the likelihood of finding the neutron outside of a certain absorption area. Therefore, it can be argued that the agreement of both formalisms is a product of the simplicity of the reaction mechanism in this particular case. In order to explore the evolution of the agreement when this simple picture is weakened we have computed two reactions where the separation energy of the neutron has been increased artificially to 5 and 18 MeV. The results for these calculations are shown in Fig. 3.2. As can be seen in the figure the agreement remains remarkably good for the two new calculations although in the case with $S_n = 18$ MeV the TC calculation seems to overestimate the high momentum tail when compared to the DWIA calculation. To this respect, it was found that in the DWIA calculation this tail was particularly sensitive to the choice of E_{pn}, the energy at which the free $p - n$ cross section is evaluated (see Eq. (1.12)), as is shown in Fig. 3.3. In the figure *initial* corresponds to computing the energy from κ, *final* corresponds to κ' and *average* to the average of both energies. As can be seen

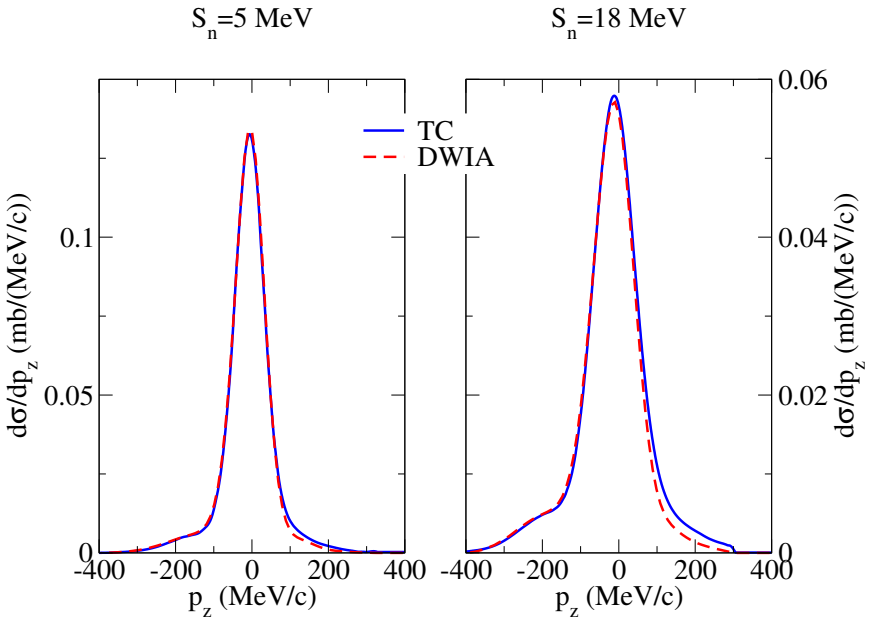

Figure 3.2: Benchmark calculation for the same reaction as Fig. 3.1, where the separation energy has been artificially increased to $S_n = 5$ and 18 MeV.

the differences between these choices are not too important at this incident energy, but they alter somewhat the agreement with the Transfer to the Continuum calculation in the peak and tail.

Let us remark that this ambiguity in the choice of E_{pn} stems from the approximation of $|t_{pn}|^2$ by $\frac{\mathrm{d}\sigma}{\mathrm{d}\Omega}$, the free $p-n$ cross section. When t_{pn} is accessible for different initial and final energies (off-shell t-matrix) in the DWIA calcualtion, it is not necessary to make an on-shell approximation. From the results presented in Figs. 3.1, 3.2 we conclude that the agreement between both formalisms is satisfactory within the uncertainties of each formalism, and consider that the benchmark shows them as fully consistent.

One of the main difficulties faced by the Transfer to the Continuum formalism is the loss of the information on the relative energy between n and core and p and core. Since in the formalism optical potentials that depend on energy are used, this lacking information opens the question of which energy should be used when evaluating the potential. As mentioned in Sec. 3.1.1, we opted to use the potentials at half the incident energy, but we are left to ponder how this choice affects the results. The DWIA formalism retains the information on the relative energy and can select the

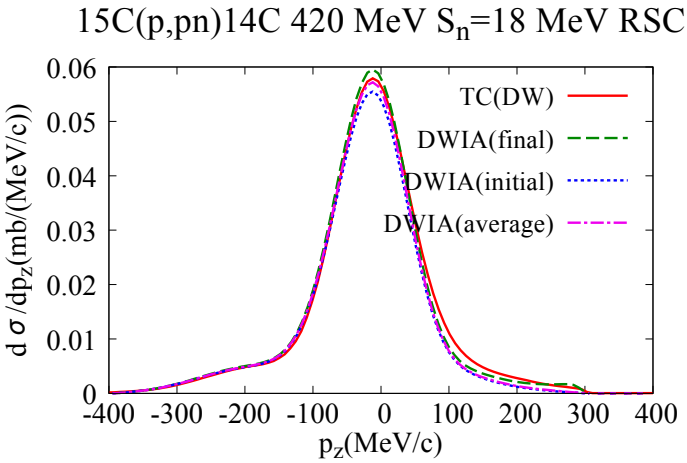

Figure 3.3: Dependence of the DWIA momentum distribution on the selection of E_{pn}, the energy of evaluation of the free $p-n$ cross section.

corresponding potentials at the relative energy for each final configuration (see Eq. (1.16)). Thus, we can compare DWIA calculations using the same prescription for the potentials as the Transfer to the Continuum and using the distorting potentials corresponding to the relative energies for each outgoing configuration. This should illustrate the effect on the observables of the choice of potentials made in the Transfer to the Continuum calculations. The corresponding calculations are shown in Fig. 3.4. In the figure, EI-DWIA corresponds to the DWIA calculation where the outgoing potentials are fixed to half the incident energy, while ED-DWIA corresponds to the calculation where the outgoing potential has been computed based on the relative $p-^{14}$C and $n-^{14}$C energy for each outgoing state. As can be seen in the figure, in general the inclusion of the energy dependence of the potential increases the shoulders and tails of the distributions, while reducing the peak contribution. The total cross section is however not changed much, being reduced by 3.4% for $S_n = 1.22$ MeV, by 3% for $S_n = 5$ MeV and increased by 0.4% for $S_n = 18$ MeV. From this, we may expect the momentum distributions obtained using the choice of potentials taken in the Transfer to the Continuum to give cross sections close to those obtained using the energy-dependent potentials, although the momentum distributions may be somewhat narrower with higher peaks and reduced tails. This issue will be relevant when comparing to experimental data in Chapter 4.

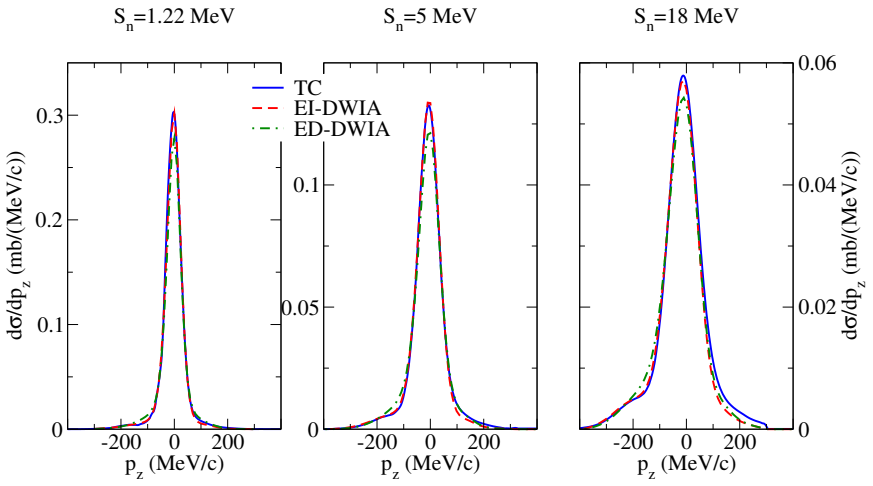

Figure 3.4: Distorted wave results from Figs. 3.1, 3.2 compared to DWIA results where outgoing potentials are calculated for each of the outgoing configurations.

3.1.3 Comparison with published Faddeev/AGS results. Effect of relativistic corrections

The reaction ^{15}C$(p,pn)^{14}$C at a proton energy of 420 MeV was studied using the Faddeev/AGS formalism in [57]. There, the study of the reaction was performed using non-relativistic kinematics. As such, their results could not be compared to those from the DWIA calculation, which was implemented fully relativiscally. However, we were able to compare them to the Transfer to the Continuum calculations by removing the relativistic corrections described in Sec. 2.3.

In order to have a more meaningful comparison we employ the potentials presented in [57], which for completion are presented in Table 3.1. We also include the potential for p+^{15}C. In the Faddeev/AGS formalism this potential is not required as an input, since the p+^{15}C is built from the binary interactions between p and n and p and ^{14}C. However, in the Transfer to the Continuum formalism this is not the case and a certain choice of this potential must be provided as an input. For consistency and convenience, we have chosen to generate this potential from the Köning-Delaroche (KD) parametrization [76] evaluated at 200 MeV, as the $p,n-^{14}$C potentials were taken. The potentials present a Woods-Saxon-shaped real part and an imag-

inary part with Woods-Saxon and Woods-Saxon-derivative components:

$$V(r) = -\frac{V_0}{1+e^{\frac{r-r_0A^{1/3}}{a_0}}} - i\frac{W_0}{1+e^{\frac{r-r_0A^{1/3}}{a_0}}} - 4iW_s\frac{e^{\frac{r-r_{0s}A^{1/3}}{a_{0s}}}}{\left(1+e^{\frac{r-r_{0s}A^{1/3}}{a_{0s}}}\right)^2}, \quad (3.2)$$

where A is taken as 14, corresponding to the core. From the cases presented

	V_0 (MeV)	W_0 (MeV)	r_0 (fm)	a_0 (fm)	W_s (MeV)	r_{0s} (fm)	a_{0s} (fm)
$V_{p-^{14}\mathrm{C}}$	13.121	13.115	1.136	0.676	0.195	1.304	0.526
$V_{n-^{14}\mathrm{C}}$	16.161	11.044	1.136	0.676	0.138	1.304	0.542
$V_{p-^{15}\mathrm{C}}$	13.345	13.121	1.140	0.676	0.205	1.303	0.527

Table 3.1: Parameters for the König-Delaroche potentials used in the calculation.

in [57] we have chosen the one explored in the previous benchmark: a neutron removed from a $2s$ state with separation energy $S_n = 1.22$ MeV. We present the transversal momentum p_x distribution in Fig. 3.5. In the figure, in the left panel, the Faddeev/AGS calculation taken from [57] is presented in a blue solid line, while two Transfer to the Continuum calculations are presented: the red dot-dashed line corresponds to a calculation without relativistic corrections while the green dashed line includes them. It can be seen that the agreement between the Faddeev/AGS and non-relativistic Transfer to the Continuum calculation is excellent. Since the Faddev/AGS calculation was computed non-relativistically we conclude that Transfer to the Continuum and FaddeeV/AGS give fully consistent results. It must be remarked that the V_{pn} interaction used in both calculations is different: the Faddeev/AGS calculation employs CD-Bonn interaction [77] while the Transfer to the Continuum uses Reid93, as mentioned above. In the elaboration of this study, we were not able to implement CD-Bonn potential in our reaction code, so a comparison using the same V_{pn} interaction was not feasible. However, we must note that both potentials reproduce experimental $p-n$ phaseshifts up to energies of hundreds of MeV, so they present the same on-shell behaviour and should yield very similar observables in the (p, pn) reaction. In order to isolate the effect of the V_{pn} interaction, in the right panel a "plane-wave" calculation is presented where all the distorting potentials have been set to 0, which can be compared to a similar calculation shown in [57]. The agreement is still excellent, from where we conclude that both interactions

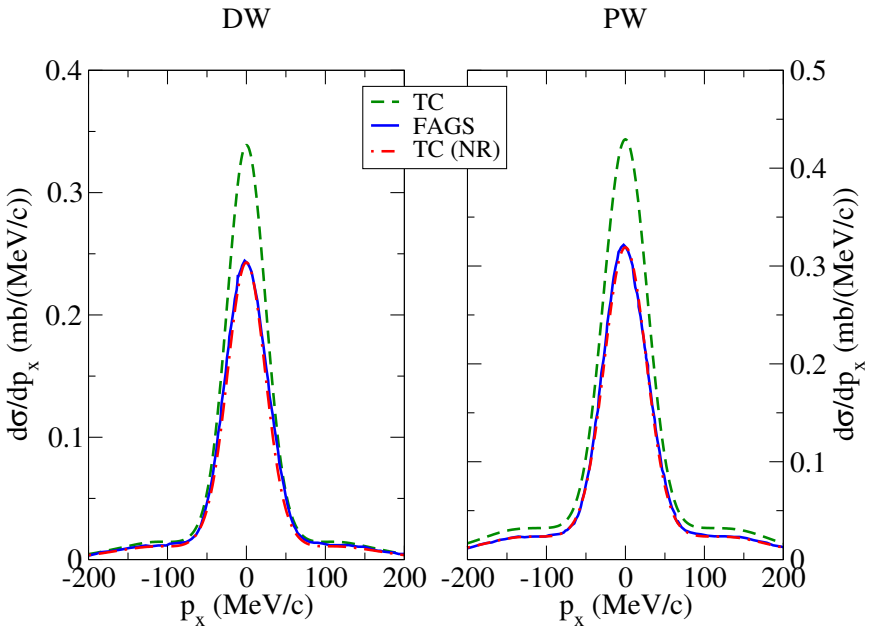

Figure 3.5: Transversal momentum distribution for ^{15}C$(p, pn)^{14}$C at 420 MeV proton energy computed using the Faddeev/AGS formalism through non-relativistic equations and using the Transfer to the Continuum formalism with (green dashed line) and without (red dot-dashed line) relativistic corrections. The left panel shows the full calculation while the right one shows the "plane-wave" calculation where all distorting potentials are set to 0.

seem to result in the same cross sections, which should not be surprising since both reproduce the same free $p - n$ observables.

We must mention that the inclusion of the relativistic prescription results in a marked increase in the cross section computed for the Transfer to the Continuum formalism, of around 30%, which corresponds roughly to the factor γ^2 (see Eq. (2.47)) when following the prescription from [69]. We conclude from here that relativistic corrections can severely affect the cross sections obtained and therefore must be taken into account when trying to obtain information from comparing theoretical calculations to experimental data.

3.2 ^{11}Be$(p, pn)^{10}$Be at 200 MeV/A

In this case we perform non-relativistic calculations, since the Faddeev/AGS implementation is non-relativistic. As such we have chosen a lower proton energy (200 MeV) so as not to be so influenced by relativity. This energy is also chosen because it is the upper limit for the prescription used for the distorting potentials: Köning-Delaroche's [76]. The Faddeev/AGS calculations shown in this section were performed by Dr. A. Deltuva, to whom the author of this thesis is greatly thankful.

3.2.1 Inputs and details for the calculation

In this calculation all excitations of ^{10}Be will be ignored. In reality the ground state of ^{11}Be has a finite overlap with the excited state ^{10}Be(2^+)[78], but for the sake of simplicity we will assume a ground state for ^{11}Be with only one channel: ^{10}Be(0^+).

As in the previous benchmark, the bound state for the neutron has been generated with a Woods-Saxon potential, which in this case has the following geometry: $R_0 = 1.39 \times 10^{1/3}$ fm, $a_0 = 0.52$ fm. The depth of the potential is adjusted to obtain the eigenstate at the neutron separation energy $S_n = 0.5$ MeV.

For the distorting potentials $p-^{10}$Be, $n-^{10}$Be the KD parametrization has been used, selecting a nucleon energy of 200 MeV for its evaluation. In the Faddeev/AGS calculation, for the $n-^{10}$Be partial wave supporting the initial bound state, the potential must be fixed to that generating the bound state. In that respect, there is a difference between the Faddeev/AGS calculation and the Transfer to the Continuum one. In the Faddeev/AGS calculation all partial waves but that supporting the initial bound state are assigned the KD potential, while the one supporting the bound state is assigned the binding Woods-Saxon potential. In the Transfer to the Continuum one, the final states do not have a defined $n-^{10}$Be configuration, so different potentials cannot be assigned to different configurations. As such, in the coupled-channel calculation, the $n-^{10}$Be potential is always taken from KD, and the binding potential is only used to generate the bound neutron wavefunction.

Another difference arises in the treatment of the $p+^{11}$Be potential. As

mentioned above, the Faddeev/AGS formalism does not require this potential as an input, since it only uses binary interactions between $p, n,^{10}$Be, while in TC this potential is involved in the calculation of the distorted wave for the incident channel (Eq. (2.14)). For the TC calculation, two choices for this potential are explored: the first computes this potential by folding V_{pn} and $V_{p^{10}\mathrm{Be}}$ with the bound neutron wavefunction in order to produce $V_{p^{11}\mathrm{Be}}$

$$U^{\mathrm{fold}}_{p^{11}\mathrm{Be}}(\mathbf{R}) = \int \mathrm{d}\mathbf{r}_{n^{10}\mathrm{Be}} \left|\varphi_{^{11}\mathrm{Be}}(\mathbf{r}_{n^{10}\mathrm{Be}})\right|^2 \left(V_{pn}(\mathbf{r_{pn}}) + U_{p^{10}\mathrm{Be}}(\mathbf{r_{p^{10}Be}})\right). \quad (3.3)$$

The second takes $V_{p^{11}\mathrm{Be}}$ from KD parametrization at 200 MeV. We note that, when the final state wavefunction is the exact solution of Schrödinger's equation the choice of $V_{p^{11}\mathrm{Be}}$ is arbitrary and does not modify the transition matrix. As such, if our approximation for the final wavefunction Ψ^{bin}_b is a good representation of the exact solution for the region of space explored by the reaction, we expect the choice of $V_{p^{11}\mathrm{Be}}$ not to modify much the reaction observables.

For V_{pn}, a Gaussian interaction is assumed [61].

$$V = -V_0 e^{-\frac{r^2}{a_0^2}}. \quad (3.4)$$

The Gaussian interaction is taken as attractive for the waves with even $p-n$ orbital angular momentum and as repulsive for those with odd $p-n$ orbital angular momentum. This choice was taken for simplicity and because the Reid93 potential was not implemented in the Faddeev/AGS program at the moment of this benchmark.

All distorting potentials as well as V_{pn} are presented in Table 3.2. The potentials are taken as spin-independent, which allows us to take all involved particles as spinless. Coulomb interaction is also ignored, as it is expected to influence little the reaction observables. This reduces the computational cost of the calculations, and in particular allows all partial waves for the outgoing $p-n$ system to be coupled in the Transfer to the Continuum calculation, in contrast to the previous benchmark. In the calculations, p and n are assumed to have a mass of 1 average nuclear mass 1 a.n.m. = 1.00797 amu, while ^{10}Be and ^{11}Be masses are taken as 10 and 11 a.n.m. respectively. The maximum orbital angular momentum considered for the $p-n$ pair is taken as $l_{max} = 3$,

	V_0(MeV)	W_0(MeV)	r_0(fm)	a_0(fm)	W_s(MeV)	r_{0s}(fm)	a_{0s}(fm)
$V_{p-^{10}\mathrm{Be}}$	13.445	13.095	1.116	0.676	0.204	1.308	0.524
$V_{n-^{10}\mathrm{Be}}$	15.970	10.997	1.116	0.676	0.128	1.308	0.543
$V_{p-^{11}\mathrm{Be}}$	13.740	13.100	1.122	0.676	0.217	1.307	0.524
V_{pn} l *even*	72.15			1.484			
V_{pn} l *odd*	-72.15			1.484			

Table 3.2: Parameters for the potentials used in the calculation. All potentials are taken from [76] but V_{pn}, which is based on the parametrization from [61].

since most of the cross section is expected to be contained in the considered partial waves and higher l make the calculation both significantly heavier and less stable. The maximum total angular momentum for the three-body system is taken as $J_{max} = 60$. Test calculations with $J_{max} = 70$ showed negligible differences.

In the Transfer to the Continuum calculations the binning mesh used is the following: bins are computed evenly spaced in energy with a width of $\Delta E = 5$ MeV. For $l_{pn} = 0, 1$ the mesh is extended from 0 to 160 MeV, while for $l_{pn} = 2, 3$ the mesh is taken from 20 to 160 MeV. A test calculation with $\Delta E = 2.5$ MeV shows a change in the cross section of $\sim$0.6%, so we consider the calculation with $\Delta E = 5$ MeV to be sufficiently converged.

Let us remark that in contrast to the previous calculation, the *remnant term* $V_{p^{10}\mathrm{Be}} - V_{p^{11}\mathrm{Be}}$ is kept in the calculations, since the "recoil" effect introduced by this term is also accounted for by the Faddeev/AGS formalism.

3.2.2 Results

In this section the results for the benchmark are presented. Two different cases are studied in this benchmark: in the first one, the neutron is assumed to be removed from a $2s$ state, corresponding to the component with highest population probability for the halo neutron of ^{11}Be. The second assumes a neutron extracted from a $1p$ state. Both calculations are performed assuming the same neutron separation energy $S_n = 0.5$ MeV. This allows us to explore the dependence of the agreement between both formalisms on the quantum numbers of the removed nucleon, which have a fundamental influence on the shape of the observables, in particular of the momentum distributions.

The observables we have chosen to present are the following, all referring to the outgoing ^{10}Be core: in the top left, the transversal momentum

distribution: $\frac{d\sigma}{dp_x}$, in the top right, the longitudinal momentum distribution measured in the center of mass system: $\frac{d\sigma}{dp_z}$, in the bottom left, the energy distribution measured in the center of mass: $\frac{d\sigma}{dE_{^{10}\mathrm{Be}}}$ and in the bottom right, the angular differential cross section in the center of mass: $\frac{d\sigma}{d\Omega}$. The results of the benchmark assuming a neutron in the $2s$ state are presented in Fig. 3.6.

For each calculation, two TC calculations are presented which differ in the choice of $V_{p^{11}\mathrm{Be}}$. In Fig. 3.6, the blue dashed line corresponds to the

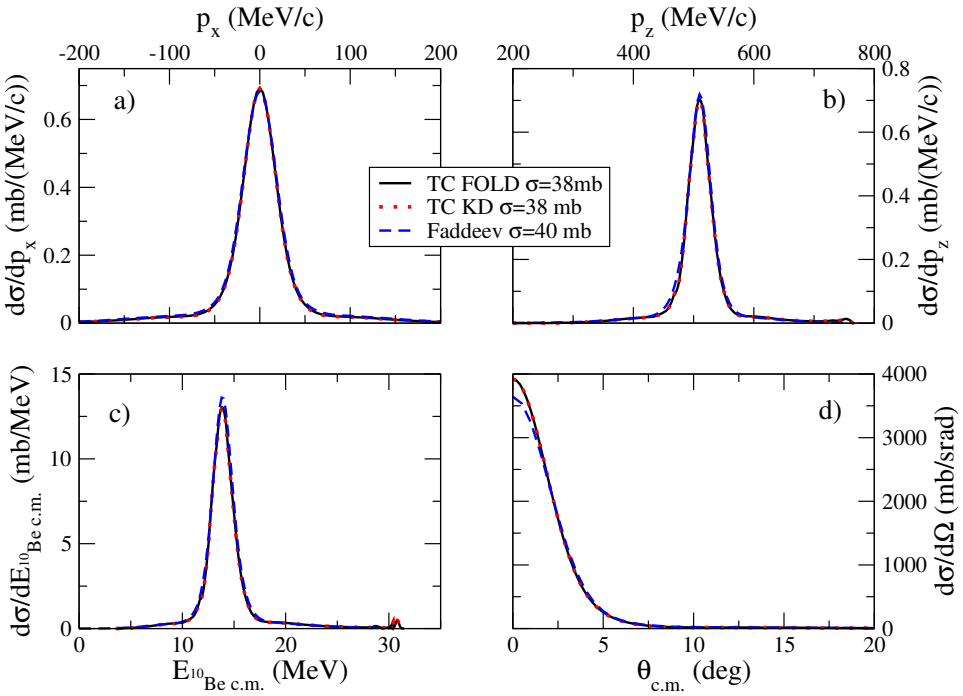

Figure 3.6: Benchmark calculation for removal of a $2s$ neutron. The blue dashed line corresponds to the FaddeeV/AGS calculation, the black solid line corresponds to a TC calculation with $V_{p^{11}\mathrm{Be}}$ obtained through folding as described in Sec. 3.2.1 and the red dotted line corresponds to TC with $V_{p^{11}\mathrm{Be}}$ from KD parametrization. The oservables presented all refer to the outgoing core ^{10}Be in the c.m. frame and are as follows: a) transversal momentum distribution, b) longitudinal momentum distribution, c) energy distribution, d) angular distribution.

Faddeev/AGS calculation while two Transfer to the Continuum calculations are presented: the black solid line corresponds to a calculation where $V_{p11\mathrm{Be}}$

is obtained from the folding procedure mentioned in Sec. 3.2.1, while the red dotted line corresponds to a calculation where $V_{p11\mathrm{Be}}$ is taken from the KD parametrization. It must be noted that the cross section leading to the deuteron, $^{11}\mathrm{Be}(p,d)^{10}\mathrm{Be}$, has been included in the Transfer to the Continuum calculations but not in the Faddeev/AGS ones. The cross section for this channel only amounts to 0.2 mb, so we find this difference not to be essential for the benchmark. In the longitudinal momentum and ^{10}Be energy distributions the deuteron contribution can be seen at the high energy and momenta and has been given an artificial width of 1 MeV in order to emulate the effects of finite experimental energy and momentum resolution and to avoid an infinite peak in the cross section.

We can see that the agreement is remarkably good for all observables except for the angular differential cross section at small scattering angles, where the Faddeev/AGS result falls under both Transfer to the Continuum calculations, which agree rather well between themselves. We note that due to the solid angle factor $\sin(\theta)$, these small angles contribute little to the cross section, which explains why this difference is not so apparent in the rest of the observables. The integrated cross section is larger for the Faddeev/AGS calculation, as can be seen in the legend of the figure. Closer inspection shows the Faddeev/AGS calculation to give a slightly bigger peak in the energy distribution and a somewhat greater contribution in the low momentum tail in the longitudinal momentum distribution. It is difficult to elucidate a physical reason for these differences, although it could be argued that the in the Transfer to the Continuum, the use of the KD potential for all partial waves may introduce a small extra source of absorption, when compared to the Faddeev/AGS calculation, which uses the real binding potential for the $l = 0$ partial wave.

With these cautionary notes, we may conclude that the agreement between both formalisms, which use slightly different inputs and may not give *a priori* compatible results, is rather satisfactory. We also note that the Transfer to the Continuum observables is remarkably similar for both choices of $V_{p^{11}\mathrm{Be}}$. This can serve as an indication that our approximation for the final three-body wavefunction is reasonable in these reactions, since formally the exact solution is independent of the choice of $V_{p^{11}\mathrm{Be}}$.

In Fig. 3.7, the same observables as in Fig. 3.6 are presented for the calculation where the neutron is removed from a $1p$ orbital. In general,

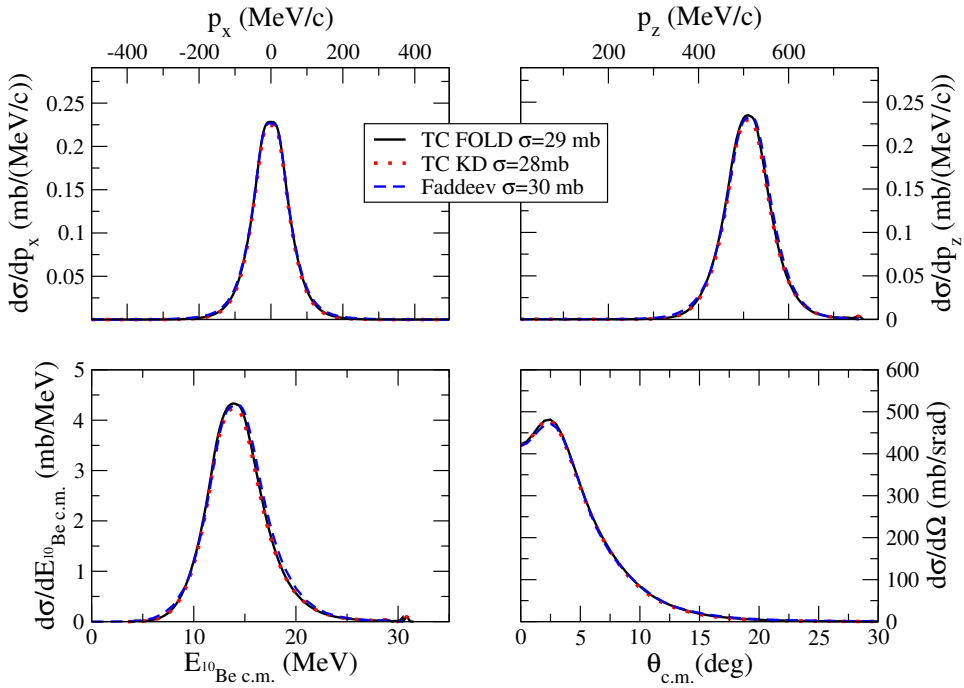

Figure 3.7: As Fig. 3.6 but for removal of a $1p$ neutron.

the same features are observed as in the case with removal from the $2s$ orbital. All calculations give a rather good agreement, with the Transfer to the Continuum calculations giving a cross section which is somewhat smaller than that of Faddeev/AGS ones. As before the deuteron contribution is included in the Transfer to the Continuum calculations but not in the Faddeev/AGS ones. In this case the contribution is even smaller, of 0.04 mb, so this difference should not be too relevant for the comparison. The difference in the angular distribution is reduced in this case, although this is likely due to the reduction of the contribution of the lower angles, which tend to be more unstable and sensitive to the intricacies of the calculation.

Although the differences are small, the Transfer to the Continuum calculations seem to differ somewhat more in this case when compared to the $2s$ one. The differences are however too small to be given physical meaning, since they may well be simply a result of the numerical calculation. Let us also remark that once the final wavefunction is not the exact solution of Schrödinger equation, the choice of $V_{p^{11}\mathrm{Be}}$ may influence the cross section, and it is difficult to relate the dependence of the observables on it with the adequacy of the approximate wavefunction, beyond a merely qualitative

discussion.

Both Transfer to the Continuum calculations seem to give slightly narrower momentum distributions than the Faddeev/AGS calculation. We must remark that, in contrast to what was found in the benchmark with DWIA presented in Sec. 3.1, this is not related to the energy dependence of the potential, which in this case is fixed at a certain energy in both Faddeev/AGS and Transfer to the Continuum calculations. Again the difference is too small to try and give physical meaning to it.

Calculations with Reid93

We note that the Gaussian interaction used up until now in the comparison with the Faddeev/AGS formalism is adjusted to describe well the binding energy and mean square radius of the deuteron and the low-energy phase shifts for the $p-n$ subsystem in the $^3S_1$ wave. However, it does not produce the well known d wave component of the deuteron, nor does it reproduce the phase shifts for the other waves of the $p-n$ subsystem.

For these reasons we find it suitable to perform some other benchmark calculations using the Reid93 nucleon-nucleon potential, in order to check whether the consistency found in the previous calculations is maintained when introducing the new NN interaction. Given that the Reid93 interaction is spin-dependent we no longer can remove the spins of proton and nucleon. Instead of performing the calculation for final states with $l = 0 - 3$ relative angular momentum between proton and neutron, we have opted to consider the states with total angular momentum between them of $J^\pi = 0 - 3^\pm$. Since the number of final states increases by a factor of 4 due to the spins of both proton and neutron, it is no longer feasible to perform the calculation coupling all final states. Following the method taken for the other calculations in this work, we uncouple states with different total angular momentum and parity j^π, computing independently the cross section leading to each set of states.

The results are presented in Fig. 3.8 assuming a neutron removed from a $s_{1/2}$ state and in Fig. 3.10 from a $p_{1/2}$ state. As can be seen from the figures both TC and Faddeev/AGS calculations keep showing very similar shapes for all the distributions presented, again the TC ones being slightly narrower than the ones from Faddeev/AGS. However, the TC distribution

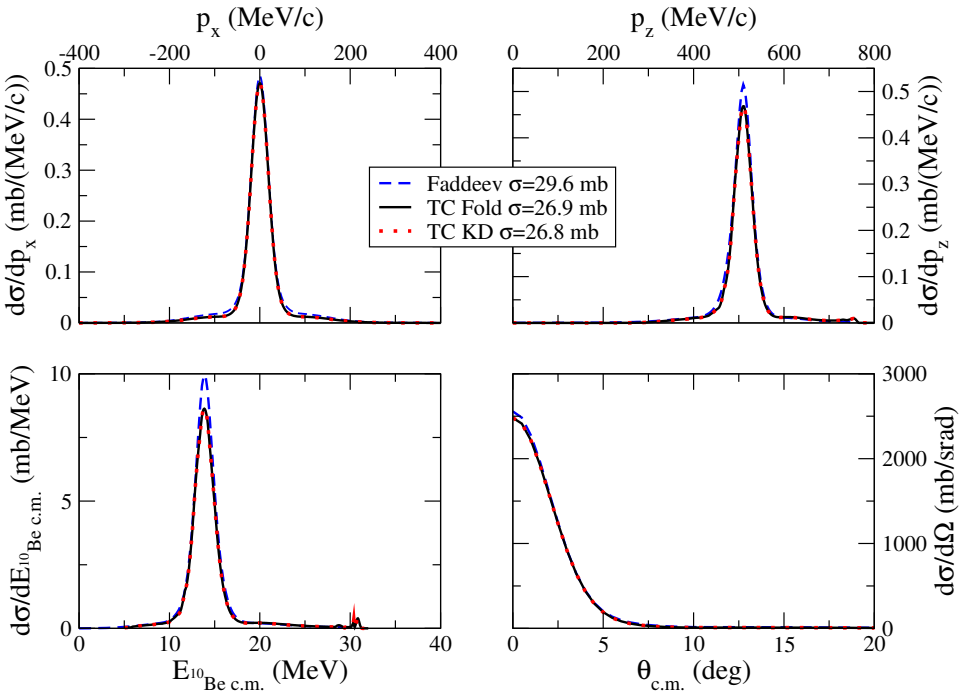

Figure 3.8: As Fig. 3.6 taking the Reid93 as NN interaction, assuming a neutron removed from the $2s_{1/2}$ wave.

is noticeably smaller than Faddeev's, with a reduction of $\sim 8\%$. Given the excellent agreement found in the study employing the Gaussian potential, this difference is quite intriguing. In order to try to clarify the origin of this difference and to check the implementation of the Reid93 interaction, we have performed a comparison of our plane-wave calculations for the case with the neutron removed from the p wave, whose results are shown in Fig. 3.10. For the plane-wave calculation we find that the agreement between Faddeev/AGS and TC is once more excellent. Since in this calculation the only relevant potential is the NN interaction, it should be most sensitive to the intricacies of the Reid93 interaction. The agreement of the plane-wave calculation thus indicates a compatible behaviour of the Reid93 interaction in the Faddeev/AGS and TC formalisms.

The origin of the difference between both formalisms in Figs. 3.8 and 3.10 is therefore not found (only) in the Reid93 interaction and has not been clarified by the time of composition of this work. One possible cause is the effect of uncoupling the final states with different j^π for the final $p-n$ subsystem, which could, in principle, affect the total cross section. The

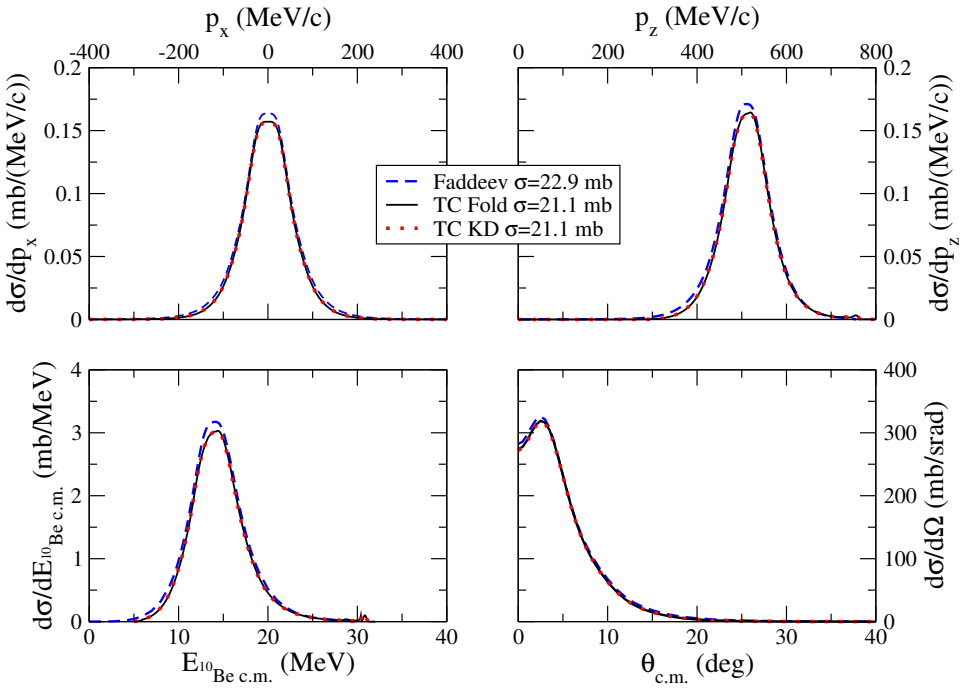

Figure 3.9: As Fig. 3.6 taking the Reid93 as NN interaction, assuming a neutron removed from the $1p_{1/2}$ wave.

effects of this approximation are difficult to test because the full calculation requires too much computer time and resources to be feasible in a reasonable time. As will be detailed in Sec. 2.5.1, a rough calculation was performed coupling the most relevant waves and the difference between this calculation and the uncoupled ones was found to be much smaller than the one found here. As such, it does not seem likely that this is the origin of the discrepancy.

Another possible origin of the difference between the calculations lies in the potential between p and ^{11}Be, as mentioned in previous sections. For the TC calculations, as in previous cases, we have explored two different prescriptions for this potential, one obtained from the KD parametrization and the other from a folding of the $n-^{10}$Be and pn interactions over the square of the wave function of ^{11}Be. On the other hand, the Faddeev/AGS formalism only considers binary interactions between p, n and ^{10}Be.

The excellent agreement between both TC calculations is remarkable and is indication of the final CDCC wavefunction $\Psi^{\rm bin}_{b\alpha}$ being a good approximation of the exact 3-body wavefunction $\Psi^{3b}_{b\alpha}$, since for the exact wavefunction the choice of $U_{p^{11}\rm Be}$ does not affect the interaction. This could be understood

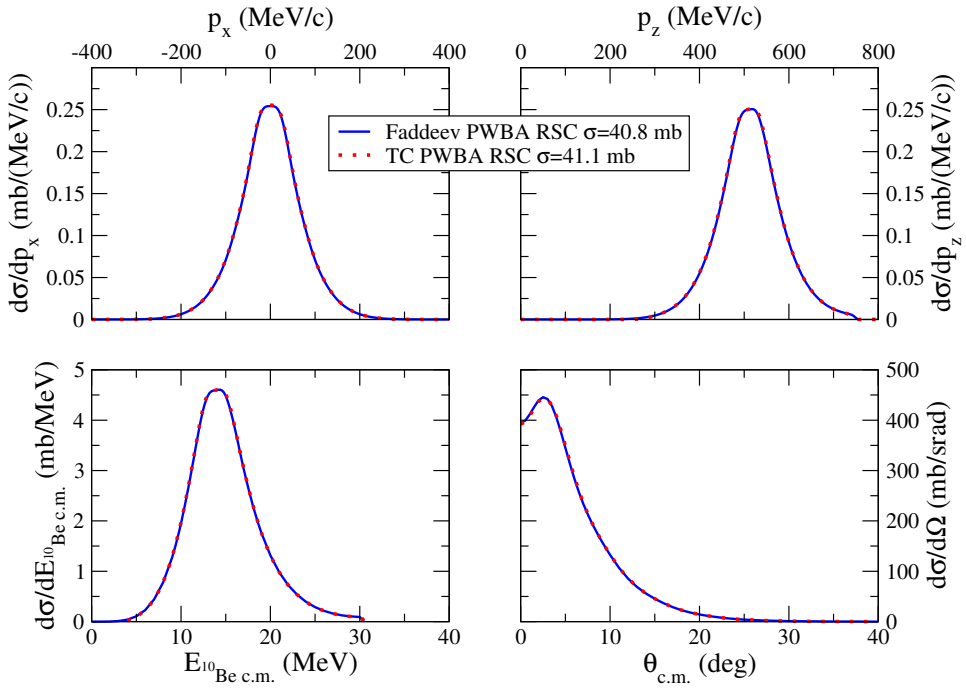

Figure 3.10: Plane wave calculation for the ^{11}Be$(p,pn)^{10}$Be reaction at 200 MeV/A, assuming the removal of the neutron from the $1p_{1/2}$ wave. Red dots correspond to the TC calculation, while the blue line corresponds to the Faddeev/AGS one.

as $U_{p^{11}\mathrm{Be}}$ having a small effect on the final cross section. However, calculations rescaling the $U_{p^{11}\mathrm{Be}}$ potential still show some dependence of the cross section, so the result is not independent on $U_{p^{11}\mathrm{Be}}$. The agreement between both prescriptions for the potential rather stems from the folding being dominated by the $p-^{10}$Be interaction, which comes from the KD parametrization and is very similar to the one for $p-^{11}$Be.

It can be questioned whether these simple descriptions of the $p-^{11}$Be interaction are able to mimic the complex behaviour of the Faddeev/AGS equations, specially when the $p-n$ interaction is as strong and peaked as the Reid93 interaction, as well as being and l-dependent. A milder potential such as the Gaussian of the previous section may result in a better description by smooth potentials such as the ones used in the TC calculations.

The results presented here seem at odds with those presented in Sec. 3.1.3. We do not have a satisfactory explanation for the disagreement in the calculations presented in this section and the agreement found there. It is

possible that the inclusion of $J = 4^{\pm}, 5^{\pm}$ in our calculations for Sec. 3.1.3 had helped increase the TC cross section, thus meeting the Faddeev/AGS one or that the discrepancies are reduced for the larger energy of 420 MeV/A considered there.

Despite these discrepancies, the excellent agreement between TC and DWIA both in shape and magnitude as well as the agreement between TC and Faddeev/AGS, good in shape and fair in magnitude, serve as validation for the TC formalism to be used in comparison to experimental data for (p, pn) and $(p, 2p)$ reactions, which will be presented in the next section.

Chapter 4

Comparison with experimental data

It doesn't matter how beautiful your theory is, it doesn't matter how smart you are. If it doesn't agree with experiment, it's wrong.

Richard P. Feynman

In this chapter, results of calculations with the Transfer to the Continuum formalism are presented and compared to published experimental data.

4.1 Experimental results for low- and medium-energy experiments

The Transfer to the Continuum (TC) formalism is not based in the Impulse Approximation nor it requires any eikonal approximation. In fact, the main approximations taken in its development is the Born approximation performed in Eq. (2.10) and the ansatz for Ψ_b given in Eq. (2.15) both of which can be related to the assumptions that the coupling to the excited states of the parent nucleus is small and that the reverse coupling, from the breakup $p + n + C$ states to the $p + A$ state is small.

Both assumptions are verified at lower energies than the energies usually required for the applicability of the eikonal and impulse approximations. As

such, we expect TC to be valid at these lower energies, under 100 MeV/A. As such, we present in the following a pair of (p, pn) reactions at low energies which we analyse using TC to show the validity of the formalism at low energies and the information that it can provide from these reactions.

4.1.1 ^{18}C$(p, pn)^{17}$C* at 81 MeV/A

The first reaction we present in this section is the (p, pn) reaction on ^{18}C leading to ^{17}C in its excited states, which was performed in the RIBF facility at an energy of 81 MeV/A and whose results were published in [79]. In that work, experimental data were compared to CDCC calculations, which are similar to TC ones but which expand the 3-body $p + n + ^{17}$C final state in states with good angular momentum and parity of the $n + ^{17}$C subsystem instead of the $p + n$ subsystem, as in TC. As such, CDCC calculations cannot include the (p, d) channel.

We now present a reanalysis of the experimental data for this reaction using the TC formalism. The inputs of the reaction have been taken following closely the prescriptions for the CDCC calculations in [79]: the optical potentials between $p, n - ^{18,17}$C have been taken through a folding procedure between the JLM effective interaction [80] (valid for nuclei with 12<A<208 at energies E<160 MeV) and the density of ^{18}C or ^{17}C, obtained using the subroutine DENS, which is part of the OXBASH package [18]. The bound state for the neutron is obtained as the eigenvalue for a Woods-Saxon potential with $r_0 = 1.25$ fm and $a = 0.7$ fm, whose depth has been adjusted to reproduce the effective neutron separation energy ($S_n^* = S_n + E_x$) where $S_n = 4.18$ MeV is the neutron separation energy of the ground state of ^{18}C leading to the ground state of ^{17}C while E_x is the excitation energy of the excited state of ^{17}C*. Spectroscopic factors have been obtained from a shell-model calculation with the WBP interaction [15].

For the $p-n$ interaction, in [79] they have used the semirealistic Malfliet-Tjon V potential [81], which was adjusted to reproduce only the $^1S_0$ and $^3S_1$ $p-n$ phase shifts. Since in TC the $p-n$ interaction is the main one leading the reaction, we have chosen instead to use the Reid93 [74] interaction, which reproduces all phase shifts for the $p-n$ states of interest here.

In this reaction, two excited states of ^{17}C are populated, one at E_x=0.21 MeV and another at E_x=0.33 MeV. The ground state is also populated, but

due to its small overlap with the ground state of ^{18}C, the cross section to it is small and could not be established accurately. As such, we have chosen not to compute the cross section to the ground state, since the experimental data to compare with are not well established.

As indicated in Sec. 2.5.1, the cross section to states with a certain $p-n$ angular momentum and parity j^π is computed independently. In this case we have only computed states with j up to 3. As is shown in Fig. 4.1, the cross section is strongly dominated by the 1^+ contribution, and it decreases with increasing j. therefore, the states with $j > 3$ will not contribute much to the cross section. This can be easily understood as the phase shift for the free $p-n$ process at low energy is much larger for the $^3S_1$ wave than for all of the other waves.

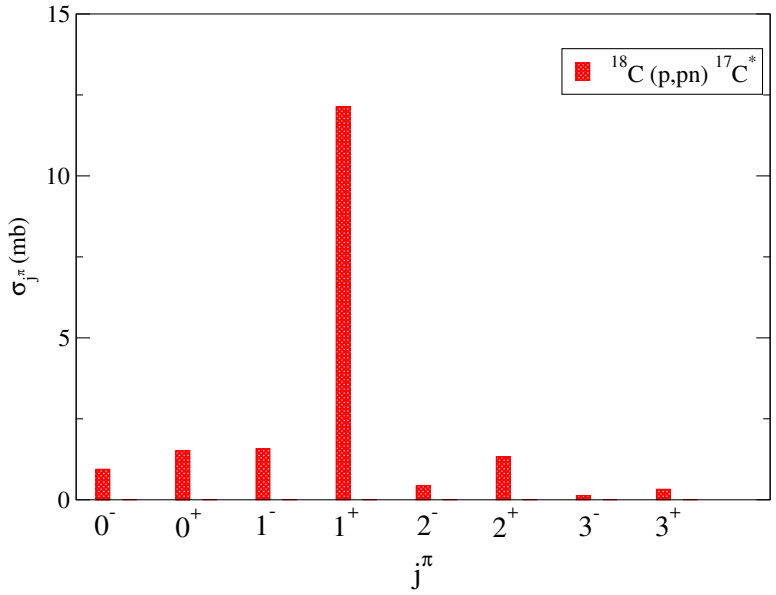

Figure 4.1: Cross section for the $^{18}\mathrm{C}(p,pn)^{17}\mathrm{C}^*$ (0.33 MeV) reaction assuming removal from the $d_{5/2}$ state as a function of the final $p-n$ angular momentum and parity j^π.

Cross sections are computed using the formula:

$$\sigma_{th} = \sum_\alpha C^2 S_\alpha \left(\frac{A}{A-1}\right)^N \sigma_{sp}^\alpha, \tag{4.1}$$

where α denotes the states of the core which contribute to the reaction, σ_{sp}^α is the corresponding single-particle cross section, C^2S_α is the spectroscopic

E_x (MeV)	J^π	σ_{exp}	C^2S	σ_{sp}^{CDCC}	σ_{th}^{CDCC}	R_s^{CDCC}	σ_{sp}^{TC}	σ_{th}^{TC}	R_s^{TC}
0.21	$1/2^+$	11(2)	0.65	28	21	0.52(10)	21.8	15.9	0.69(13)
0.33	$5/2^+$	43(5)	2.80	18	57	0.75(9)	17.4	54.6	0.79(9)

Table 4.1: Cross section and "quenching factors" R_s for ^{18}C$(p,pn)^{17}$C* obtained from CDCC [79] and TC calculations. The first and second columns indicate the energy and the angular momentum and parity of the state, respectively, while the third column shows the experimental cross section. The fourth column shows the spectroscopic factor obtained with the WBP interaction for each state. The fifth, sixth and seventh columns show the CDCC single particle cross section, theoretical cross section and "quenching factor", respectively. The eight, ninth and tenth columns do the same for TC values.

factor with the necessary isospin factor, A denotes as usual the mass number of the parent nucleus and N is the shell main quantum number for the orbital from which the nucleon is removed. We must note here that the $\left(\frac{A}{A-1}\right)^N$ factor has been strictly derived for the Independent Particle Model in a harmonic oscillator basis [82] and its use can be questionable in the present case, where we use shell-model SF. Noting this caveat, we include this factor nonetheless, following previous authors [32] with whose results we intend to compare. We have computed the cross section for the $1/2^+$ state at E_x =0.21 MeV assuming removal from the $2s_{1/2}$ level and for the $5/2^+$ state at E_x =0.33 MeV assuming removal from the $1d_{5/2}$ level. The results for the total cross section, as well as for the "quenching factors" $R_s = \sigma_{exp}/\sigma_{th}$ are presented in Table 4.1. Results from the CDCC calculation in [79] are presented as well for comparison. Transversal momentum distributions are presented in Fig. 4.2.

As can be seen in Fig. 4.2, the agreement in shape between the TC calculation and experimental data, after convolution with the experimental resolution (FWHM=71 MeV), is very good for both excited states of ^{17}C: $1/2^+$ in the left panel and $5/2^+$ in the right one. In the table we can see that the "quenching factors" R_s obtained in the TC calculation are larger than those obtained with the CDCC calculation. They are also more consistent between themselves, both agreeing within error (which was computed propagating the error from the experimental cross section) while this is not the case for the CDCC calculation.

However, a very interesting feature appearing in our calculation is the

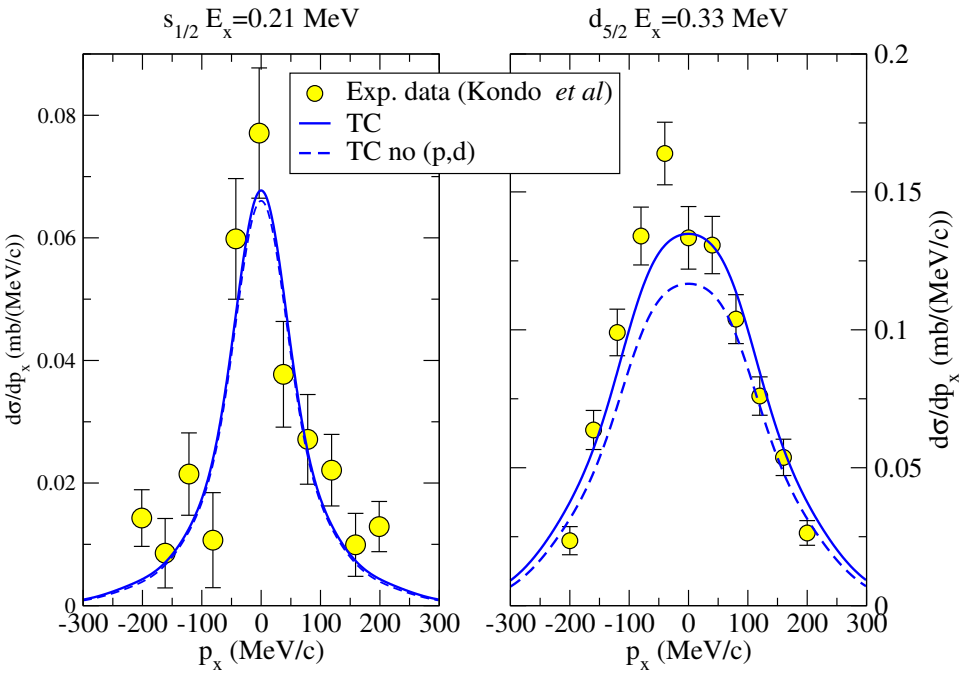

Figure 4.2: Transversal p_x momentum distributions for the $^{18}\mathrm{C}(p,pn)^{17}\mathrm{C}^*$ reaction. Experimental data are from [79]. The left panel corresponds to (p,pn) leading to the $E_x = 0.21$ MeV ^{17}C excited state, while the right panel corresponds to the $E_x = 0.33$ MeV excited state. The blue solid line corresponds to the full calculation rescaled to give the experimental total cross section. The blue dashed line corresponds to the calculation removing the contribution from the (p,d) transfer reaction, rescaled by the same factor as the full calculation. All theoretical calculations have been convoluted with the experimental resolution.

contribution of the (p,d) reaction channel. We must note that experimentally, only the ^{17}C core was detected, so the contribution of the (p,d) channel, if significant would be incorporated to the experimental observables. For the $1/2^+$ single-particle cross section, (p,d) contributes with 0.83 mb, which amounts only to 3% of the cross section, being rather small. However, for the $5/2^+$ its contribution rises to 2.61 mb, 15% of the single particle cross section.

In order to check whether this strong contribution of the (p,d) channel is an artifact of the calculation we have performed simple DWBA calculations for the $^{18}\mathrm{C}(p,pn)^{17}\mathrm{C}^*(E_x = 0.33)$MeV reaction. A calculation using An-Cai [83] potential between d and ^{17}C, which is valid for this range of masses and

energy, and the same JLM prescription of the TC calculation for the $p-^{18}$C potential yields a transfer cross section of 2.18 mb, while a calculation using An-Cai for $d-^{17}$C and Köning-Delaroche for $p-^{18}$C yields 2.48 mb. The variation of the values with the potential is expected and known for transfer calculations [40]. However, overall value of the cross section is coherent and consistent with that found in TC.

From this, we conclude that the contribution of (p, d) transfer reaction to the total cross section is indeed important at these energies. Therefore, we must discourage the use of formalisms which do not include this channel, such as CDCC, for reactions such as this, in which this channel contributes strongly, in favour of those which include it, such as TC.

4.1.2 ^{20}C$(p, pn)^{19}$C at 40 MeV/A

In this section, we analyze the reaction $^{20}\mathrm{C}(p, pn)^{19}\mathrm{C}$ using the Transfer to the Continuum formalism. This reaction was measured at the RI Beam Factory (Japan) and the experimental data published in [84]. This reaction is of particular interest because it populates the bound states of ^{19}C, whose low-energy spectrum is still under debate. As can be seen in Fig. 4.3, experimental evidence is conflicting on the existence of a bound $5/2^+$ state, with results from [85, 86] favouring a bound $5/2^+$ state while measurements from [87–89] suggest the state is rather an unbound resonance. Also, a reanalysis of the data from [85] presented in [90] shows them to be compatible with the $5/2^+$ state being unbound. The $^{20}\mathrm{C}(p, pn)^{19}\mathrm{C}$ reaction can be used to shed some light on the existence of a $5/2^+$ bound state, since if it does exist, it should be populated in the reaction, and rather strongly, as will be shown below. In a similar way to the analysis in [84], we base our calculations in the level scheme resulting from a shell-model calculation using the effective nucleon-nucleon WBP interaction [15], taking from it the spectroscopic factors and excitation energies of the corresponding levels. The latter are used to compute the effective separation energy $S_n^* = S_n + E_x$ with $S_n = 2.9$ MeV. The bound states for the different states are computed using Woods-Saxon potentials with a depth adjusted to give the effective separation energy and a reduced radius adjusted to give the mean square radius of a Hartree-Fock calculation using the SkX interaction [93]. In this calculation the $1d_{3/2}$ configuration was found to be unbound, so for it the value of the reduced radius from the $1d_{5/2}$

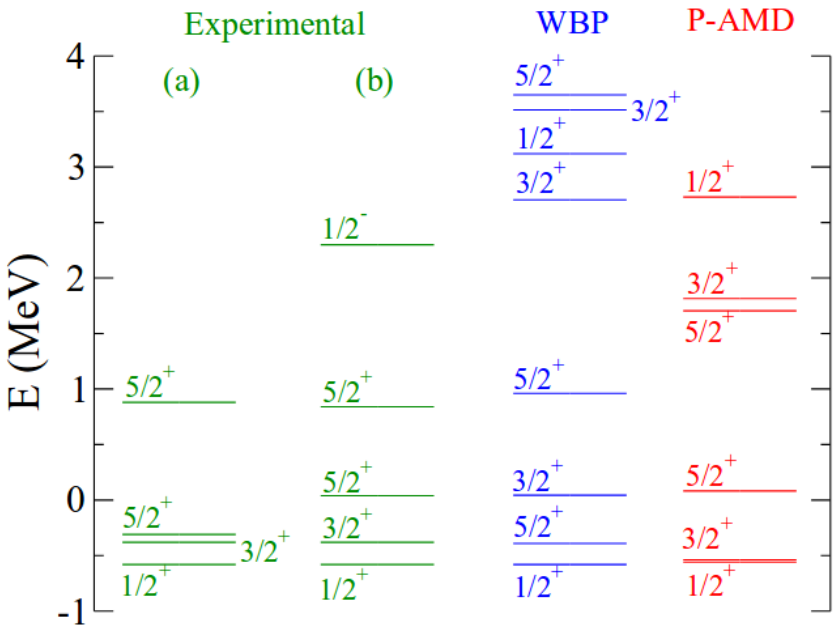

Figure 4.3: Experimental and theoretical levels for ^{19}C. The level scheme from a) has been constructed from the results in [85, 86] while that in b) is based on the results from [87, 89, 91]. The theoretical results have been obtained from a shell model calculation using the WBP interaction [15] and from a P-AMD model [92]. Note that the first $5/2^+$ state is either bound or unbound for different experiments and models. Figure taken from [90].

calculation has been considered. Details on the calculation are presented in Table 4.2.

The optical potentials between p, n and ^{19,20}C have been computed as in the previous section, through a folding procedure between the JLM effective interaction [80] and Hartree-Fock densities. Due to the low beam energy, the coupling between $p-n$ states with different angular momentum and parity becomes relevant. From the results of the previous section, which show that states with $J^\pi \geq 3$ do not contribute much to the cross section, we have restricted the calculations to states with $J^\pi < 3$, which are all coupled. The results of the calculations are shown in Fig. 4.4. The single-particle cross sections are shown in the dot-dashed lines, blue, red and green for the states $1/2^+$, $3/2^+$ and $5/2^+$, respectively. The orange solid line corresponds to the sum of the contributions for the $1/2^+$ and $3/2^+$ states, following Eq. 4.1, while the dark green solid line corresponds to the sum of the contributions

to the three considered states.

As can be seen in Fig. 4.4, both results overestimate experimental data, though it is evident that the inclusion of the $5/2^+$ increases greatly the cross section separating it much more from experimental data. In the right panel, the calculations excluding and including the $5/2^+$ state have been rescaled to give the experimental cross section. The rescaling factor for the calculation excluding the $5/2^+$ state is rescaled by a factor 0.59(22) while the one including it is rescaled by a factor 0.20(7), which we consider to be too small to be credible. It is notable that despite the different shape shown by both calculations, after rescaling both reproduce relatively well experimental data, due to the large error bars for these data.

We take these results as support for the models where the $5/2^+$ is unbound, since its inclusion worsens the agreement with experimental data, leading to a too small rescaling factor. The method employed here, which takes the spectroscopic factors from a shell model calculation, but allows for a change in the energies of the corresponding states may be put into question. However, we note that in shell model calculations spectroscopic factors tend to be more stable than the energies of the levels, which are more sensitive to the interactions and model spaces used in the calculation. We have repeated the nuclear structure calculation using the WBT [15] interaction. This has switched the positions of the $1/2^+$ and $5/2^+$ states, leading to a $5/2^+$ ground state for ^{19}C. However, the spectroscopic factors have shown changes of less than 15%, being 1.053, 3.946 and 0.202 for $1/2^+$, $5/2^+$ and $3/2^+$ states respectively, which is in agreement with the previous interpretation.

J^π	E_x (MeV)	C^2S	r_0 (fm)	$\sigma_{\rm sp}$ (mb)
$1/2^+$	0.00	1.099	0.905	27
$5/2^+$	0.19	3.649	1.145	19
$5/2^+$	0.62	0.247	1.145	18

Table 4.2: Results for the considered levels of ^{19}C. The first, second and third column denote the angular momentum and parity, excitation energy and spectroscopic factors for the states obtained using the WBP interaction respectively. The fourth column indicates the reduced radius used for the computation of the bound state wavefunction. The last column shows the single particle cross section to each state.

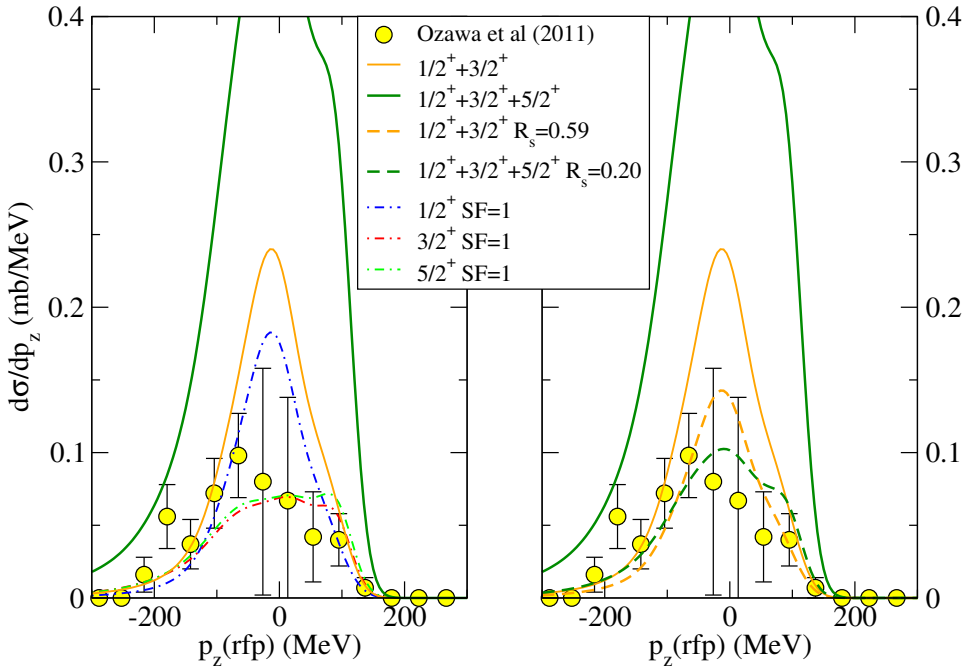

Figure 4.4: Experimental data and Transfer to the Continuum calculations for the ^{20}C$(p,pn)^{19}$C reaction. The left panel shows the single-particle cross sections for the states $1/2^+$, $3/2^+$ and $5/2^+$ in the blue, red and green dash-dotted lines, respectively, while the orange and dark green solid lines denote the total contribution for states $1/2^+$ and $3/2^+$ and $1/2^+$, $3/2^+$ and $5/2^+$ respectively. In the right panel the orange and dark green lines have been rescaled to reproduce the experimental cross section, with the result shown in the dashed lines and the rescaling factor appearing in the legend

4.2 Comparison with R^{3}B data

As mentioned in Chapter 1, the R^3B collaboration has very recently performed a campaign of (p,pn) and $(p,2p)$ reactions at energies of 300-500 MeV, whose fist results have only very recently been published [23, 42, 43]. The results published correspond to carbon, nitrogen and oxygen isotopes and their analysis with the Transfer to the Continuum formalism is presented in the following, with special interest in the dependence of the found "quenching factors" on the isospin asymmetry of the nuclei.

4.2.1 Choice of optical potentials

Fundamental ingredients in the calculations presented in this document are the optical potentials used to describe the distortion and absorption suffered by the incoming proton and the outgoing nucleons due to their interaction with the rest of the nucleus. In general we have chosen two parametrizations to produce the optical potentials, one that can be considered more "microscopic" and one more "phenomenological".

1. Paris-Hamburg (PH)

   The first interaction we consider is the "microscopic" one. It is built through the folding of an effective nucleon-nucleon interaction with the nuclear densities of the involved nuclei. For the effective nucleon-nucleon interaction we have chosen the Paris-Hamburg g-matrix effective interaction [94, 95], which includes nuclear medium effects (in particular, Pauli blocking) and has shown to give a good description of proton-nucleus elastic scattering for energies from 100 to 400 MeV, on various nuclei such as ^{12}C and ^{208}Pb. The nuclear densities are obtained from Hartree-Fock calculations based on the SkX Skyrme interaction [93], using the subroutine DENS as before. The folding is performed with the code LEA [96]. From now on this potential will be referred to as PH potential.

2. Dirac

   The other "phenomenological" potential has already been briefly introduced in Sec. 3.1[45, 46]. It is based on the application of the Dirac equation to describe the dynamics of the proton and has been fitted to a vast number of experimental data on elastic proton-nucleus scattering ranging from ^{12}C to ^{208}Pb and for energies from 20 to 1040 MeV. From the multiple parametrizations presented, we have chosen the EDAD2 one (Energy-Dependent A-Dependent), which provides potentials for nuclei beyond those used for the fitting and is energy-dependent, thus giving a better fit to experimental data. Even though the potentials are originally produced for the Dirac equation, they can be modified to be suitable for the Schrödinger equation we use in our calculations. From now on, we will refer to this potentials as Dirac potentials.

It must be remarked that in order to give meaningful results, the production of the potentials must be consistent with the equation to be solved. In particular, the relativistic prescription used in this work (the substitution of the reduced mass μ by the reduced energy ϵ and the momentum by its relativistic value, see Sec. 2.3) has to be consistent with the codes used to generate the potential. The code LEA indeed generates potentials assuming this prescription and the program we have used to generate our Dirac potentials has an option to consider this prescription as well.

As in Sec. 3.1, a choice must be made for the outgoing proton-core and neutron-core potentials. In our formalism, the energy between outgoing nucleon and core is not well defined for the final states considered, so it is difficult to assign an energy at which to evaluate the potentials. Using the same criteria as in Sec. 3.1 we have evaluated the potentials for the outgoing channels at half the incident energy, since the maximum of the cross section is expected at this nucleon-nucleus energy. Based on the results presented in Fig. 3.4, we expect the effects of the energy dependence of the potential (which we do not include) to be relatively minor, although we note that we have only tested them in one case, at high energies and corresponding to removal from an s wave, so the extension of these results to other cases can be put into question and would deserve further study.

As a summary, in Eq. (2.37), the potentials used to generate $U_{\beta\beta'}$ [Eq. (2.36)] are evaluated at half the incident energy, while the potential U_{pA} is evaluated at the incident energy. For the potential U_{pC} in the third term of Eq. (2.37) (the reaction vertex), we have chosen to evaluate it at the incident energy, since it is to be applied on X_A, the wavefunction in the incoming channel. This choice also allows to minimize the so-called *remnant term*, $U_{pC} - U_{pA}$.

In Fig. 4.5 both PH and Dirac potentials are presented between proton and ^{16}O at three different energies: 400, 200 and 100 MeV. As can be seen in the figure, at higher energies potentials become highly absorptive. This results in the global (p, pN) corresponding to only a few percent of the full reaction cross section. It also implies that (p, pN) are not very sensitive to the nuclear interior, although it can be argued that they are not as peripheral as transfer or knockout reactions with heavier targets [52]. They also become repulsive at small distances. However, due to the strong absorption, the features of the real potential in the nuclear interior are not reflected much in

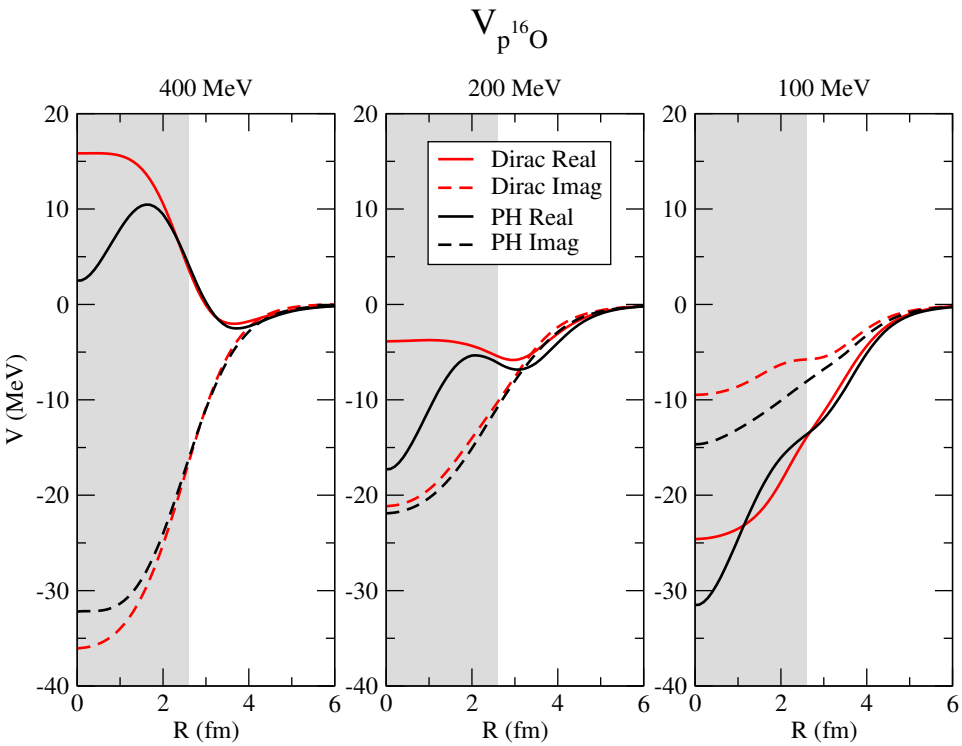

Figure 4.5: Proton-^{16}O potentials at three different energies using PH and Dirac parametrizations (See text). The shaded area marks the distances up to the rms radius of ^{16}O.

the reaction observables. The behaviour at small distances is rather different for both potentials, even though they have been adjusted to reproduce similar experimental data. This can be understood easily due once again to the insensitivity of the observables (in this case, elastic differential cross sections) to the nuclear interior, where the value of the potential is not relevant for the reaction.

In order to test the potential sets and our implementation of them, in Fig. 4.6 the elastic differential angular cross section is computed with both potentials and compared to experimental data at energies of 200, 300 and 398 MeV [97–99]. Both calculations agree well with experimental data at small angles, but for larger angles Dirac potentials agree systematically better. This should come as no surprise, since the Dirac parametrization was obtained through fitting of very similar data, the experimental data at 200 and 398 MeV actually being used for the fitting procedure. The agreement with experimental data serves as a validation for the use of these potentials

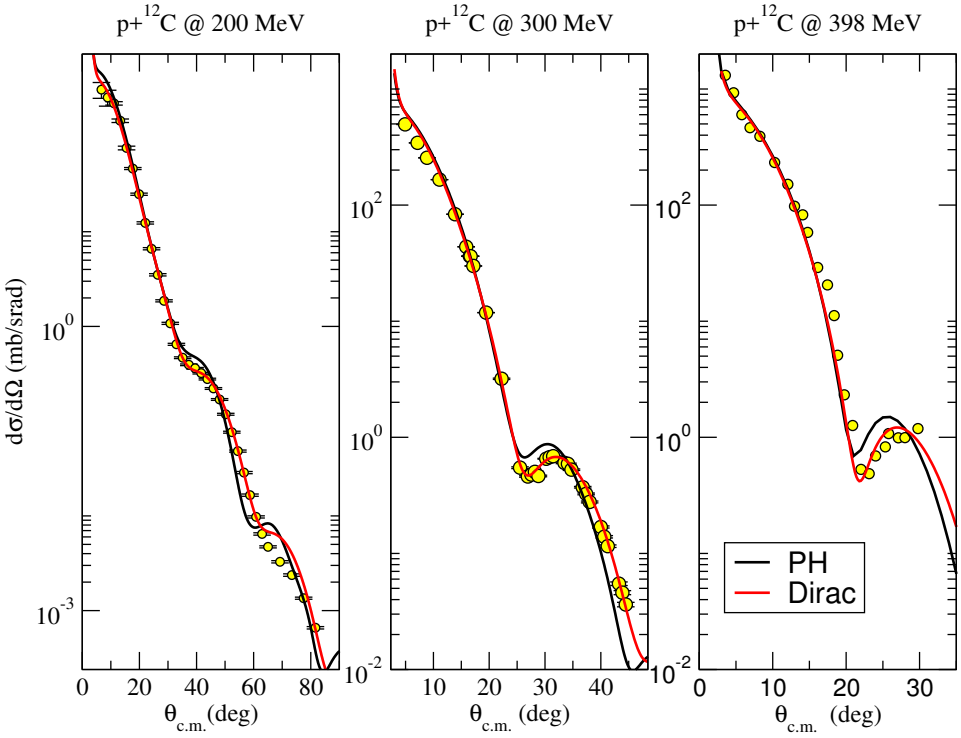

Figure 4.6: Angular differential cross sections for the elastic scattering between p and ^{12}C at 200, 300 and 398 MeV incident proton energy compared to theoretical calculations using PH and Dirac potentials. Experimental data are from [97–99] for the energies of 200, 300 and 398 MeV respectively.

as descriptors of the interaction between nucleon and nucleus in (p, pN), noting that elastic scattering is less sensitive to the nuclear interior than (p, pN) reactions, so that a part of the potentials that may be relevant for the latter is not being probed by this test.

4.2.2 Spectroscopic factors and binding potentials

Before the comparison to experimental data of (p, pn) and $(p, 2p)$ reactions at high energies, the parameters chosen to generate the spectroscopic factors and the binding potentials which bind the to-be-removed nucleon to the core must be described.

Spectroscopic factors and core excited states

The observables we will present in the following section are inclusive in the states of the residual core, requiring just the detection of the core. Excited states of the core under the particle emission threshold will deexcite by emitting a γ photon leading to the core in the ground state, so they will be counted in the experimental observables. On the other hand, excited states over the particle emission threshold will decay by the emission of a proton or a neutron, thus "breaking" the core, so they are excluded from the experimental observables. Therefore, we need to determine which states are below the particle emission threshold and which are not. Given that some of the reactions studied involve exotic nuclei for which the excited states are not established experimentally, we require a theoretical framework to predict the level scheme.

We have chosen to generate the energy levels using a shell model calculation based on the WBT interaction [15]. We are interested in a systematic study of the (p, pn) and $(p, 2p)$ cross sections. Therefore, a consistent description of all nuclei using the same inputs is essential for our conclusions and, as such, the use of a general interaction such as WBT is the best choice.

The shell model calculations were performed using the code OXBASH, which provides both the energy levels and the associated SF between the parent nucleus and the residual core. The calculation can be performed including n particle-n hole excitations. We have chosen to keep n as the minimum value required to produce non-zero SF between the parent nucleus and the residual "core", since the WBT interaction was designed for pure np-nh configurations, without mixing different n [15].

Further discussions on spectroscopic factors are presented in Appendix A.

Binding potentials

The overlap between parent nucleus and residual core is an essential part of the reaction calculation. Its obtention from the wavefunctions of both nuclei is, however, a very difficult to solve many-body problem. As such, some approximation must be taken to produce the overlap.

Following previous works [32], we produce the overlaps as the eigenstates for a Woods-Saxon potential with a diffuseness $a = 0.7$ fm and a spin-orbit term with a depth of 6 MeV and the same geometry as the central term.

The radius of the Woods-Saxon potential is adjusted to reproduce the root-mean-square (rms) radius of the corresponding partial wave obtained from a Hartree-Fock calculation (using code OXBASH), noting that the rms radius from the Hartree-Fock calculation must be multiplied by a factor $\sqrt{A/(A-1)}$ before comparing it with the result of the Woods-Saxon potential. This factor accounts for the displacement of the center of mass of the A system with respect to the $A-1$ one.

The depth of the potential is then adjusted to reproduce the effective nucleon separation energy, $S_{p,n} = S_{p,n} + E_x$.

4.2.3 Momentum distributions

In this section, momentum distributions are computed and compared to experimental results. As has been shown in Sec. 2.5.2, momentum distributions are sensitive not only to the features of the wavefunction of the removed nucleon but also to distorsion and absorption effects. As such, they are an excellent test for our formalism prior to studying the behaviour of the "quenching factors" R_s. In the following, we present comparisons to momentum distributions from different publications by the R^{3}B collaboration, focusing on the agreement in the shapes, since the agreement in magnitude will be taken into account in the next section.

- ^{12}C$(p,2p)$ at 398 MeV/A

  In this section we compare our TC calculations to the momentum distributions for ^{12}C$(p,2p)$ presented in [42]. The results are shown in Fig. 4.7.

  In the figure calculations using Dirac and PH are presented. The single-particle momentum distribution is computed for the $p_{1/2}$ and $p_{3/2}$ waves and then scaled by the corresponding spectroscopic factors (0.627 and 3.654 respectively, more detailed information is provided in the next section). Then, both distributions are added and multiplied by the "quencing factor" R_s (0.69 for PH and 0.73 for Dirac) to reproduce the experimental cross section. Note that the momentum distribution is presented for 5 MeV bins, as such, the theoretical distribution must be further multiplied by 5 in order to reproduce experimental data.

  The momenta for which the distribution is presented are somewhat

unusual. The top panel corresponds to the transversal momentum distribution $p_t = \sqrt{p_x^2 + p_y^2}$ while the bottom one shows the modulus of the momentum of the core measured in the projectile reference frame (rfp) $P_{\rm tot}$.

We note that when comparing to these experimental data, experimental resolution must be properly taken into account. The transversal momentum (p_t) and longitudinal momentum (p_z) present different experimental resolution (a Gaussian distribution with σ=20 and 50 MeV, respectively). For $P_{\rm tot}$ the resolution cannot be expressed as a Gaussian with constant width, which instead becomes momentum-dependent. In order to compute the distribution on $P_{\rm tot}$ with experimental resolution, we have computed the double differential cross section $\frac{d\sigma}{dp_t dp_z}$, we have convoluted it with the experimental resolution for p_t and p_z and from the convoluted double differential cross section we have extracted the distribution on $P_{\rm tot}$. In order to check the influence of the experimental resolution we show the momentum distributions without considering it in the black dot-dashed and red dotted lines for PH and Dirac respectively. As can be seen the experimental resolution does not modify much the p_t distribution, broadening it somewhat. On the other hand, the distribution on $P_{\rm tot}$ shows a significant modification, both broadening and shifting its peak to larger momenta.

Both PH and Dirac calculations give very similar shapes of the momentum distributions, even though they lead to cross sections which are somewhat different (See Table 4.4). When comparing both calculations to experimental data, we find that they compare relatively well to experiment, giving well the position of the peak, though they are somewhat narrower, specially for $P_{\rm tot}$, underestimating the high-momentum tail.

It can be pondered whether different weights for the $p_{3/2}$ and $p_{1/2}$ waves would change the shape of the distribution, thus endowing momentum distributions with stronger spectroscopic discernibility. Unfortunately, as can be seen in Fig 4.8, the shape of the momentum distributions for both orbitals is rather similar. Given the similarity of the shapes for both orbitals the relative occupancy of each cannot be established from the shape of the momentum distribution, be it transversal, longitudinal

or total momentum.

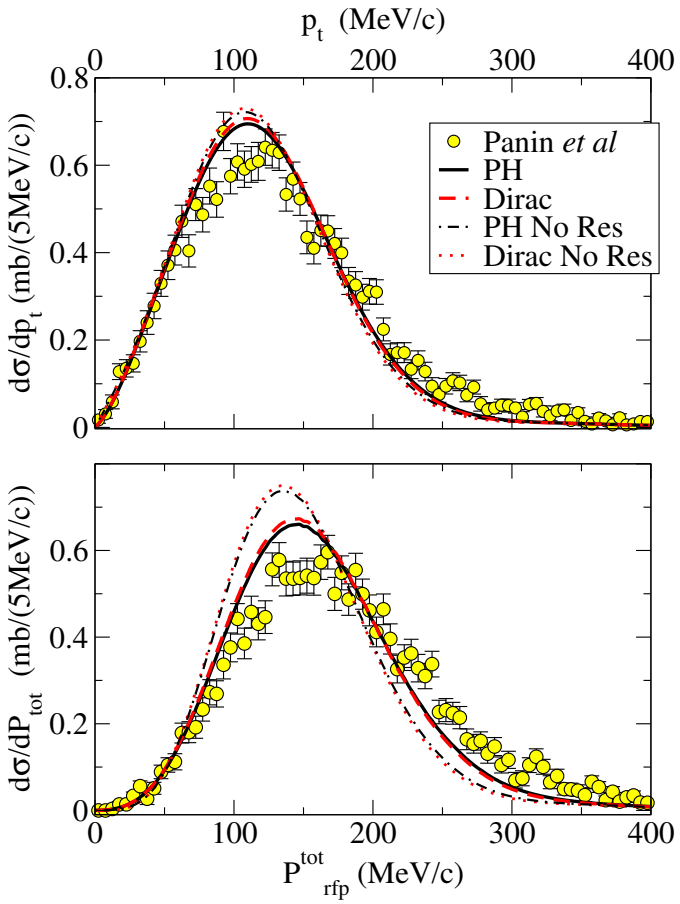

Figure 4.7: Momentum distributions for ^{12}C$(p, 2p)$ at 398 MeV/A. Experimental data are from [42]. Calculations are presented using PH and Dirac calculations (black and red lines respectively). The black solid and red dashed lines have been convoluted with an experimental resolution of 20 MeV for the transversal momentum p_x and 50 MeV for the longitudinal one p_z. Black dot-dashed and red dotted lines correspond to calculations without the experimental resolution.

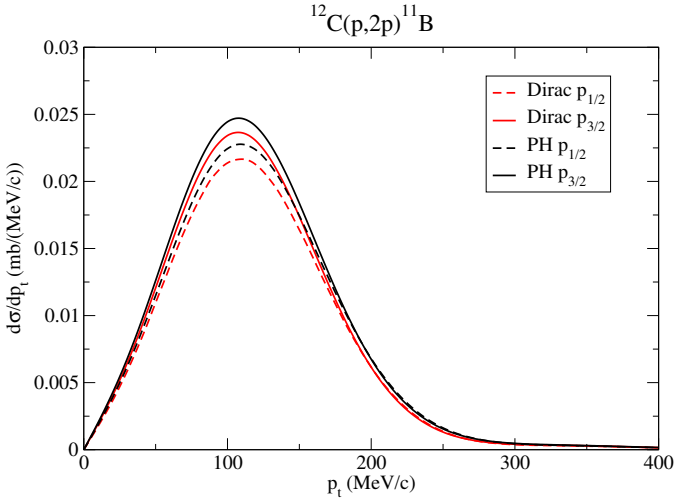

Figure 4.8: Single-particle transversal (p_t) momentum distributions for ^{12}C$(p, 2p)$ at 398 MeV/A computed for the $p_{3/2}$ and $p_{1/2}$ orbitals using Dirac and PH potentials. It can be seen that shapes are quite similar in all cases.

- ^{16}O$(p, 2p)$ @ 451 MeV/A

  In Fig. 4.9, the transversal momentum distribution (p_x) is presented for ^{16}O$(p, 2p)^{15}$N at an incident energy of 451 MeV/A, for which experimental data are taken from [23].

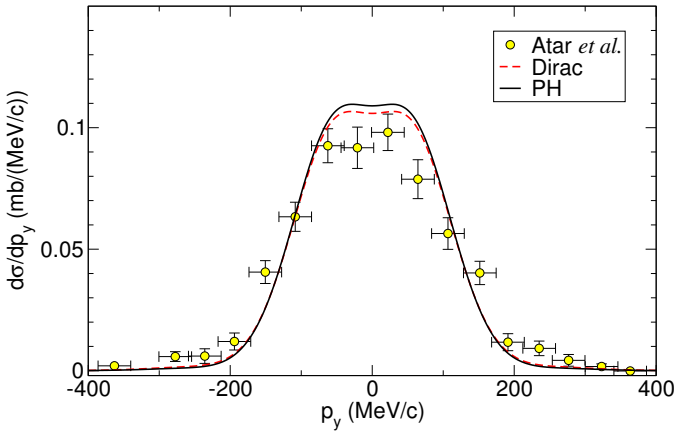

Figure 4.9: Transversal p_y momentum distribution for ^{16}O$(p, 2p)$. Experimental data are from [23]. Calculations are presented using PH and Dirac calculations (black solid and red dashed lines respectively) rescaled to reproduce the experimental cross section.

  The same procedure as for ^{12}C$(p, 2p)$ has been followed to generate the theoretical cross sections. The waves $p_{1/2}$ and $p_{3/2}$ have been considered for the removed proton, with SF 2.00 and 4.09 respectively. The Dirac and PH calculations have been multiplied by the "quenching factor" R_s 0.74 and 0.78 respectively.

  A similar result is found as for ^{12}C$(p, 2p)$. Both PH and Dirac calculations present similar shapes, both of which agree reasonably well with the experimental data, though they are somewhat narrower than experiment. In this case, it is the PH calculation the one that is slightly narrower than the Dirac one, as opposed to the previous case. As in ^{12}C, the shape of the single-particle momentum distributions is very similar for removal from $p_{1/2}$ and $p_{3/2}$ orbitals.

- ^{22}O(p, pn) @ 414 MeV/A

  In this section the transversal p_y momentum distribution for ^{22}O(p, pn) is presented together with the experimental data from [43] in Fig. 4.10. Theoretical calculations have been obtained through the same proce-

dure as the previous cases, though since in this case experimental data are given in arbitrary units results have been rescaled to reproduce the integral of experimental data, instead of by the R_s factor.

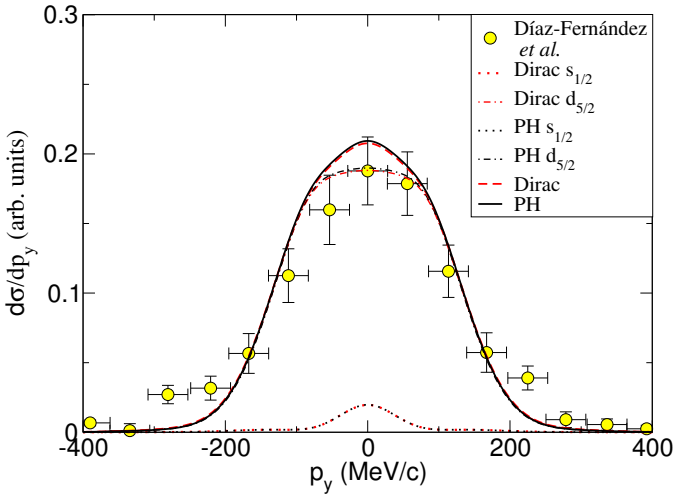

Figure 4.10: Transversal p_y momentum distribution for ^{22}O(p,pn). Experimental data are from [43]. Calculations are presented using PH and Dirac calculations (black solid and red dashed lines respectively) rescaled to reproduce the integral of experimental data (given in arbitrary units). The dotted and dot-dashed lines correspond to the contributions of $s_{1/2}$ and $d_{5/2}$ orbitals, having all been scaled by the same arbitrary factor, and as such conserving their relative weight.

For this reaction two orbitals with different orbital angular momentum intervene, $s_{1/2}$ and $d_{5/2}$. Both waves show momentum distributions with markedly different shapes, as can be seen in Fig. 4.10, where the dotted lines correspond to $s_{1/2}$ and the dot-dashed ones to $d_{5/2}$. Therefore, different relative weights for both orbitals lead to different shapes of the total cross section, so its comparison to the experimental shape has spectroscopic value. Instead of trying to fit the shape of the distribution, we have represented the momentum distribution resulting from the sum of both waves scaled with the SF obtained from a shell-model calculation, as described in 4.2.2, showing the contribution of each orbital (dotted lines for $s_{1/2}$ and dot-dashed ones for $d_{5/2}$). Let us remark that since both PH and Dirac calculations have been rescaled to give the total integral of the data, the difference in magnitude for both calculations (with the Dirac cross section being 7% larger than

the PH one) is not apparent in the figure.

We find a good agreement in the distribution shape for the shell-model SF, which serves as a test for these values. As with the previous cases, both Dirac and PH yield distributions with very similar shapes, which are somewhat narrower than experimental data.

In general, we find a reasonably good agreement between experimental momentum distributions and our theoretical calculations, although the former seem to be systematically broader than the latter. We also find that the shape of momentum distributions is rather insensitive to the prescription for optical potentials chosen, even with the magnitude of the full cross section showing a stronger dependence on these potentials, as will be shown in the following section.

A thorough comparison between the distributions produced with PH and Dirac potentials seems to show that the calculation resulting in a smaller cross section tends to produce a (slightly) narrower cross section. This would relate a stronger absorption to a narrower momentum distribution, which agrees with the qualitative description in Sec. 2.5.2. Given that our distributions are narrower than experimental ones, this could indicate an overestimation of the effect of absorption in our calculations.

Another explanation for the narrowness of our distributions is the effect of energy dependence in the potentials. As was shown in Sec. 3.1, the inclusion of energy dependence for the optical potentials in DWIA calculations broadens slightly the distributions without modifying much the total magnitude. Since we are not including energy-dependence, our distributions may be narrower for this exclusion.

In spite of the previous caveats, we find the agreement between our calculations and the momentum distributions to be in general good for all of the considered cases, which span nuclei with high and low nucleon binding energies, and as such, take it as a validation of the method, which will in the following be applied to study the systematics of the "quenching factors" R_s.

4.2.4 Comparison with integrated cross section. "Quenching factors"

In this section we present our results for the "quenching factors" R_s, the ratios between experimental and theoretical cross sections and which have

Reaction	E/A (MeV)	$S_{p(n)}$ (MeV)	Ref	Reaction	E/A (MeV)	$S_{p(n)}$ (MeV)	Ref
^{13}O$(p,2p)$	401	1.51	[23]	^{21}O$(p,2p)$	449	20.99	[23]
^{14}O$(p,2p)$	351	4.63	[23]	^{21}N(p,pn)	417	4.59	[43]
^{15}O$(p,2p)$	310	7.30	[23]	^{21}N$(p,2p)$	417	19.60	[43]
^{16}O$(p,2p)$	451	12.13	[23]	^{22}O(p,pn)	414	6.85	[43]
^{17}O$(p,2p)$	406	13.78	[23]	^{22}O$(p,2p)$	414	23.26	[43]
^{18}O$(p,2p)$	368	15.94	[23]	^{23}O(p,pn)	445	2.73	[43]
^{12}C$(p,2p)$	398	15.96	[42]	^{23}O$(p,2p)$	445	24.71	[43]

Table 4.3: Detail of the reactions considered, with the incident energy of the beam, the separation energy of the removed nucleon (proton for $(p,2p)$ and neutron for (p,pn)) and the reference from which experimental data have been taken.

already been described in the introduction.

As described in Secs. 4.2.2, only (p,pN) processes leading to states of the residual core which are below the nucleon separation energy and which give a SF larger than 0.1 are considered. Single-particle cross sections (with SF=1) have been computed using both Dirac and PH potentials in order to test the dependence of our results to the choice of potential and they are used to compute total theoretical cross section through Eq. 4.1, as in Sec. 4.1.1.

Single-particle cross sections have been computed for the different states assuming a certain orbital from which the nucleon is removed. These single particle cross sections are detailed in Appendix A. When two states correspond to the same orbital and lie close in energy we have opted to use the same σ_{sp} for both states, usually taking the value computed for the state which lies lower in energy. States for which the σ_{sp} has not been computed present an asterisk in the value of σ_{sp}.

Theoretical cross sections have been computed for all the cases presented in Table 4.3, which are the ones that have been published by the R^{3}B collaboration up to the date of composition of this document. For ^{22}O$(p,2p)$ and ^{23}O$(p,2p)$, two different but compatible analysis were performed in [43] and [23]. We have taken the experimental cross sections from [43] in both cases.

For all of these reactions, the "quenching factors" $R_s = \sigma_{th}/\sigma_{exp}$ have been computed, using both Dirac and PH potentials. The values are shown in Table 4.4. The R_s are presented as a function of ΔS ($S_p - S_n$ for $(p,2p)$ reactions and $S_n - S_p$ for (p,pn) ones) in Fig. 4.11 in order to study their dependence on ΔS and compare it to that found in knockout experiments with heavier targets [31, 32]. In the figure, R_s factors from [23, 42], which

were obtained using an eikonal DWIA formalism [52], are also shown as well as those from [43], which were obtained from the Faddeev/AGS formalism. The errors in R_s have been propagated from the errors in the experimental cross sections.

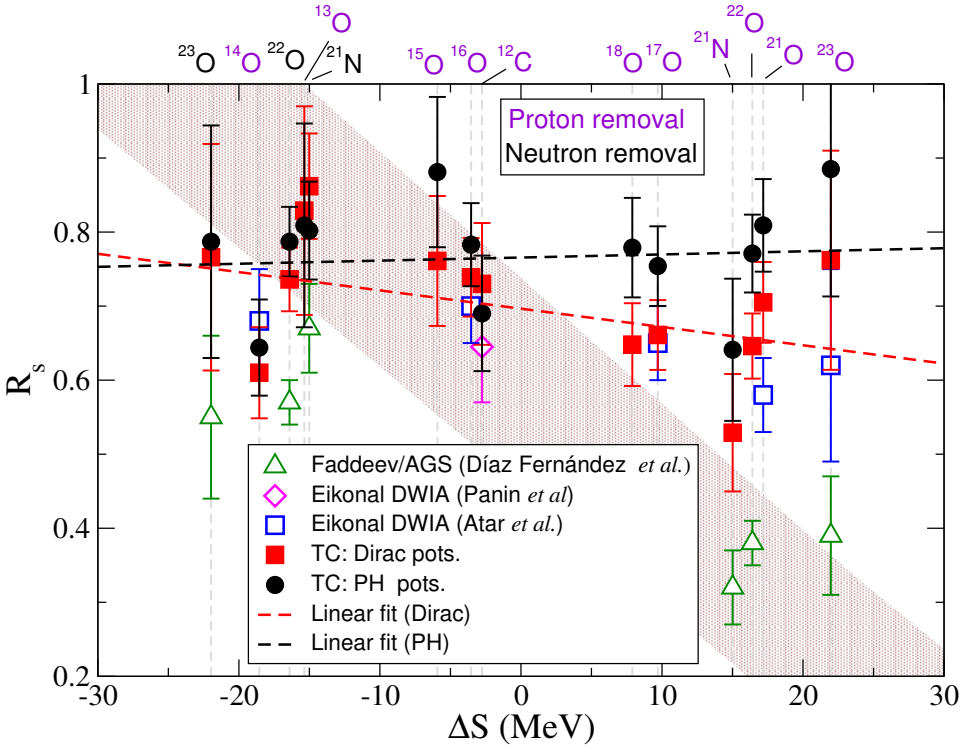

Figure 4.11: "Quenching factors" R_s as a function of ΔS, the difference between proton and neutron separation energy. Results from this work are presented in black circles using PH potentials and in red squares using Dirac potentials. The brown band corresponds to the systematics found in knock-out experiments [31, 32]. R_s from [43], [23] and [42] are presented in green triangles, blue squares and pink diamonds respectively.

Despite the relatively large dispersion in the values of R_s for both potential sets, in particular for PH potentials, it can be clearly seen that both sets of R_s present a dependence on ΔS which is much milder than the one found in knockout experiments (represented with the shaded area). In order to quantify their dependence on ΔS, both sets of quenching factors have been fitted with a linear function, which is presented in Fig. 4.11 in a dashed line (black for PH and red for Dirac). We obtain from this fit a dependence such as $R_s = 0.697(17) - 2.5(12) \cdot 10^{-3}\Delta S$ for the calculations employing

Dirac potentials and $R_s = 0.766(18) + 0.4(13) \cdot 10^{-3}\Delta S$ for the calculations with Paris-Hamburg potentials. The corresponding reduced χ^2 values are, 1.15 and 0.76, for Dirac and PH calculations, respectively. The very small value of the slope for both sets of calculations serves as a clear indication of the small dependence of the reduction factors on ΔS. It is rather remarkable that the slope for PH potentials is positive instead of negative. However, given that the error error of the slope is larger than its value, we can only conclude from its value that the PH calculation is compatible with a flat R_s with no dependence on ΔS.

When comparing our results with those from [23] and [42] we find that the agreement is reasonably good for ^{14}O, ^{16}O, ^{12}C and ^{17}O, with our R_s being overall larger than those from [23] and [42]. However, for ^{21}O and ^{23}O, our R_s show a marked disagreement with those of [23]. First, we must remark that we are using SF resulting from shell model calculations while in [23] they used the independent particle model (so that the associated SF are 2 for $^{21}\mathrm{O}(p, 2p)$ and $^{23}\mathrm{O}(p, 2p)$). As can be seen in Table 4.4, the total SF for $^{23}\mathrm{O}(p, 2p)$ is quite close to 2, so the comparison is meaningful at this respect. This is not the case for $^{21}\mathrm{O}(p, 2p)$, where the total SF is 1.88. However, if we assume a SF of 2 to compare to the R_s from [23], we obtain a R_s of 0.67±0.05 with Dirac potentials and one of 0.76(6) with PH potentials, which are still incompatible to the $R_s = 0.58(4)$ from [23].

Given that both analyses are based in different formalisms which use different inputs (in particular different optical potentials) it can be argued that the comparison between results of such different analyses is not meaningful. However, the eikonal DWIA used in [23] is formally similar to the one presented in the benchmark calculation in Sec. 3.1, where we found an excellent agreement when using the same input ingredients. As well, the agreement found for the other nuclei (^{14}O, ^{16}O, ^{12}C and ^{17}O) seems to suggest that both formalisms are reasonably compatible.

We note that the nuclei for which the disagreement is larger are located to the right of Fig. 4.11, so that they correspond to the knockout of the most bound species of the nucleus. We also note that, overall, the agreement between TC calculations with PH and Dirac potentials is better to the left of the figure (for removal of less bound species) than to the right (for removal of more tightly bound nucleons). This suggests that TC (p, pn) and $(p, 2p)$ cross sections for more deeply bound nuclei are more sensitive to the optical

potentials describing the interaction between nucleon and nucleus.

In order to test this idea, we have chosen the ^{23}O(p,pn) and ^{23}O$(p,2p)$ reactions, which are situated to the extremes of Fig. 4.11 and we have performed a "notch test": we have added a deep and very narrow Gaussian term ($V(r) = V_0 e^{-(r/a)^2}$ V_0=-50 MeV, a=0.2 fm) to the potential $V_{p^{23}\mathrm{O}}$ and have analyzed the sensitivity of the cross section to the position of the notch. In order to speed up calculations, this test has only been performed on the cross section leading to $p-N$ states with $j^\pi = 1^-$, which yield the largest cross section (See Sec. 2.5.1). The results of the test are presented in the left column of Fig. 4.12, where the black line denotes the relative change in the cross section as a function of the position of the node.

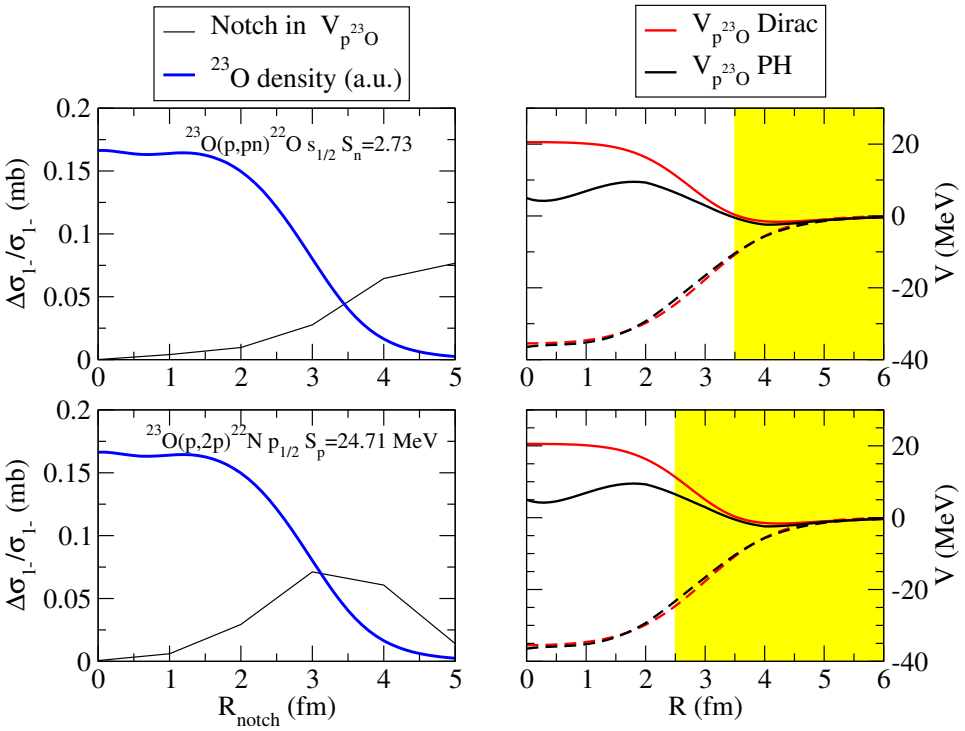

Figure 4.12: To the left, "notch test" performed on the ^{23}O(p,pn) and ^{23}O$(p,2p)$ reactions (see text). The thin black line corresponds to the relative variation of the cross section with the position of the notch. The density of ^{23}O is shown in arbitrary units for comparison. To the right the Dirac and PH potentials for ^{23}O are presented, the yellow area denoting the "area of sensitivity" which starts roughly at the position where the notch changes the cross section by ∼5%.

As can be expected, when the notch is situated at small distances, the

cross section is only weakly sensitive to it. This is an indication of the peripherality of the reaction and a result of the strong absorption of the potentials. As the notch moves to larger distances, the reaction becomes more sensitive to it and the cross section varies more strongly. We note that the ^{23}O(p, pn) reaction seems to require the notch to be at larger distances to be sensitive to it than the ^{23}O$(p, 2p)$ reaction: for the former the cross section is modified by $\sim$5% when the notch is found at $\sim$3.5 fm, while for the latter this modification is already found at $\sim$2.5 fm. In Fig. 4.12 the density of ^{23}O is also plotted in arbitrary units. From the notch test we can see that the ^{23}O(p, pn) reaction is clearly sensitive only to the tail region of the density distribution, while the ^{23}O$(p, 2p)$ one is more sensitive to the interior. This can be easily understood by noting that the wave function of a more deeply bound nucleon (such as the proton in ^{23}O) drops exponentially faster and is more concentrated near the origin. Therefore, in order to extract the nucleon the incoming proton has to probe deeper inside the nucleus, thus being more sensitive to the features of the interaction in this deeper area. This also relates naturally to the reduction of the cross section with separation energy, a larger separation energy requires the proton to probe deeper regions where absorption is stronger.

Taking (rather arbitrarily) the position of the notch for which the cross section is changed 5% as the radius of sensitivity for the reaction, we can check which areas of the $V_{p^{23}\mathrm{O}}$ potential are explored by the reaction. This is shown in the right column of Fig. 4.12, where starting at the radius of sensitivity, the "area of sensitivity" is presented in yellow. We can see that for the ^{23}O(p, pn) reaction, this area corresponds to the tail of the potentials, where PH and Dirac potentials are rather similar. On the other hand, the ^{23}O$(p, 2p)$ is sensitive to deeper regions where potentials differ more strongly, thus leading to more different cross sections.

We admit this description to be rather heuristic and phenomenological but we find it gives a qualitative and intuitive explanation for the differences found between the PH and Dirac calculations and between them and the results from [23] (where the nucleon-nucleus interactions are obtained through a very different method [52]).

We now compare our results to those presented in [43] (open triangles in Fig. 4.11), finding a larger disagreement. For the negative ΔS, the difference is of about 25%, while for the positive ΔS, our R_s are about twice larger

than those from [43]. More importantly, their results seem to show a greater dependence on ΔS than ours. Given the relatively good agreement found in the benchmark calculation with the Faddeev/AGS formalism (See Sec. 3.2), this disagreement cannot be fully attributed to the difference in the used formalisms.

We note three main differences between our reaction inputs and those of [43]:

1. The geometry of the binding potential: Here we use, as described in Sec. 4.2.2 a diffuseness $a = 0.7$ fm and a radius adjusted to give the Hartree-Fock rms radius. In [43] the geometry was taken as $a = 0.65$ fm and $r_0 = 1.25$ fm.

2. The optical potentials: Here we use Dirac and PH potentials, while in [43] they use Köning-Delaroche (KD) potentials.

3. Relativistic corrections: Here we have used the relativistic corrections described in Sec. 2.3, while in [43] the calculation was performed non-relativistically.

In order to check whether the discrepancies in the R_s values stem from these differences in the analysis, we have performed a calculation where we have tried to emulate all of the mentioned features of the analysis in [43]. The result is presented in Fig. 4.13. As can be seen in the figure the agreement between our new calculation and that of [43] is improved substantially. Most notably, the ΔS dependence of the new calculation is increased, becoming similar to that of [43]. Our R_s keep being larger than those of [43], resulting from smaller single-particle cross sections when compared to Faddeev/AGS ones. This is consistent with the results found in the benchmark calculation with the Reid93 potential in Sec. 3.2.

From this comparison we conclude that the stronger ΔS dependence found in [43] is largely related to the inputs used in the calculation. In particular we find that the use of KD potentials increases heavily the cross sections, due to their relatively small absorption when compared to PH and Dirac potentials, as can be seen in Fig. 4.14. KD potentials have been fitted for proton energies up to 200 MeV, so their use in reactions of $\sim$400 MeV/A can be put into question, trusting better calculations using PH and Dirac

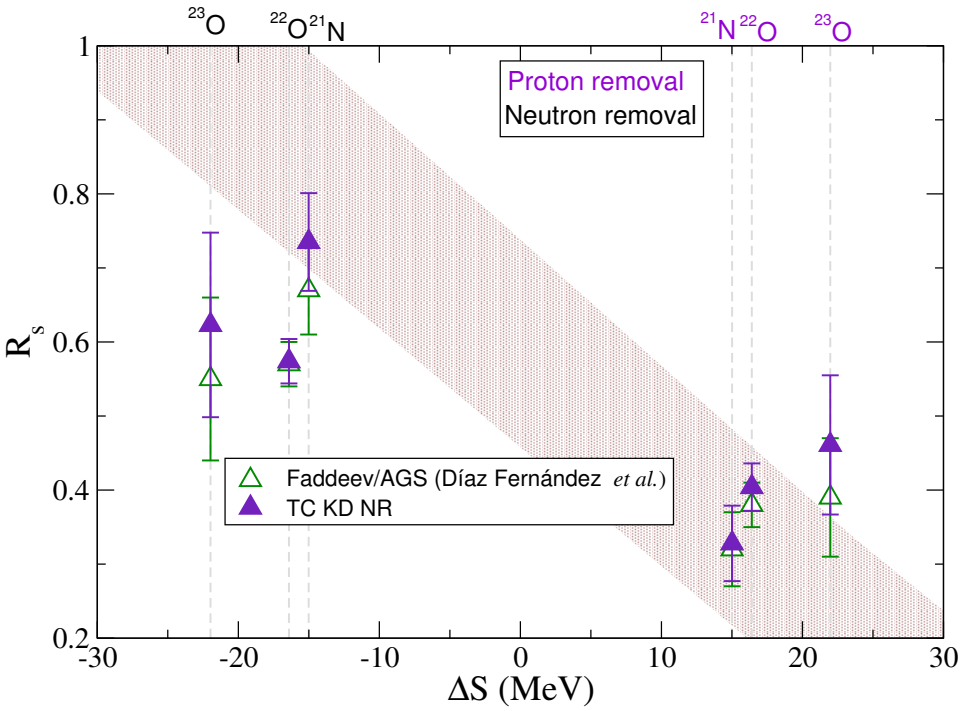

Figure 4.13: R_s from Faddeev/AGS calculations [43] (open green triangles) and from a TC calculation (in violet triangles) where KD potentials have been used, relativistic corrections omitted and the geometry of the binding potentials modified to $r_0 = 1.25$ fm, $a = 0.65$ fm, following the prescription from [43].

potentials, which have been adjusted to reproduce data in the energy range of the reactions we are studying.

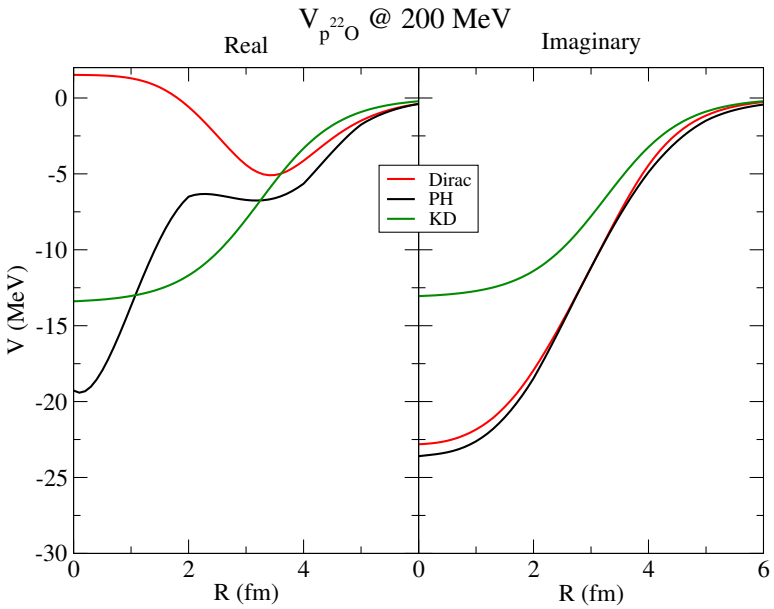

Figure 4.14: Comparison of Dirac, PH and KD potentials for p + ^{22}O at 200 MeV.

For these calculation, the weak dependence of the R_s on ΔS is a solid conclusion obtained using both PH and Dirac potential sets, which agrees, at least semi-quantitatively, with the analysis from [23], performed on only five of the reactions considered here. It is also consistent with the recent conclusions for transfer reactions on oxygen and argon [33, 37, 40] as well as on systematic studies on transfer reactions [10]. A small ΔS is also reported on exclusive $(p, 2p)$ measurements in [44] and has been obtained from state-of-the-art *ab-initio* calculations reported for the proton-hole strength based on the self-consistent Green's function (SCGF) theory [100].

Reaction	$\sum C^2S_{1p_{3/2}}$	$\sum C^2S_{1p_{1/2}}$	$\sum C^2S_{1d_{5/2}}$	$\sum C^2S_{2s_{1/2}}$	$\sigma_{\rm sp}$	$\sigma_{\rm th}$	$\sigma_{\rm exp}$	R_s
^{13}O$(p,2p)$	–	0.66	–	–	10.562 10.813	6.975 7.140	5.78(0.91)[0.37]	0.83(14) 0.81(14)
^{14}O$(p,2p)$	–	1.97	–	–	8.509 8.065	16.769 15.895	10.23(0.80)[0.65]	0.61(6) 0.64(6)
^{15}O$(p,2p)$	1.94	1.60	–	–	7.026 6.072	24.856 21.481	18.92(1.82)[1.20]	0.76(9) 0.88(10)
^{16}O$(p,2p)$	4.09	2.00	–	–	5.965 5.631	36.308 34.279	26.84(0.90)[1.70]	0.74(5) 0.78(6)
^{17}O$(p,2p)$	–	2.07	–		5.777 5.064	11.944 10.471	7.90(0.26)[0.50]	0.66(5) 0.75(5)
^{18}O$(p,2p)$	3.40	2.00	–	–	5.048 4.198	27.274 22.685	17.80(1.04)[1.13]	0.65(6) 0.78(7)
^{21}O$(p,2p)$	–	1.88	–	–	4.008 3.493	7.532 6.5656	5.31(0.23)[0.34]	0.71(5) 0.81(6)
^{21}N$(p,2p)$	0.33	0.72	–	–	4.118 3.398	4.290 3.540	2.27(0.34)	0.53(8) 0.64(10)
^{21}N(p,pn)	–	–	4.95	0.65	10.059 10.809	56.274 60.471	48.52(4.04)	0.86(7) 0.80(7)
^{22}O$(p,2p)$	0.73	1.87	–	–	3.533 2.962	9.175 7.693	6.01(0.41)	0.65(4) 0.77(5)
^{22}O(p,pn)	–	–	5.89	0.25	8.690 8.122	53.349 49.865	39.24(2.34)	0.74(4) 0.79(5)
^{23}O$(p,2p)$	–	1.99	–	–	3.302 2.844	6.577 5.663	4.93(0.96)	0.76(15) 0.89(17)
^{23}O(p,pn)	–	1.13	5.89	1.00	8.765 8.536	70.474 68.636	54.0(10.8)	0.77(15) 0.79(16)
^{12}C$(p,2p)$	3.65	0.63	–	–	6.143 6.498	26.298 27.816	19.2(1.8)[1.2]	0.73(8) 0.69(8)

Table 4.4: Experimental [23, 42, 43] and calculated cross sections. The second to fifth columns correspond to the sum of the spectroscopic factors from the prediction of shell-model calculations for the indicated waves, restricted to bound states of the residual *core*. The next column indicates the single particle cross section $\sigma_{\rm sp}$, computed using Dirac (upper value) and PH (lower value) potentials. Next the theoretical cross section $\sigma_{\rm th} = \sum C^2S\sigma_{\rm sp}$, and the experimental cross sections $\sigma_{\rm exp}$ are presented. Finally the quenching factor $R_s = \sigma_{\rm exp}/\sigma_{\rm th}$ is shown.

Chapter 5

Application of (p, pN) reactions to Borromean nuclei

There are things known and there are things unknown and in between are the doors of perception.

Aldous Huxley

In this chapter, we extend and apply the Transfer to the Continuum formalism to (p, pN) reactions induced by Borromean nuclei. As mentioned in the introduction, when a nucleon N_1 is removed from a Borromean nucleus $N_1 + N_2 + C$, the two-body system that is left, $N_2 + C$, is unbound and will decay trough the emission of the remaining nucleon. Through the measurement of the momenta of the decay products N_2 and C, it is possible to reconstruct the energy and momentum distributions of the residual system $N_2 + C$, thus exploring the properties of an unbound system which is otherwise difficult to study. Under some assumptions, this is expected to provide valuable information on two-body correlations within the original 3-body nucleus. We will focus mainly on the study of the energy distribution of the residual system. For this, an extension of the Transfer to the Continuum formalism is necessary, which will be developed in Sec. 5.1, while results for the $^{11}\mathrm{Li}(p, pn)^{10}\mathrm{Li}^*$ reaction will be presented in Sec. 5.2.

5.1 Extension of the formalism

In order to extend the formalism to the case of Borromean nuclei, let us start by establishing a slightly different notation: first, the target nucleus (projectile in inverse kinematics) will be denoted by A and we will model it as three particles: two nucleons and a core $N_1 + N_2 + C$. After the removal of one of the nucleons, which we will denote as N_1, an unbound residual system is left, which we will denote as $B = N_2 + C$. As such, the residual nucleus B takes the place of the residual nucleus C in the formalism developed in Chapter 2.

As we did in Eq. (2.15), we will expand the part of the wavefunction corresponding to the final partition Ψ_b in the basis of the eigenstates of the residual nucleus $B = N_2 + C$.

$$\Psi_b = \sum_{B_\alpha} \Psi^{3.b.}_{bB_\alpha} \Phi_{B_\alpha}, \tag{5.1}$$

where B_α denotes the possible states of the two-body system $B_\alpha = N_2 + C$. Now we will adopt a two-body model for B where we will take N_2 and C as inert. Within this model, the state of B can be described fully through the relative motion between N_2 and C and their spin projections. We will express the relative motion using the relative coordinate $\mathbf{x}$, and the associated relative momentum as $\mathbf{q}$. As such we can denote an eigenstate of the unbound system B as

$$\Phi_{B_\alpha} = \varphi^{(-)}_{\mathbf{q},\sigma_2,\varsigma}(\mathbf{x}), \tag{5.2}$$

where σ_2 and ς are the spin projections of N_2 and C respectively and as usual $(-)$ denotes incoming boundary conditions between N_2 and C. Let us note that the only requirement that we must impose on our set of states Φ_{B_α} is that they form a complete basis for the breakup of B. Therefore, we could have chosen $\varphi^{(+)}_{\mathbf{q},\sigma_2,\varsigma}$, but a description through $\varphi^{(-)}_{\mathbf{q},\sigma_2,\varsigma}$ is more suitable for the final states of the reaction. In fact, in order to compute $\varphi^{(-)}_{\mathbf{q},\sigma_2,\varsigma}$ we will instead compute $\varphi^{(+)}_{\mathbf{q},\sigma_2,\varsigma}$ [72], expanding it in the spin-orbit coupling scheme as:

$$\begin{aligned}\varphi^{(+)}_{\mathbf{q},\sigma_2,\varsigma}(\mathbf{x}) = \frac{4\pi}{qx} \sum_{LJL'J'J_TM_T} & i^{L'} Y^*_{LM}(\hat{q}) \, \langle LMs_2\sigma_2 | JM_J \rangle \\ & \times \langle JM_J I\varsigma | J_T M_T \rangle \, f^{J_T}_{LJ,L'J'}(q,x) \, [[Y_{L'}(\hat{x}) \otimes \chi_{s_2}]_{J'} \otimes \chi_I]_{J_TM_T} \,,\end{aligned} \tag{5.3}$$

where L is the orbital angular momentum between N_2 and C, s_2 and I are the spins of N_2 and C respectively and χ_{s_2}, χ_I are their spin wavefunctions. We choose the radial functions $f^{J_T}_{LJ}(q,x)$ to verify the usual scattering boundary conditions:

$$f^{J_T}_{LJ,L'J'}(q,x) \xrightarrow[x\to\infty]{} \frac{i}{2} e^{i\sigma_L} \left[H^{(-)}_L(qx)\delta_{LJ,L'J'} - S^{J_T}_{LJ,L'J'} H^{(+)}_L(qx) \right], \quad (5.4)$$

with $H^{(\pm)}$ being the Coulomb functions. To recover $\varphi^{(-)}_{\mathbf{q},\sigma_2,\varsigma}$ we will use the fact that $\varphi^{(-)}_{\mathbf{q},\sigma_2,\varsigma}$ is the time reverse of $\varphi^{(+)}_{\mathbf{q},\sigma_2,\varsigma}$ [72], which leads to an expression for $\varphi^{(-)}_{\mathbf{q},\sigma_2,\varsigma}$ such as:

$$\begin{aligned} \varphi^{(-)}_{\mathbf{q},\sigma_2,\varsigma}(\mathbf{x}) = \frac{4\pi}{qx} \sum_{LJL'J'J_TM_T} & i^{L'} Y^*_{LM}(\hat{q}) \, \langle LMs_2\sigma_2 | JM_J \rangle \\ & \times \langle JM_J I\varsigma | J_T M_T \rangle \, f^{J_T *}_{LJ,L'J'}(q,x) \left[[Y_{L'}(\hat{x}) \otimes \chi_{s_2}]_{J'} \otimes \chi_I \right]_{J_T M_T} . \end{aligned} \quad (5.5)$$

To provide a consistent description of nucleus A with that of nucleus B, the former will be modelled as a three-body system composed of the inert fragments N_1, N_2 and C, so that it only depends on Jacobi coordinates $\mathbf{x}$ and $\mathbf{y}$, as shown in Fig. 5.1.

The wavefunction for the ground state of A is expanded in hyperspherical harmonics [60, 101], leading to

$$\phi_A(\mathbf{x},\mathbf{y}) = \sum_{\beta_{3b}} w^j_{\beta_{3b}}(x,y) \left\{ \left[[Y_{l_x}(\hat{x}) \otimes \chi_{s_2}]_{j_x} \otimes \chi_I \right]_{j_1} \otimes \left[Y_{l_y}(\hat{y}) \otimes \chi_{s_1} \right]_{j_y} \right\}_{j\mu}, \quad (5.6)$$

where $\beta_{3b} = \{K, l_x, j_x, j_1, l_y, j_y\}$ is a set of quantum numbers fully describing the relative motion of the three particles N_1, N_2 and C. Here K is the hypermomentum, l_x and l_y are the orbital angular momenta associated to coordinates $\mathbf{x}$ and $\mathbf{y}$, respectively and j_x, j_1 and j_y result from the coupling of the orbital angular momenta to the spins of N_1, N_2 and C as shown in Eq. (5.6), with the restriction that the total angular momentum j must correspond to the spin of the ground state of A.

Now we express the total wavefunction in a similar way to Eq. (2.7),

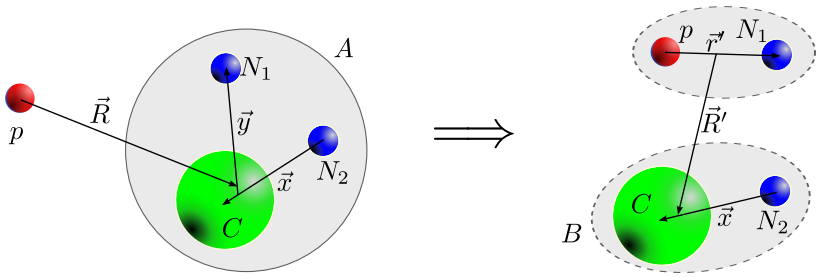

Figure 5.1: Scheme of a (p, pN) reaction on a three-body nucleus, with the relevant coordinates involved in the TC formalism.

expanding Ψ_b in the states defined by Eq. (5.5):

$$\begin{aligned}\Psi^{3\mathrm{b}(+)}(\mathbf{R},\mathbf{y},\mathbf{x}) &\simeq X_A(\mathbf{R})\phi_A(\mathbf{x},\mathbf{y}) + \Psi_b = \\ X_A(\mathbf{R})\phi_A(\mathbf{x},\mathbf{y}) &+ \int \mathrm{d}\mathbf{q} \sum_{\sigma_2,\varsigma} \varphi^{(-)}_{\mathbf{q},\sigma_2,\varsigma}(\mathbf{x}) \Psi^{3.b.}_{b\mathbf{q}\sigma_2\varsigma}(\mathbf{R}',\mathbf{r}').\end{aligned} \tag{5.7}$$

We will now impose a *participant-spectator* approximation, analogous to the *frozen core* approximation performed in Chapter 2, in which we will assume that the (p, pN) reaction only modifies the motion of the removed nucleon N_1, while the state of the residual nucleus B will not be affected by the reaction. As in Chapter 2, this results in the decoupling of the different states of B, which in the present case implies that the states with different $\mathbf{q}$, σ_2 and ς can be computed independently. The potentials in the reaction are assumed to be independent of the internal variables of B, which in this case corresponds to $\mathbf{x}$. As such, we can reach an equation equivalent to Eq. (2.28):

$$\int \mathrm{d}\mathbf{x} \varphi^{(-)*}_{\mathbf{q},\sigma_2,\varsigma}(\mathbf{x}) \phi_A(\mathbf{x},\mathbf{y}) = \varphi_{AB_{\mathbf{q},\sigma_2,\varsigma}}(\mathbf{y}), \tag{5.8}$$

where now we do not impose a normalization on $\varphi_{AB_{\mathbf{q},\sigma_2,\varsigma}}$. In order to have expressions with a defined total angular momentum, let us define

$$\begin{aligned}\varphi_{AB,LJJ_TM_T}(q,\mathbf{y}) = &\sum_{L'J'} i^{L'} \int \mathrm{d}\mathbf{x} \frac{f^{J_T}_{LJ,L'J'}(q,x)}{x} \left[[Y_{L'}(\hat{x}) \otimes \chi_{s_2}]_{J'} \otimes \chi_I\right]^*_{J_TM_T} \\ &\times \phi_A(\mathbf{x},\mathbf{y}),\end{aligned} \tag{5.9}$$

where it is rather trivial to obtain:

$$\begin{aligned}\varphi_{AB_{\mathbf{q},\sigma_2,\varsigma}}(\mathbf{y}) = \frac{4\pi}{q} \sum_{LJJ_TM_T} & Y_{LM}(\hat{q}) \langle LMs_2\sigma_2|JM_J\rangle \\ & \times \langle JM_JI\varsigma|J_TM_T\rangle \, \varphi_{AB,LJJ_TM_T}(q,\mathbf{y}).\end{aligned} \tag{5.10}$$

As in Chapter 2, we expand $\Psi^{3.b.}_{b\mathbf{q}\sigma_2\varsigma}$ in discretized states with good angular momentum and parity of the $p - N_1$ subsystem:

$$\Psi^{3b}_{b\mathbf{q}\sigma_2\varsigma} \simeq \sum_{j^\pi n} \tilde{\phi}^{j^\pi}_n X_{j^\pi n\alpha}, \tag{5.11}$$

and we can compute the transition matrix to a certain state of the $p - N_1$:

$$\begin{aligned}\mathcal{T}^{if}_{\mathbf{q},\sigma_2,\varsigma,n,j^\pi} &= \left\langle \varphi^{(-)}_{\mathbf{q},\sigma_2,\varsigma} \tilde{\phi}^{j^\pi}_n X^{\mathbf{q},\sigma_2,\varsigma}_{j^\pi n\alpha} | V_{pN} + U_{pB} - U_{pA} | X_A\phi_A \right\rangle \\ &= \left\langle \tilde{\phi}^{j^\pi}_n X^{\mathbf{q},\sigma_2,\varsigma}_{j^\pi n\alpha} | V_{pN} + U_{pB} - U_{pA} | X_A\varphi_{AB_{\mathbf{q},\sigma_2,\varsigma}} \right\rangle,\end{aligned} \tag{5.12}$$

where in the second line, we have made use of Eq. 5.8 and Eq. 5.9 under the assumption that the potentials appearing in the matrix element are independent of $\mathbf{x}$, so that they can be extracted from the integration over it. We can transform the transition matrix to:

$$\begin{aligned}\mathcal{T}^{if}_{\mathbf{q},\sigma_2,\varsigma,n,j^\pi} &= \frac{4\pi}{q} \sum_{LJJ_TM_T} Y_{LM}(\hat{q}) \langle LMs_2\sigma_2|JM_J\rangle \langle JM_JI\varsigma|J_TM_T\rangle \\ &\times \left\langle \tilde{\phi}^{j^\pi}_n X^{LJJ_TM_T}_{j^\pi n\alpha} | V_{pN} + U_{pB} - U_{pA} | X_A\varphi_{AB,LJJ_TM_T} \right\rangle \\ &= \frac{4\pi}{q} \sum_\alpha Y_{LM}(\hat{q}) \langle LMs_2\sigma_2|JM_J\rangle \langle JM_JI\varsigma|J_TM_T\rangle \, \mathcal{T}^{if}_\alpha,\end{aligned} \tag{5.13}$$

where $\alpha = \{LJJ_TM_T, nj^\pi\}$. Now we note that each of the $\mathcal{T}^{if}_\alpha$ can be computed independently as an independent (p, pN) reaction, and therefore, the TC formalism can be applied to obtain it as described in Chapter 2. Let us now get the cross section leading to a certain final state, $\varphi^{(-)}_{\mathbf{q},\sigma_2,\varsigma}$ and a certain state of the $p - N_1$ subsystem $\tilde{\phi}^{j^\pi}_n$:

$$\left.\frac{\mathrm{d}\sigma}{\mathrm{d}\Omega}\right|^{n,j^\pi}_{\mathbf{q},\sigma_2,\varsigma} = \frac{1}{(2s_p+1)(2J_A+1)} \frac{\mu_{pA}\mu_{pn-C}}{(2\pi\hbar^2)^2} \frac{K_f}{K_{pA}} \sum_m \left| \mathcal{T}^{if}_{\mathbf{q},\sigma_2,\varsigma,n,j^\pi} \right|^2, \tag{5.14}$$

where as in Chapter 2, Ω corresponds to the scattering angle of the (center of mass of) residual nucleus B.

Now we can apply the decomposition:

$$\left.\frac{\mathrm{d}\sigma}{\mathrm{d}\Omega}\right|_{\mathbf{q},\sigma_2,\varsigma}^{n,j^\pi} = \frac{1}{(2s_p+1)(2J_A+1)}\frac{\mu_{pA}\mu_{pn-C}}{(2\pi\hbar^2)^2}\frac{K_f}{K_{pA}}\frac{16\pi^2}{q^2} \times \sum_{m_p,m_A,m_d,M_T}\left|\sum_\alpha Y_{LM}(\hat{q})\,\langle LMs_2\sigma_2|JM_J\rangle\,\langle JM_JI\varsigma|J_TM_T\rangle\,\mathcal{T}_\alpha^{if}\right|^2, \tag{5.15}$$

where we now explicitly state the spin projections of the nuclei involved in the reaction. In order to produce a differential cross section on $\mathbf{q}$, we multiply by the differential element and the number of states per momentum-space element ($N(\mathbf{q})$), which for our definition corresponds to [71]:

$$N(\mathbf{q}) = (2\pi)^{-3}, \tag{5.16}$$

which we note does not depend on $\mathbf{q}$, so we will denote it as N_q. This expression leads to:

$$\left.\frac{\mathrm{d}\sigma}{\mathrm{d}\Omega\mathrm{d}\mathbf{q}}\right|_{\sigma_2,\varsigma}^{n,j^\pi} = \left.\frac{\mathrm{d}\sigma}{\mathrm{d}\Omega}\right|_{\mathbf{q},\sigma_2,\varsigma} N_q\mathrm{d}^3\mathbf{q}. \tag{5.17}$$

Since we are only interested in the energy distribution of the residual nucleus B, we may integrate over the angles of $\mathbf{q}$ and sum over the spin projections of both N_2 and C, that is over σ_2 and ς. Now we can use the properties:

$$\int \mathrm{d}\hat{q}Y_{LM}^*(\hat{q})Y_{L''M''}(\hat{q}) = \delta_{LL''}\delta_{MM''} \tag{5.18}$$

and

$$\sum_{M,\sigma_2}\langle LMs_2\sigma_2|JM_J\rangle\,\langle LMs_2\sigma_2|J^{''}M_J\rangle = \delta_{JJ''} \tag{5.19}$$

to get an expression for the cross section to a certain q

$$\left.\frac{\mathrm{d}\sigma}{\mathrm{d}\Omega\mathrm{d}q}\right|^{n,j^\pi} = \frac{1}{(2s_p+1)(2J_A+1)}\frac{\mu_{pA}\mu_{pn-C}}{(2\pi\hbar^2)^2}\frac{K_f}{K_{pA}}16\pi^2 \times \sum_{m_p,m_A,m_d,M_T}\left|\sum_\alpha \mathcal{T}_{LMJ_TM_T}^{if}\right|^2 N_q, \tag{5.20}$$

which can be easily recognised as

$$\left.\frac{\mathrm{d}\sigma}{\mathrm{d}\Omega \mathrm{d}q}\right|^{n,j^\pi} = 16\pi^2 N_q \sum_{LJJ_TM_T} \left.\frac{\mathrm{d}\sigma}{\mathrm{d}\Omega}\right|_{q,\alpha}. \tag{5.21}$$

The cross section to a state $\{LJJ_TM_T\}$ can be computed using TC by summing over the cross sections to all the bins:

$$\frac{\mathrm{d}\sigma}{\mathrm{d}\Omega \mathrm{d}q} = 16\pi^2 \sum_{\alpha} \left.\frac{\mathrm{d}\sigma}{\mathrm{d}\Omega}\right|_{q,\alpha} N_q. \tag{5.22}$$

Of course, integration over Ω yields the formula for the differential cross section with the modulus of q:

$$\frac{\mathrm{d}\sigma}{\mathrm{d}q} = 16\pi^2 \sum_{\alpha} \sigma|_{q,\alpha} N_q. \tag{5.23}$$

From here, we can easily obtain the distribution for the relative energy between N_2 and C, by multiplying by transforming from momentum to energy through:

$$\epsilon_{N_2C} = \frac{\hbar^2 q^2}{2\mu_{N_2C}} \qquad \frac{\mathrm{d}q}{\mathrm{d}\epsilon_{N_2C}} = \frac{\mu_{N_2C}}{\hbar^2 q} \tag{5.24}$$

leading to:

$$\frac{\mathrm{d}\sigma}{\mathrm{d}\epsilon_{N_2C}} = 16\pi^2 \frac{\mu_{N_2C}}{\hbar^2 q} N_q \sum_{\alpha} \sigma|_{q,\alpha} \tag{5.25}$$

Here the use of the non-relativistic expression for the density of states is justified by the low relative energies between N_2 and C, which tend to encompass only a few MeV. Finally let us note that in the previous derivation neither the integration over Ω nor the sum over the different bins n, j^π is a fundamental part of the derivation. As such it is possible to obtain a differential cross section over ϵ_{N_2C} and the center of mass momentum of the outgoing residual nucleus B (see Section 2.2) which still verifies the property that it can be constructed through the incoherent sum of the differential cross sections for the different states $\{LJJ_TM_T\}$.

5.1.1 Comment on antisymmetrization

Borromean systems in which two of the bodies are nucleons (the ones we are interested in in this work) must be of the type $n + n + C$ or $p + p + C$, since a system such as $p + n + C$ would not be Borromean, since the two-body subsystem $p+n$ can be bound forming the deuteron. Therefore, special attention must be paid to the fact that the two nucleons are identical particles so they must be properly antisymmetrized. This antisymmetrization must be taken into account in the calculation of ϕ_A, and is most easily considered by working in the T-system, where the orbital angular momentum between the two nucleons is defined. There, the components where $L + S$ (with $S = s_{N1} + s_{N2}$) is odd can be removed, and those where it is even multiplied by a factor $\sqrt{2}$, in a similar way to Section 2.4. We must then transform the wavefunction to the Y-system as in Eq. (5.6), since there the overlap with nucleus B is simpler. Let us remark that in the actual calculations it is common to leave the factor $\sqrt{2}$ out of the calculation, so that the final cross sections obtained must be multiplied by a factor 2.

5.2 ^{11}Li$(p, pn)^{10}$Li*

5.2.1 Brief introduction

^{11}Li has the honour of being the first established halo nucleus, after the experiments by Tanihata *et al* [102] showed it to have a interaction cross section which was much larger than other nuclei of its neighbourhood. This was interpreted as ^{11}Li having a much larger radius, which was later understood as having two valence neutrons orbiting a ^{9}Li core at a large radius, forming the halo.

Despite the numerous experiments performed on ^{11}Li, the structure of its ground state is not clearly established yet. It is experimentally agreed upon that the ground state of ^{11}Li is an admixture of $s^2_{1/2}$ and $p^2_{1/2}$ [103], but the weight of each component is not clear, with predictions for the weight of the $(sd)^2$ component ranging from 0 to 100% [104], with the predictions for the s^2 occupation based on the matter radius of ^{11}Li being around 30-50%.

The associated unbound system ^{10}Li presents a spectrum that has yet to be clarified as well, as can be seen from Table 5.1, which has been adapted from [104]. Currently, the general consensus is that the ground state of ^{10}Li

Year	Reaction	Energy (MeV)	Width (MeV)	l	Ref
1997	^{10}Be(^{12}C,^{12}N)	0.24(4)	0.10(7)		[105]
1999	^{9}Be(^{9}Be,^{8}B)	0.50(6)	0.40(6)		[106]
1999	fragmentation	$<$0.05		s	[107]
2001	p removal from ^{11}Be			g.s. is s	[108]
2003	^{9}Li(d,p)	0.35(11) or $<$0.2 and 0.77(24)	$<$0.32 – and 0.62		[109]
2006	^{9}Li(d,p)	$\sim$0 $\sim$0.38	 $\sim$0.2	s p	[110]
2015	$2p$ removal from ^{12}Be	0.11(4) 0.50(10)	0.2 0.8	p p	[111]
2016	^{11}Li(p,d)	0.62(4)	0.33(7)	p	[112]

Table 5.1: Position of the resonances and virtual states found for ^{10}Li in various experiments, adapted from [104]

corresponds to a s wave with an energy very close to threshold and that it has one or more resonances corresponding to a p wave in the range of 0.2-0.7 MeV.

5.2.2 Models for ^{11}Li and ^{10}Li

As was indicated in Sec. 5.1, the main structure ingredient required for the computation of the (p,pn) energy distribution is the overlap between the ground state of the Borromean nucleus (^{11}Li) and the unbound residual two-body system (^{10}Li) at different n+^{9}Li relative energies. In order to produce this overlap, the wave functions of both systems have to be produced, in this case, employing a 3-body model for ^{11}Li ($n+n$+^{9}Li) and a two-body one for ^{10}Li (n+^{9}Li).

The main input ingredients for these models are the potentials between the subsystems considered. Given that in the three body system two of the particles considered are identical (the two neutrons) only two potentials are required in these calculations: V_{nn} and $V_{n^9\mathrm{Li}}$.

For V_{nn}, the well tested GPT interaction [113] has been chosen, which is able to reproduce the scattering length for this system. Given that the relevant energy range between the two neutrons inside ^{11}Li will be relatively small, $E_{nn} < 5$ MeV, we find that a good description of the scattering length is enough to describe the $n-n$ interaction.

The n–^{9}Li interaction is less well established since the properties of ^{10}Li are not that well known. As such, we have produced 5 different interactions

which yield different spectra for ^{10}Li. This allows us to explore the sensitivity of the reaction observables to the characteristics of the $n-^9$Li continuum.

One main property of the $n-^9$Li interaction we explore in this work is the spin-spin coupling between n and ^{9}Li, which leads to splitting of the structures of the continuum (resonances and virtual states) depending on the relative orientation of the spins of both systems. The shapes for the interactions including spin-spin terms is different in the literature than that of the interactions excluding this term. As such distinctions must be made between them.

The interactions excluding spin-spin coupling have been based in the parametrization of Thompson and Zhukov [114]:

$$V^{(L)}_{n^9\mathrm{Li}} = V^{(L)}_c(x) + V^{(L)}_{so-v}(x)\mathbf{L}\cdot\mathbf{s_n}, \tag{5.26}$$

where the depth of the interactions depend on the orbital angular momentum (L) between n and ^{9}Li, with the central term following a Woods-Saxon shape and the spin-orbit term following a Woods-Saxon derivative, both with geometries with the parameters $R = 2.642$ fm (note it is R and not r_0) and $a = 0.67$ fm. Meanwhile the interactions including spin-spin coupling are based on the parametrization of Garrido *et al.* [115]:

$$V^{(L)}_{n^9\mathrm{Li}} = V^{(L)}_c(x) + V^{(L)}_{so-v}(x)\mathbf{L}\cdot\mathbf{s_n} + V^{(L)}_{so-C}(x)\mathbf{L}\cdot\mathbf{s_C} + V^{(L)}_{ss}(x)\mathbf{s_n}\cdot\mathbf{s_C}, \tag{5.27}$$

presenting central, spin-spin and spin orbit terms for both n and ^{9}Li spins. The geometry for these terms is Gaussian $V(r) = ve^{-r^2/a^2}$ with $a = 2.55$ fm. As in the previous case the depths of the potentials are L-dependent.

The depths of the different terms for the potentials considered in the following sections are presented in Table 5.2. The potentials with an I in their names (P1I and P2I) include spin-spin terms, while those without it (P3, P4 and P5) exclude them.

Looking at the depths of the central part for the s wave it can be seen that they are much shallower for P1I and P2I than for P3, P4 and P5. As well, we can see that for the p-wave the potential is highly repulsive for P1I and P2I. This is done to push out the $p_{3/2}$ component in what is called the repulsive core approach [116]. This method results in the s-wave states produced being $1s_{1/2}$ states, which do not present a node. We do not expect

Model	$v_c^{(0)}$	$v_c^{(1)}$	$v_c^{(2)}$	$v_{ss}^{(0)}$	$v_{ss}^{(1)}$	$v_{\text{so-c}}^{(1)}$	$v_{\text{so-v}}^{(1)}$
P1I	-5.4	260.75	–	-4.50	1.00	1.00	300
P2I	-5.0	260.25	–	-2.00	1.00	1.00	300
P3	-50.5	-39.0	-50.5	–	–	–	40.0
P4	-49.6	-39.4	-50.5	–	–	–	35.5
P3	-50.5	-39.0	-53	–	–	–	40.0

Table 5.2: Potential depths for the ^{11}Li models used in this work. Spin-orbit terms have the same depth for $L = 1, 2$ and spin-spin terms for $L = 0, 2$.

	$E_r[p_{1/2}]$ (MeV)		a (fm)		$E_r[d_{5/2}]$ (MeV)	$\%p_{1/2}$	$\%s_{1/2}$	$\%d_{5/2}$	r_{mat} (fm)	r_{ch} (fm)
	1^+	2^+	1^-	2^-						
P1I	0.37	0.61	–	-37.9	–	31	67	1	3.2	2.41
P2I	0.30	0.55	-1.1	-6.7	–	44	54	<1	3.0	2.40
P3	0.50		-29.8		4.3	30	64	3	3.6	2.48
P4	0.23		-16.2		4.3	67	27	3	3.3	2.43
P5	0.50		-29.8		1.5	35	39	23	3.2	2.42

Table 5.3: Features of the ^{10}Li structure for the different potentials employed in this work. The second column shows the energy of the $p_{1/2}$ resonance while the third one shows the scattering length of the $s_{1/2}$ virtual state. Note that for the model with spin, both the resonance and virtual state are split. The fourth column shows the position of the d-wave resonance, only for the models without spin. The fifth, sixth and seventh columns show the weights of the $p_{1/2}$, $s_{1/2}$ and $d_{5/2}$ waves in the ^{11}Li ground state respectively, while the last two columns show its matter and charge radii.

this to influence the energy distributions we intend to study, although it may change momentum distributions, which will not be explored in this work.

As for P3, P4 and P5, they produce deeply-bound $1s_{1/2}$ and $1p_{3/2}$ components which have to be removed from the spectrum using the adiabatic projection method [117].

Apart from these potentials, the three-body calculation for ^{11}Li includes a three-body force to reproduce the two-nucleon separation energy for ^{11}Li, $S_{2n} = -0.37$ MeV. Let us remark here that $V_{n^9\text{Li}}$ is used consistently for the calculations for ^{10}Li and ^{11}Li.

The features of the ^{10}Li continuum obtained for these potentials as well as the weight of the different waves for the $n-^9$Li system in the ^{11}Li ground state wave function are presented in Table 5.3. The charge and matter radii for ^{11}Li are also presented.

In our adjustment of potential depths, we have tried to reproduce the

overall features for the ^{10}Li continuum, a p-wave resonance at $\sim$0.5 MeV and a virtual state at low energies with a (negative) scattering length of $\sim 20 - 30$ fm for the P1I and P3 potentials. Let us note that, while we have a relative freedom to displace the position of the resonances and virtual states by changing the depths of the interaction, this also modifies strongly the weights of the associated waves in the ground state of ^{11}Li. This can be understood quite intuitively, as a resonance at lower energies is more easily populated as one at higher energies, so a model with a lower resonance in the p-wave will have a larger weight for this wave than one with the resonace at a higher energy, as can in fact be seen when comparing models P4 and P3.

Actually, models P2I and P4 have been produced, not to be "realistic", but to give a larger p-wave component. As can be seen in Table 5.3, this can only be achieved either by reducing the scattering length of the s-wave, as for P2I, effectively pushing the energy of the associated virtual state away from the threshold; or by reducing the energy of the p-wave resonance, as in P4.

This shows that our method establishes a relation between the energy of the structures in the ^{10}Li and the weight of their contribution, thus linking the height of the resonance peaks to their position. This severely restricts the distributions we can produce, thus endowing them with stronger spectroscopic capabilities.

5.2.3 ^{11}Li$(p, pn)^{10}$Li* at 280 MeV/A

In this section we compare our calculations to experimental results measured at GSI, Germany, and published in [118]. In this work, the experimental momentum distribution was adjusted assuming a Breit-Wigner shape for the resonance and the shape for the virtual state from [119]. From this analysis they concluded that the spectrum of ^{10}Li presented a p-wave resonance at $\sim$0.5 MeV and a virtual state with a scattering length of -20 to -30 fm. We note that in this fitting procedure the energy of the resonance, the scattering length of the virtual state and their weights are all independent parameters, as opposed to our method where the weight of each component is closely related to its energy.

For this calculation, the optical potentials between p and ^{11}Li and be-

tween p, n and ^{10}Li have been generated through the same method as the PH potentials in Sec. 4.2.1, through the folding of the Paris-Hamburg g-matrix effective interaction with the density of the nucleus computed from a Hartree-Fock calculation with the code OXBASH. Since ^{10}Li is unbound, we have opted to use the density of ^{9}Li instead. We note that the use of mean-field densities for the case of such exotic and light nuclei can be questionable. However, we have not found a better prescription to build the optical potentials for these cases, so we have kept to this one. The $p-n$ interaction is taken as Reid93, as in the other cases presented in this document.

The (p, pn) calculation has been computed for 20 to 30 $p-n$ bin states for each configuration of the final ^{10}Li, in order to produce the energy distribution. This means a large number of calculations has to be performed in order to produce the energy distribution. Therefore, in order to reduce computation time we have only computed the cross section leading to $p-n$ states with angular momentum and parity $j^\pi = 0^\pm, 1^\pm, 2^\pm$, which are the waves that contribute the most at the incident energy of 280 MeV/A. Some test calculations including higher j^π suggest that by this truncation we are underestimating the cross section by 10-15%. Since we are not interested in the magnitude of the cross section nor in "quenching factors" and noting that our choice of potentials may well induce larger uncertainties in the total cross section, we consider this precision to be enough. It can be questioned whether this approximation may alter the relative weights of different components of ^{10}Li. Test calculations indicate that the ratio between the contributions of different j^π is similar for different components of ^{10}Li. As such, the error induced by the truncation should affect all components of ^{10}Li similarly, not affecting their relative weights.

Now we present calculations for the different models for ^{10}Li presented in the previous section, and use the results in order to extract information on the structure of ^{10}Li. These results have been published in [120]

5.2.3.1 P3 and P4 models: No spin splitting, no d-wave

From the spectrum of [118], we try to build a ^{10}Li spectrum with a p-wave resonance at $E = 0.5$ MeV and a virtual state for the s-wave with a scattering length of -20 to -30 fm. Such a spectrum can be produced from potential P3 from Table 5.3. We therefore compute the energy distribution using TC

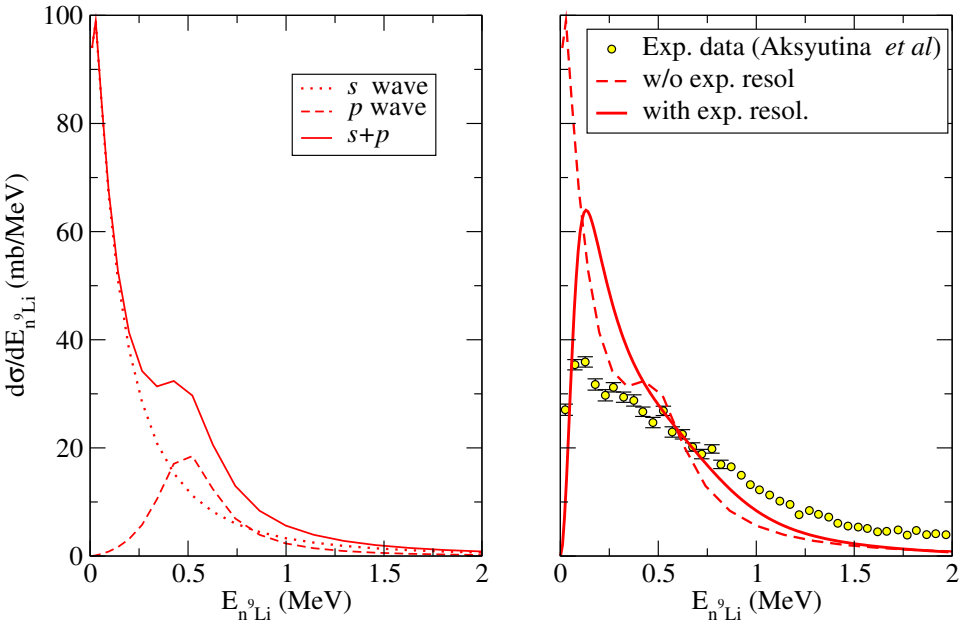

Figure 5.2: Energy distribution for ^{11}Li$(p, pn)^{10}$Li using potential P3 (see Table 5.3). The left panel shows the contribution of the s and p waves along with their sum. The right panel shows the full distribution before and after convoluting with the experimental resolution. Experimental data are from [118].

and present the results in Fig. 5.2.

Looking at the left panel of Fig. 5.2 it can be seen that the contribution of the s wave is concentrated at low energies, where it is markedly strong, presenting a behaviour consistent with a near-threshold virtual state. As for the p wave it shows a somewhat smaller contribution with the characteristic behaviour of a resonance at 0.5 MeV. In the right panel the strong distorting effect of the experimental resolution is apparent. It reduces strongly the low-energy contribution as well as smoothening out the features of the distribution. In particular, the peak of the resonance is barely visible due to the resolution. The theoretical prediction gives quite well the magnitude of the cross section, which is of 32 mb for the theoretical result and of 30 mb for the experimental data (between 0 and 2 MeV). This is rather surprising given the strong approximations used in its computation and the rather uninspired choice of potentials. However, the most interesting feature of the distribution, its shape, is not well reproduced, even having a ^{10}Li spectrum showing similar characteristics to those found in [118]: a p-wave resonance

at 0.5 MeV and a virtual state with scattering length $a \sim 20 - 30$ fm.

The reason for this discrepancy can be understood in the weights of the s and p waves. The s wave has a weight in the ground state of ^{11}Li of around 64%. Since its contribution seems to severely overestimate experimental data, we can conclude that this weight is too large, and that a better description of the ^{10}Li continuum should transfer part of it to the p wave. However, as we have mentioned in the previous section, the weight of each component is strongly correlated to the position in energy of the related structures (resonances and virtual states). As such, we cannot modify much the relative weight between the s and p waves without modifying the position of the virtual state and the resonance, thus separating our model from the experimental results established in [118].

Despite this caveat, we find illustrative to show the shape for a calculation in which the weight of the p-wave is markedly larger than that of the s-wave. This is achieved through potential P4, whose p-wave component has been increased to 67% at the cost of reducing the energy of the resonance to 0.23 MeV moving it farther from the value from [118]. The scattering length for the s wave virtual state has also been reduced, although it is still reasonably close to the results in [118]. The resulting energy distribution is shown in Fig. 5.3

As can be seen in Fig. 5.3 the modification in the spectrum of ^{10}Li has not helped improve the agreement with the experimental distribution. The s-wave contribution has indeed decreased reducing the contribution at low energies. However, in order to increase the contribution of the p wave, the resonance had to be shifted to lower energies, so our theoretical result keeps overestimating the distribution at low energies and underestimating it at higher energies.

From these tests we can conclude that we cannot modify much the relative weights of the s and p waves without distorting the positions of the resonance and virtual state beyond what is consistent with experimental data. Given that the agreement with experimental data is lacking, this indicates that the model we have been using for ^{10}Li (including only s and p wave states without coupling to the spin of ^{9}Li) is not enough to reproduce experimental data. In the following sections we present some extensions to the model to improve the agreement.

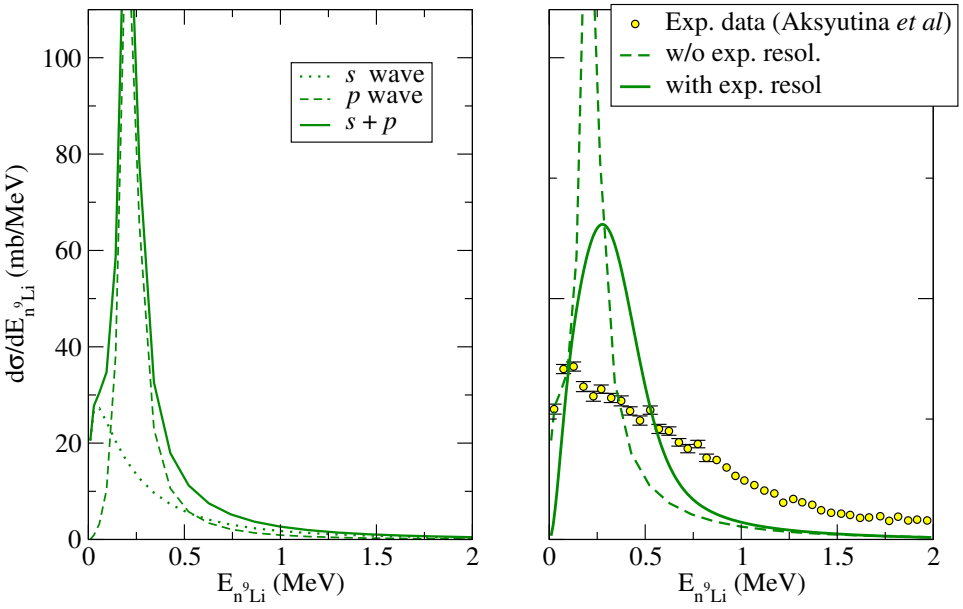

Figure 5.3: As Fig. 5.2, but showing the results for potential P4 (see Table 5.3).

5.2.3.2 P5 model: No spin splitting, d-wave

In the analysis of recent neutron removal experiments on ^{11}Li with a carbon target [121], the existence of a d-wave resonance at low energies ($\sim$ 1.5 MeV) has been suggested in order to reproduce experimental data. Such a resonance has not been considered in many other experiments on ^{10}Li, so its introduction can be contested.

However, it is interesting to check whether such a resonance can improve the agreement to experimental data so we have generated a calculation with potential P5, which shows a d-wave resonance at 1.5 MeV with a significant weight of the d wave in the ground state of ^{11}Li: 23%. The results of this calculation are presented in Fig. 5.4.

As can be seen in the figure, the inclusion of the d-wave resonance improves considerably the agreement with the experimental distribution. The reason for this improvement is twofold: first the appearance of a resonance at 1.5 MeV increases the cross section at high energies, which improves the agreement to experimental data in this region, where previous calculations were lacking. Secondly, as can be seen in Table 5.3, the weight of the d-wave in the ground state of ^{11}Li is drained almost exclusively from the s wave,

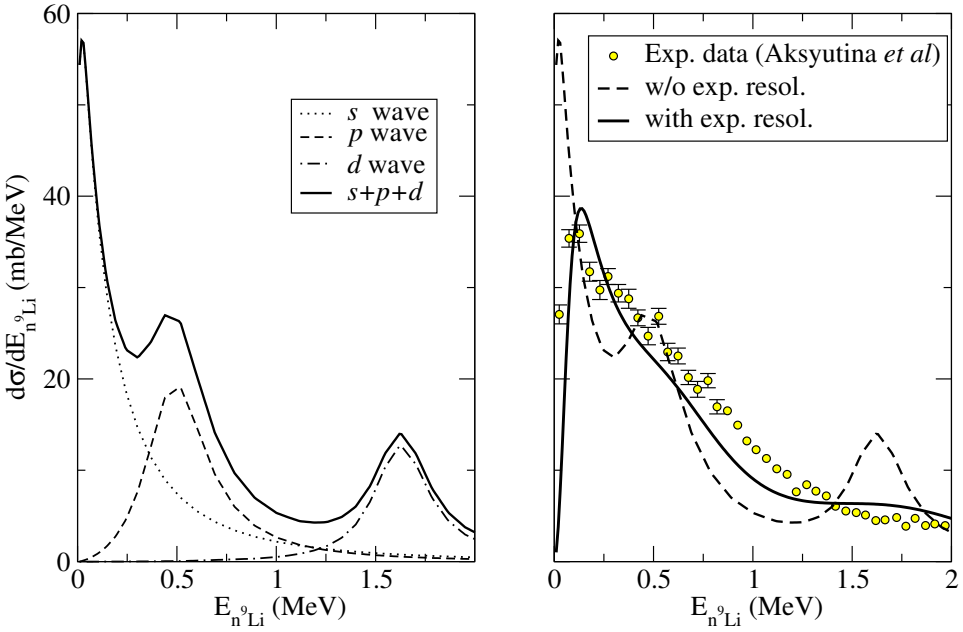

Figure 5.4: As Fig. 5.2, but showing the results for potential P5 (see Table 5.3).

which is left with a weight of 35%, around half that for P3. This reduces the contribution of the s wave, which is concentrated at low energies due to the virtual state, so the cross section at low energies decreases, approaching the experimental data.

Despite the sharp improvement in the agreement to experimental data, the lack of further support for the existence of a low-energy d-wave resonance makes us reluctant to accept this model of ^{10}Li. Therefore in the next section we will explore another model which does not include this resonance.

5.2.3.3 P1I model: Spin splitting, no d-wave

A feature of the ^{10}Li continuum that we have not included yet and that is widely accepted in the nuclear phsyics community, as opposed to a low-energy d-wave resonance, is the splitting of the structures of the continuum due to coupling to the spin of ^{9}Li ($3/2^-$). Such a splitting is present in many other nuclei and has been suggested as an explanation for the dispersion in the suggested values of the position of the p-wave resonance [104]. If such a resonance is split in two, some experiments could be sensitive to one of them, at a certain energy and others to the other one, at another energy.

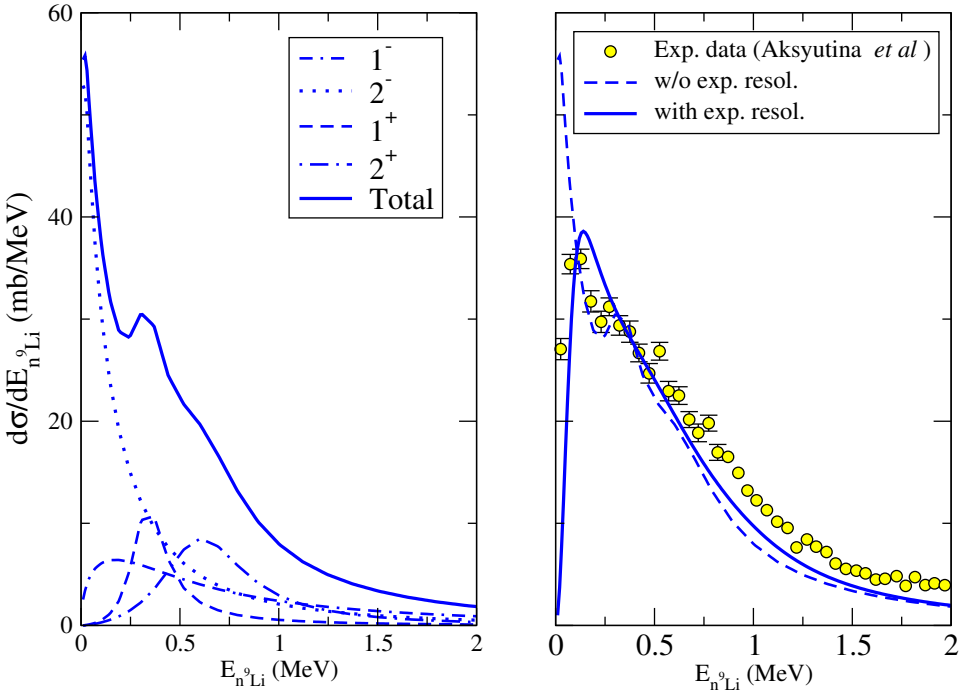

Figure 5.5: As Fig. 5.2, but showing the results for potential P1I (see Table 5.3). Due to splitting, the s wave gives 1^- and 2^- states for ^{10}Li, while the p wave gives 1^+ and 2^+ states.

Our P1I potential produces a spectrum with such a splitting, breaking the p-wave resonance in a 1^+ resonance at 0.37 MeV and a 2^+ resonance at 0.61 MeV. The virtual state is also broken in 1^- and 2^- components. In this case, the 1^- component loses its virtual state properties and results instead in a non-resonant continuum, while the scattering length of the 2^- state is increased to -37.9 fm. The weights in ^{11}Li ground state for the 1^-, 2^-, 1^+, 2^+ components are 27%, 40%, 12% and 19% respectively. The results of the calculations with P1I are presented in Fig. 5.5.

As can be seen in the figure the agreement with experimental data also improves considerably when considering the splitting of the states due to coupling with the spin of ^{9}Li. The low-energy contribution is reduced due to the splitting of the virtual state in the 2^- and 1^- components. Due to the non-resonant 1^- continuum, its contribution is effectively "lost", decreasing the effect of the virtual state. Moreover, the splitting of the $p-$wave resonance leads to an effectively broader resonance which tends to fill the high-energy tail of the distribution, thus improving the agreement for that area.

It can be questioned whether our results for P1I are compatible with the spectrum found in [118], that is, a resonance at 0.5 MeV and a scattering length of 20-30 fm. As for the resonance, an average of the resonance peak for 1^+ and 2^+ weighted by their contribution to the ground state of ^{11}Li (12% and 19% respectively) yields a centroid for the resonance of 0.52 MeV. Given that both resonances are not resolved due to the experimental resolution this result is compatible with a resonance at 0.5 MeV. As for the scattering length, we note that the square of the scattering length is proportional to the cross section at low energies $\sigma \propto a^2$ and that the cross section to the s wave can be expressed as the sum of the contributions of the 1^- and 2^- states, weighted by their contribution to the ^{11}Li ground state. Assuming that the proportionality between scattering length and cross section is the same for s wave, 1^- and 2^-, we can build an effective scattering length through:

$$a_{eff} = \frac{\sqrt{C_{1^-} a_{1^-}^2 + C_{2^-} a_{2^-}^2}}{C_{1^-} + C_{2^-}}, \tag{5.28}$$

with C_i being the weight of component i in the ground state of ^{11}Li. Assuming a scattering length $a_{1^-} = 0$ fm since it does not present a virtual state gives an effective scattering length $a_{eff} = -29.3$ fm which is rather consistent with our restraints over the scattering length.

In summary, applying our formalism we have found that we cannot describe the experimental data assuming just a p-wave resonance at 0.5 MeV and a virtual state with scattering length $a = -20 - 30$ fm, as was found in [118], because the weights we obtain for each contribution, which are not free parameters in our model, are incompatible with the experimental data. A remarkable improvement in the agreement with experimental data can be achieved either by the addition of a d-wave resonance at 1.5 MeV or the introduction of a spin-spin interaction which breaks the p-wave resonance in 1^+ and 2^- resonances at 0.37 and 0.61 MeV respectively, as well as giving an effective scattering length $a_{eff} = -29.3$ fm. From both modifications to the ^{10}Li continuum we favour the spin splitting because it is in better agreement with previous works on ^{10}Li. Let us remark the very important smearing effect of the experimental resolution, which makes two very different theoretical predictions, such as P5 and P1I, give very similar distributions after convolution with the resolution. Our calculations predict (p,pn) reactions

to be sensitive to both resonances in the case of spin splitting. As such, an experiment with better resolution, able to resolve both resonances, would prove of high spectroscopic value.

5.2.3.4 Distorting effects of the reaction mechanism

When extracting spectroscopic information from observables such as the energy distribution from a (p, pn) reaction, it is usual to assume a clear relation between the experimental distribution and the "real" spectrum of the nucleus. For example, a peak at a certain energy is usually assumed to indicate a resonance at that energy and the relative heights of different peaks are used to extract the relative strength of the associated components of the wave function.

In order to establish this relation, a main assumption is that the reaction mechanism is "transparent" to the nuclear structure, so that the results of the reaction are a mirror of the properties of the nucleus, perhaps with some overall kinematic factor accounting for conservation of energy and momentum.

This picture of the reaction mechanism is overly simplistic and known to fail to describe experimental observables at low energies, where the relatively long interaction time between projectile and target impedes a simple relation between the nuclear reaction predictions and the properties of the outgoing fragments of the reaction, whose properties and state of motion have undergone many changes ont their way out of the interaction area.

For high energies, it is expected that the experimental observables mirror closely the resonant structure of the unbound nucleus, without being affected much by the reaction mechanism, which would have a interaction time too short to distort the observables significantly. We have seen in Sec. 2.5.2 that absorption and distortion effects (associated to the reaction mechanism and not to the structure of the nucleus) tend to narrow significantly momentum distributions even at high energies, so the simplified picture we have described seems not to apply to them.

We are left to ponder how strong the effect of the reaction mechanism is in the energy distribution for (p, pN) reactions on Borromean nuclei and, therefore, how reliable the extraction of spectroscopic information is when extracted directly from experimental observables.

Since we have developed a full reaction formalism to describe (p,pn) reactions, we are in a position to study the effect of the reaction mechanism on the experimental energy distributions. To quantify these effects we will assume that the cross section for each value of q, the relative momentum between n and ^{9}Li, is proportional to the norm of the overlap:

$$\sigma_\alpha(q) \simeq C_\alpha \eta_\alpha(q) \qquad \eta_\alpha(q) = \int \mathrm{d}\mathbf{y}\, |\varphi_{AB,\alpha}(q,\mathbf{y})|^2 \,, \tag{5.29}$$

where all quantities take the definitions from Sec. 5.1. This approximation is not unlike the one where the spectroscopic factor is factored out from the cross section [Eq. (2.28)]. With this approximation, the total cross section can be expressed as:

$$\frac{\mathrm{d}\sigma}{\mathrm{d}\epsilon_{N_2C}} = 16\pi^2 \frac{\mu_{N_2C}}{\hbar^2 q} N_q \sum_\alpha C_\alpha \eta_\alpha(q). \tag{5.30}$$

In these expressions, we have intentionally omitted the dependence of C_α on q, because we will assume that C_α does not depend on the energy of the final ^{10}Li, since such a dependence would imply that the reaction would distort the structure energy distribution by favouring lower or higher energies. In Fig. (5.6) we compare the cross section obtained from Eq. (5.30) (dashed lines) with the full cross section from Eq. (5.25) (solid line). The factors C_α have been adjusted for each partial wave heuristically to give a good agreement with the full calculation.

We can see in the figure that the agreement between both equations is remarkably good, excellent for the p-wave components, although for the s-wave ones the full calculation is somewhat larger at lower energies than at higher energies when compared to the calculation from Eq. (5.30).

From these results we can interpret that the reaction behaves similarly for states of ^{10}Li with different energies. This is understandable by comparing the range of energies covered here (0-2 MeV) to the energy of the reaction (280 MeV/A). Clearly, the reaction will take place similarly when it provides 0.3 MeV to the ^{10}Li, yielding ^{10}Li in the breakup threshold and when it provides 2.3 MeV, yielding ^{10}Li with a relative energy of 2 MeV, since it has 280 MeV to spare. This result is also in agreement with the quasi-free picture of the (p,pn) reaction, in that the reaction is quite insensitive to the state of the ^{10}Li, being led by the interaction between the proton and the removed

nucleon.

We must note however that the C_α computed for the different waves differ rather strongly, by 27% for P3, when comparing the s and p waves and by 11% for P1I comparing the 2^- and 2^+ waves.

These rather large differences for the different waves make the use of a proper reaction formalism essential to extract quantitative spectroscopic information from the experimental momentum distribution, since it alters the relative weights of the different components in the nuclear structure spectrum and in the experimental distribution.

With all of these results in mind, a first-order computationally lighter method for studying these reactions without involving as many calculations as the full reaction calculation is suggested: Since the overall scaling factor C_α is fairly constant for all considered values of the $n-^9$Li energy, it is only necessary to compute the full cross section for one value of the energy (preferably one with high cross section). then the cross section is compared to η_α at that energy to obtain the factor C_α, which is then applied to the whole energy distribution. This process is repeated for all ^{10}Li configurations to account for the difference in C_α and allows to obtain energy distributions rather similar to those obtained for the full calculation, reducing the computation time in a factor of 20-30 (the number of energies required to produce a significant energy distribution). Since for the s wave states this method is expected to give a worse agreement, it could be considerd to skip this approximation completely or to perform calculations at low, mid and high energies to describe roughly the behaviour of factor C_α.

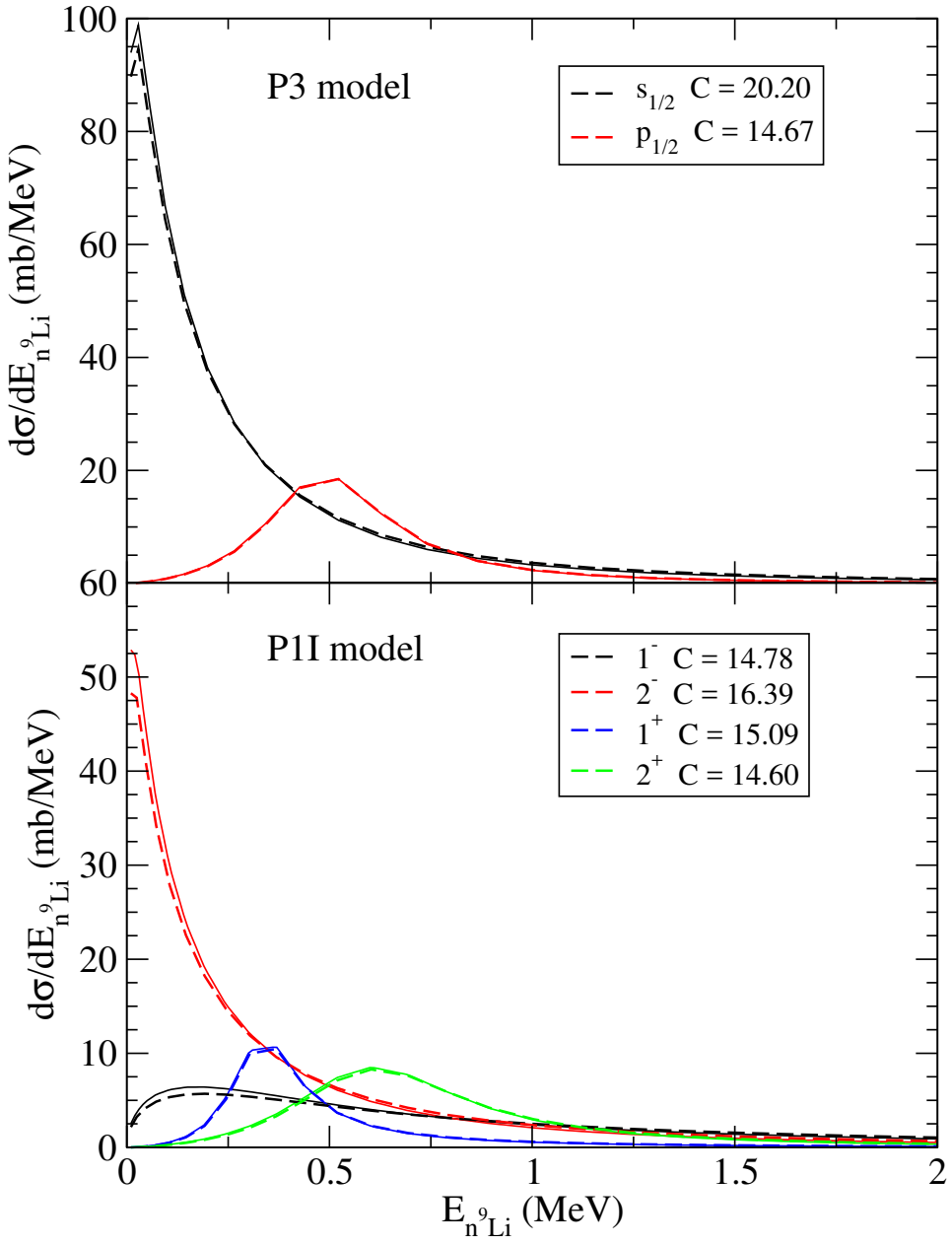

Figure 5.6: Energy distributions computed using Eq. 5.25 (solid lines) and Eq. 5.30 (dashed lines). The factors C_α are computed for each configuration of ^{10}Li independently. The top panel corresponds to calculations with potential P3 and the bottom one to potential P1I (See Table 5.3).

5.2.4 ^{11}Li$(p, d)^{10}$Li* @ 5.7 MeV/A

The $\langle ^{10}\text{Li}|^{11}\text{Li}\rangle$ overlaps are quantities resulting from a pure nuclear structure calculation. Therefore, they are not exclusive for a certain reaction. It is interesting then to check whether they can reproduce experimental data from other reactions which are sensitive to them.

To this respect, the reaction $^{11}\text{Li}(p, d)^{10}\text{Li}$ was measured recently in the IRIS facility at TRIUMF at a beam energy of 5.7 MeV/A [112]. There, they found a resonance at 0.62(4) MeV, which they associated to a $p_{1/2}$ state with a spectroscopic factor of 0.67(12) by comparing theoretical calculations to the angular differential cross section.

The theoretical calculation was performed using the DWBA formalism whose most questionable ingredient was the wavefunction for the transferred nucleon when bound to ^{11}Li. It was approximated by a Woods-Saxon potential with a rather conventional geometry ($r_0 = 1.15$ fm and $a = 0.6$ fm) whose depth was adjusted to give a $p_{1/2}$ eigenvalue at 0.98 MeV, the two-neutron separation energy plus the energy of the resonance.

The use of such a simple model for one of the valence neutrons of a Borromean system is rather doubtful, so we have performed a reanalysis of the experimental data using our $\langle ^{10}\text{Li}|^{11}\text{Li}\rangle$ overlaps, deeming them a more reliable description of the behaviour of the neutron in ^{11}Li.

As for the reaction calculation, we have opted to follow closely that of [112]. We have also performed a DWBA calculation using the same ingredients as those form [112]: The $p-n$ potential and the $p-^{11}$Li potentials were taken directly from [112] and the $d-^{10}$Be was fitted to the data on $d-^{11}$Li from [122], as theirs. The values of the potentials are presented in Table 5.4. A test has been made using Reid93 as V_{pn}, finding only small differences in the cross section. Therefore we have chosen to keep the prescription from [112] so that the only difference between their calculation and ours lies in the neutron wave function. The results of these calculations have been published in [123] and are shown in the following.

In order to study the sensitivity of the reaction to the models used we present calculations for potentials P1I, P2I, P3 and P4 (See Table 5.3). We have computed the cross section for 20 bins equispaced in momentum for a $n-^{9}$Li from 0 to 2 MeV for P3 and P4 and for 30 bins from 0 to 3 MeV for P1I and P2I, since they extend somewhat further in energy. Energy distributions

V	V_0	r_0	a_0	W_{0V}	r_{0V}	a_{0V}	W_{0s}	r_{0s}	a_{0s}	V_{so}	r_{so}	a_{so}
$p-^{11}$Li	95.93	1.00	1.10	15.00	0.65	0.50	11.90	0.67	1.1	10.70	0.80	0.75
$d-^{10}$Li	65.86	1.28	0.61	11.48	1.46	1.41	–	–	–	–	–	–
$p-n$	165.54	0.4	0.6	–	–	–	–	–	–	–	–	–

Table 5.4: Potentials used to compute ^{11}Li$(p, d)^{10}$Li. For the $d-^{10}$ potential, $A = 11$ has been used.

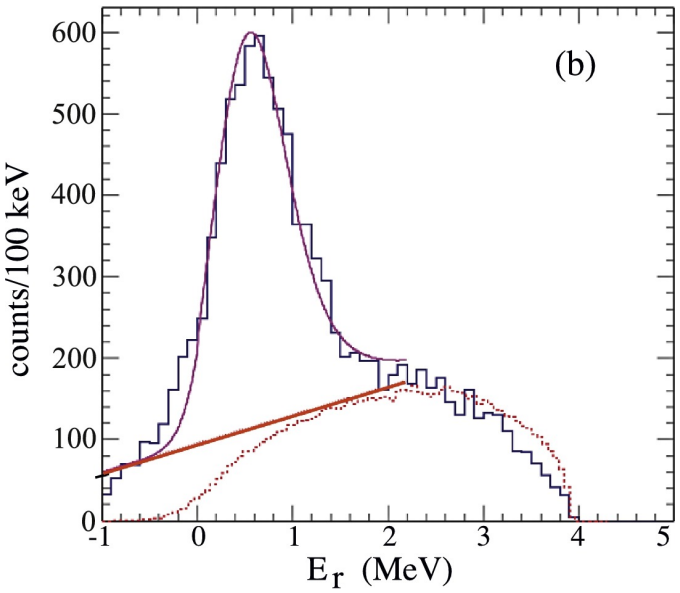

Figure 5.7: Resonance energy spectrum from [112]. The dotted red line denotes the calculated ^{9}Li$+n+d$ three-body non-resonant phasespace and the solid red line denotes the extracted background for the determination of the cross section.

for the four models are presented in Fig. 5.8, where the contribution of each ^{10}Li configuration is presented separately, as well as the total, which is also shown after convolution with the experimental resolution ($\sigma = 0.31$ MeV).

The strong effect of the experimental resolution is evident in the distributions. Despite the different shapes shown by the total energy distribution prior to the convolution with the experimental resolution, all of them result in a Gaussian shape with roughly the same width and centered in roughly the same position.

The comparison of Fig. 5.8 with Figs. 5.2, 5.3 and 5.5 shows that the transfer reaction seems to increase the contribution of the p-wave contributions with respect to the s-wave ones, when compared to the (p, pn) reaction,

as can be easily seen comparing the peaks of the p-wave resonances to the s-wave tails at their energy. This reinforces the importance of the description of the reaction mechanism when extracting spectroscopic information from experimental observables, as it makes it apparent how the same nuclear structure spectrum may be modified by different reactions.

In [112], an energy spectrum is presented, which is reproduced in Fig. 5.7. However, we refrain from comparing our distributions to this figure for two reasons. First, the energy distribution is given in counts instead of a cross section, so a comparison of magnitude is not possible. Second and more important is the fact that the distribution is presented without the background extracted.

The extraction of the background introduces a problem in our comparison to experiment. In [112], the background is extracted by fitting the energy distribution by a Breit-Wigner shape to describe the resonance and a linear function to describe the background. This marks the background as the events that do not fit a Breit-Wigner shape. However, the events forming the Breit-Wigner are not necessarily related to the p-wave resonance of ^{10}Li. As can be seen in Fig. 5.8, the rather broad experimental resolution mixes all contributions in an overall peak, making it very difficult to distinguish the resonant from the non-resonant continuum.

Moreover, the origin of the background events is not clear either, since they may come from the $^{11}\mathrm{Li}(p, d)^{10}\mathrm{Li}$ reaction leading to non-resonant states of the continuum of ^{10}Li or they may result from more complex processes between the four particles (p+n+n+^{9}Li) which end up producing outgoing deuteron and ^{9}Li, the two detected particles.

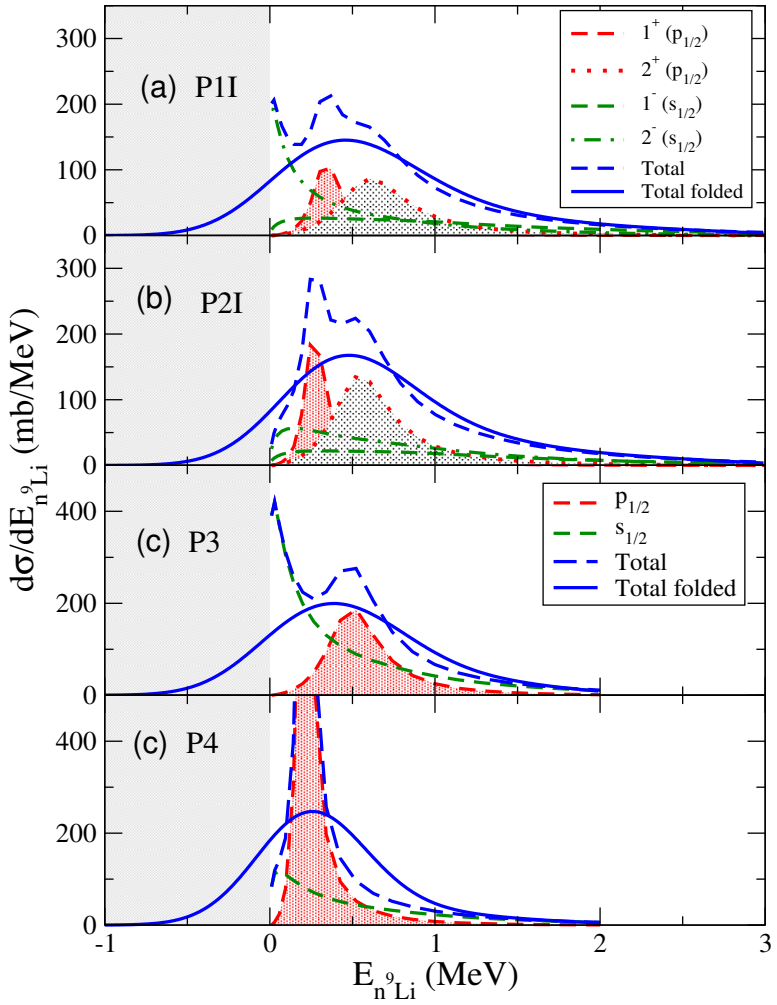

Figure 5.8: Energy distributions for the ^{11}Li$(p, d)^{10}$Li reaction obtained with models P1I, P2I, P3 and P4. The contribution of each ^{10}Li configuration is shown, as well as its sum. The sum is also shown convolved with the experimental resolution.

We have therefore to decide which events from our calculation contribute to the experimental cross section. We have considered only the contributions leading to p-wave configurations, taking the whole considered ^{10}Li energy interval, and leaving out the s-wave contribution. The reasoning behind this choice is that the shape for the s-wave contribution is certainly not Breit-Wigner-like and is therefore likely to be considered as background in the fitting procedure. Also, the whole p-wave spectrum for the energy $E_{n^9\mathrm{Li}} = 0 - 3$ MeV seems to be dominated by the resonances, and any non-resonant part will be rendered indistinguishable by the experimental resolution, thus the inclusion of the whole range seems the most adequate choice.

After these considerations we compare our theoretical angular differential cross section to the experimental angular differential cross section from [112] in Fig. 5.9. The theoretical cross section has been computed by integrating over $E_{n^9\mathrm{Li}}$ the double differential cross section on $E_{n^9\mathrm{Li}}$ and $\Omega_{c.m.}$, the center-of-mass angle of the outgoing deuteron, produced for the p-wave contributions. We note that no scaling factor is included in the calculations, which are compared directly to experimental data.

We find a good agreement in the shape of all contributions with that of the experimental data, corresponding to transfer from a p-wave. In magnitude, both P1I and P3 agree very well with experimental data, while P2I and P4 overestimate them. The blue dotted line shows the contribution of the s wave for P1I. Rather fortituously, its contribution is minimal at the angles where experimental data exist, although it would still be significant had we included it.

It is rather remarkable that two models as different as P1I and P3 give such a similar agreement with experimental data. Given the markedly different energy distributions presented by both models, we may conclude that the angular differential cross section for the reaction is not sensitive to the structure of ^{10}Li. We find that the angular cross section is only sensitive to the angular momentum of the transferred neutron in the resonant state and to the p-wave component of the ground state of ^{11}Li. Looking at Table 5.3, we can see that the p-wave accounts for 30% and 31% of the ground state for P1I and P3 respectively. These similar values of the p-wave content result in similar cross sections, which agree with experimental data and, in turn, the contents of 44% and 67% for P2I and P4 result in their overestimation of the experimental data.

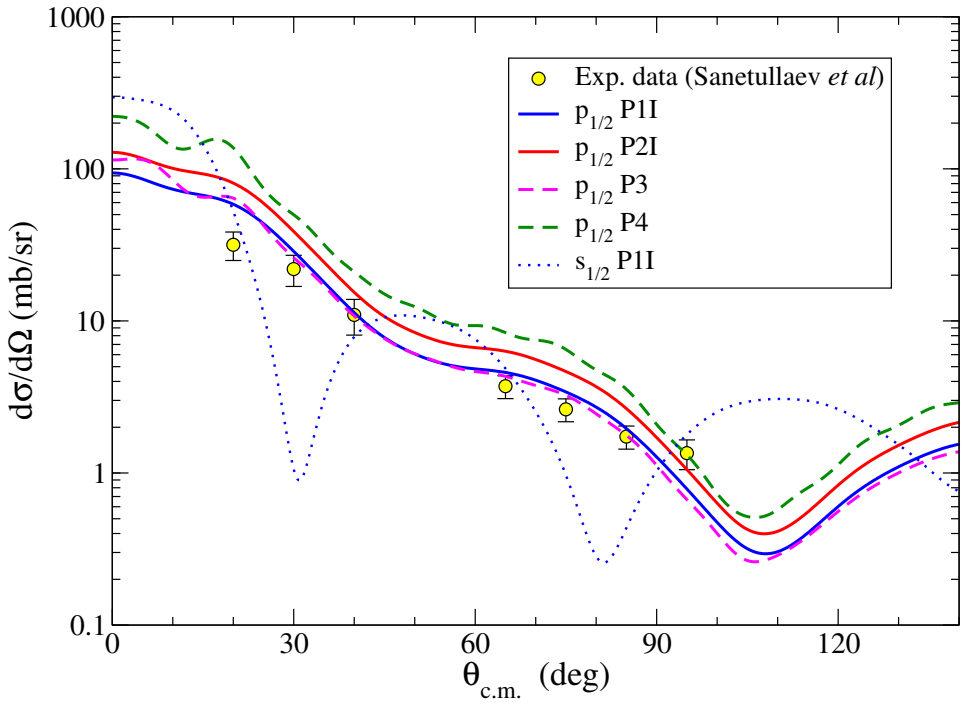

Figure 5.9: Angular differential cross section computed for ^{11}Li$(p,d)^{10}$Li. Experimental data are from [112]. Dashed lines denote calculations with models without coupling to the ^{9}Li spin while solid lines denote models including it. The contribution of the s wave components for P1I is shown in the blue dotted line.

From here we conclude that the experimental data from [112] agree well with models giving a p-wave component of ∼30%, and are rather independent from other features of the model. As a test of this assertion, in Fig. 5.10, the calculation for P5 (which was produced after the present work on transfer reactions was developed and published) are shown. P5 has a p-wave component of 35%, so it is expected to show a good agreement with experimental data, as can be seen in the figure. We must also note that, since ^{11}Li has two valence neutrons, an occupation of ∼30% corresponds to a spectroscopic factor of 0.6, fully consistent with that found in [112].

To finish this chapter let us remark that our models P1I and P5 are able to reproduce two different reactions (^{11}Li(p,pn) and ^{11}Li(p,d)) at very different incident energies (280 MeV/A and 5.7 MeV/A), which are sensitive to different features of our models. From these two models, we favour model P1I over P5, because the d-wave resonance presented by the latter has only

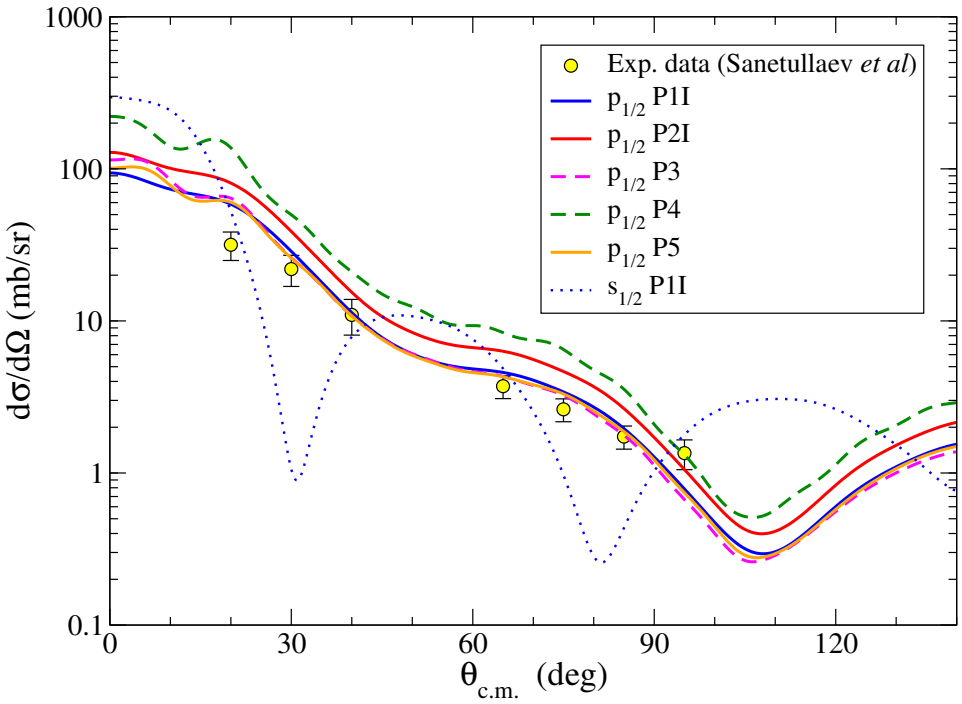

Figure 5.10: As Fig. 5.9 including the calculation for P5.

been reported by the analysis of one experiment, while the former presents splitting of the spectrum due to coupling to the spin of ^{9}Li, a feature which, despite not having been confirmed experimentally due to poor experimental resolution, is widely accepted in the relevant literature.

Chapter 6

Summary and conclusions

And here, poor fool! with all my lore
I stand no wiser than before

Faust, Johann Wolfgang von Goethe

In this work, a new reaction formalism has been developed for the study of (p, pn) and $(p, 2p)$ nucleon knockout reactions at intermediate and high energies. This formalism, referred to as Transfer to the Continuum, is based on the prior representation of the matrix element for the (p, pN) process, so that the main interaction leading the reaction is that between the incoming proton and the removed nucleon, consistently with the quasi-free picture of (p, pN) reactions, which relates them to the free scattering between the incoming proton and the removed nucleon.

The Transfer to the Continuum formalism does not explicitly assume the Impulse Approximation nor the factorization approximation, as the widely-used Distorted-Wave Impulse Approximation (DWIA) formalism and, as such, is applicable at lower energies.

For the larger energies considered in this work ($\sim 200 - 400$ MeV), relativistic kinematics must be taken into account, although the use of the Schrödinger equation is still well-founded, including the proper modifications to account for relativistic kinematics. These modifications yield an increase in the cross section of around $1-3\%$ at energies of 100 MeV/A and of $30-45\%$ at 400 MeV/A. As such, their inclusion is essential for the description of experimental data.

The main observables of interest in this work are the total integrated

cross sections and the momentum distributions. The latter present a shape which is heavily dependent on the quantum numbers of the removed nucleon, most notably the orbital angular momentum. As such, they are valuable in spectroscopic studies. However, they are modified by distortion and absorption effects, so a proper reaction formalism is required to extract reliable information from them.

In order to test the Transfer to the Continuum formalism, benchmark calculations have been performed comparing with other theories for the study of (p, pN) nuclear reactions: the Distorted-Wave Impulse Approximation (DWIA) and the Faddeev/AGS equations.

The comparison with DWIA was analysed for the ^{15}C$(p, pn)^{14}$C reaction at 420 MeV/A [49], finding an excellent agreement between both formalisms, both in shape and magnitude. The comparison was tested for different separation energies of the removed neutron: 1.22, 5 and 18 MeV, finding a similar degree of agreement for all these cases. Since in the Transfer to the Continuum the dependence of the optical potentials with the nucleon-nucleus energy is not considered but in DWIA it can be included, the effect of this energy dependence has been studied, finding it to be relatively small,with a slight broadening of the distributions without a change in the total cross section. This validates the use of energy-independent optical potentials employed by the Transfer to the Continuum for the study of (p, pN) reactions. A comparison with published Faddeev/AGS momentum distributions for this reaction [57] also gives an excellent agreement, once relativistic effects have been ignored.

Benchmark calculations with Faddeev/AGS were performed for the ^{11}Be$(p, pn)^{10}$Be reaction at 200 MeV/A, ignoring relativistic effects, since the Faddeev/AGS code used did not include them. The dependence of the benchmark on the angular momentum of the removed nucleon was studied by computing the cross sections for the removal of the neutron from a $2s_{1/2}$ and a $1p_{1/2}$ orbital. Two proton-neutron interactions have been used in the benchmark calculations, namely a simple Gaussian central interaction and the more realistic Reid93 interaction [74]. Using the Gaussian interaction, modified to better reproduce the phaseshifts for odd parity waves, yielded an excellent agreement between Faddeev/AGS and Transfer to the Continuum, with differences in the cross section of 5-6%, which are barely noticeable in the momentum distributions. The use of the Reid93 interaction for the

proton-neutron potential yielded larger differences, of 8-9%. The origin for these larger discrepancies is not clear to us yet. In order to understand their origin we have performed a plane-wave calculation which yields a much reduced discrepancy, of less than 1%. This indicates that the origin of the discrepancy is not simply the proton-neutron interaction, but rather its influence in the calculation. In particular, the steeper nature of the Reid93 interaction may make it more difficult for both formalisms to describe similarly the $p-^{11}$Be interaction, since the Transfer to the Continuum uses relatively smooth interactions for it, while for the Faddeev/AGS formalism, it appears as a complicated composition of the binary interactions between p and n, p and ^{10}Be and n and ^{10}Be. Given the steep and l-dependent nature of the Reid93 interaction, the result of this composition is unlikely to be well described by a smooth l-independent potential.

Since the Transfer to the Continuum formalism does not consider the impulse approximation nor the factorization approximation used by DWIA, it is applicable at lower energies than it. As a test to its adequateness at these lower energies, we have reanalysed experimental results from $^{18}\mathrm{C}(p,pn)^{17}\mathrm{C}^{*}$ at 81 MeV/A. The reanalysis gives a good description of the momentum distributions for the reaction leading to the excited states at E_x =0.21 MeV and E_x =0.33 MeV (the cross section to the ground state was too small to extract an adequate momentum distribution) when considering a neutron removed from $2s_{1/2}$ and $1d_{5/2}$ orbitals respectively. The "quenching factors" found using the Transfer to the Continuum for both states were somewhat larger and similar between themselves than those reported by a previous analysis using CDCC. The most interesting result from this reanalysis was a sizeable cross section for the (p,d) transfer reaction, which accounted for $\sim$15% of the total (p,pn) cross section for the E_x = 0.33 MeV state. This result was verified using conventional DWBA calculations. Given that in the experiment only the residual core was detected, the transfer reaction contributes to the experimental cross section. As such, for similar reactions the use of reaction formalisms that do not treat the transfer channel explicitly, such as CDCC, should be discouraged in favour of models which consider it, such as Transfer to the Continuum, or at least, the relevance of the reaction channel should be checked through DWBA calculations prior to the use of such formalisms.

The reaction $^{20}\mathrm{C}(p,pn)^{19}\mathrm{C}$ at 40 MeV/A incident energy has also been

studied, lending support to the models of ^{19}C which do not show a bound $5/2^+$ state, since its inclusion leads to a severe overestimation of the cross section. This result must be taken just as an indication rather than as solid evidence due to the lack of a trustworthy model for ^{19}C.

The open problem of the dependence of "quenching" on the isospin asymmetry of nuclei has been tackled with the Transfer to the Continuum formalism. We have computed the "quenching factors" for all the $(p, 2p)$ and (p, pn) reactions published by the R^3B collaboration at GSI, Germany up to the date of composition of this document [23, 42, 43], and have studied their dependence on $\Delta S = S_{p(n)} - S_{n(p)}$, the difference between the binding energy of the proton and neutron for $(p, 2p)$ reaction and between neutron and proton in (p, pn) reactions. The sensitivity of the results to the optical potentials used in the calculation has been studied by employing two different potential parametrizations. As a test of the adequateness of the formalism, we have computed momentum distributions and compared them to published results. In general, the agreement is good and rather independent of the binding energy of the removed nucleon, with our theoretical results being somewhat narrower than the experimental distributions and showing little dependence on the potential parametrizations used.

For both parametrizations, a small dependence has been found of the "quenching factors" on ΔS. This small dependence is in agreement with the results found for transfer reactions [10, 33, 37] and recent analysis of exclusive $(p, 2p)$ reactions measured at RIKEN (Japan) [44]. It is however at odds with the trend found for nucleon knockout reactions with heavy targets at intermediate energies, which showed a marked dependence of the "quenching factors" on ΔS [31, 32]. The overall "quenching factor" for the reactions is $R_s = 0.7 - 0.77$, which is in reasonable agreement with other analysis, though perhaps somewhat larger than the mean "quenching factor" found in the literature.

The "quenching factors" found for both potential parametrizations are very similar when considering reactions where a weakly-bound nucleon is removed. However, for more deeply-bound nucleons the "quenching factors" are more dependent on the optical potentials used. This results in dependencies on ΔS which are slightly different for both potential parametrizations, although they are both markedly weaker than the dependence shown by mid-energy nucleon knockout data. The origin of these difference arises from the

reactions for deeply-bound nucleons being more sensitive to deeper parts of the wavefunction, where the potentials show larger differences and are not well constrained. The extraction of elastic scattering data for the measured reactions could prove useful in order to constrain the optical potential used for their analysis, although it could prove to be insufficient, since elastic scattering is more peripheral than (p, pn) and $(p, 2p)$ reactions, specially for deeply-bound nucleons.

The reactions for nuclei which are well described by the Independent Particle Model have been studied using the eikonal version of the DWIA formalism [23], with reported results which are consistent with those presented here, finding a small dependence of the "quenching factors" on ΔS with an overall value of 0.66, which is somewhat smaller than the results presented here. The "quenching factors" for particular reactions show a greater agreement between our results and theirs for removal of weakly-bound nucleons and larger differences for deeply-bound nucleons. This points to the origin of the difference being the optical potentials used in the calculations.

Other analysis for (p, pn) and $(p, 2p)$ reactions on ^{22,23}O and ^{21}N, "quenching factors" have been published using the Faddeev/AGS formalism [43]. These "quenching factors" present a larger dependence on ΔS and are quite smaller than ours for these reactions. We obtained a greater agreement with these results using similar inputs to theirs in our calculations. However, these calculations were non-relativistic and used potentials which in our opinion do not have enough absorption for the energies of the reactions. As such we consider that our previous calculations, including relativistic kinematics and stronger absorption, give more realistic quenching. With these considerations we manage to obtain a consistent description of all of the reactions published by the R^3B collaboration, solving the discrepancies between the different results published by the collaboration.

The agreement between our results with Transfer to the Continuum, and those from eikonal DWIA must be remarked, since the approximations assumed by both formalisms are rather different, so their agreement is mutually validating. This is specially relevant given the discrepancy of the trend found and that for mid-energy heavy-target knockout reactions, which may shed doubts on the reaction model used to describe (p, pN) or heavy-target knockout reactions. In this dichotomy, the fact that two reaction formalisms starting from different assumptions give similar conclusions is a strong argu-

ment in favour of their description of the reaction, and poses doubts on the description of heavy-ion knockout, which leads to a different dependence on isospin asymmetry.

In the next section of this work, we have extended our reaction formalism to include (p, pN) reactions to the case of Borromean nuclei. Given their Borromean nature, (p, pN) reactions lead to an unbound residual core whose spectrum can be studied by measuring the energy distribution from the reaction. This energy distribution can be computed using the Transfer to the Continuum formalism and a three-body description of the Borromean nucleus, leading to a parameter-free description of the energy distribution. This is a great improvement over the traditional treatment of (p, pN) reactions on Borromean nuclei, which relies on an R-matrix fitting of the energy distribution. One fundamental element included by our treatment of the reaction which was missing on previous descriptions is the consistency between the two-body spectrum and the description of the three-body bound nucleus, which is perhaps most evident in the relation between the position of the resonances and their relative weight. It also provides a prediction for the absolute value of the cross section.

The formalism has been applied to the $^{11}\mathrm{Li}(p, pn)^{10}\mathrm{Li}$ reaction, which was recently measured at an energy of 280 MeV/A. Our analysis shows that the previous description of the energy distribution including just a p-wave resonance at 0.5 MeV and a s-wave virtual state with a scattering length of $a = 20 - 30$ fm is not enough, since the weight of the s-wave virtual state is underestimated by the R-matrix fitting, and leads to too large a contribution when considering a realistic weight for it. As such, the model was extended in two ways that led to an improved description of the experimental energy distribution.

The first of these extensions is the inclusion of a d-wave resonance at 1.5 MeV, which has been suggested by some experiments but discarded by other. This model presents a reduced weight of the s-wave, thus improving the agreement with experimental data. The second includes spin-spin interactions which split the resonance and virtual state leading to a better description with the data. Although no experimental data has yet conclusively confirmed this splitting, it is theoretically expected and widely accepted.

We have also studied the distorting effect of the reaction on the energy

distribution, finding that the shape of the energy distribution is not affected much by the reaction and mirrors that obtained from three-body nuclear structure calculations for the different configurations. However, different configurations are differently enhanced and suppressed by the reaction, so, in order to have precise spectroscopic information a reliable reaction formalism is required to provide scaling factors between experimental data and nuclear structure calculations.

Both models for ^{11}Li and ^{10}Li have also been used in the description of the $^{11}\mathrm{Li}(p,d)^{10}\mathrm{Li}$ reaction at 5.7 MeV/A, showing great success in the reproduction of the angular distribution without the need of rescaling factors. This success stems from the transfer reaction being sensitive mostly to the weight of the $p-$wave in the ground state of ^{11}Li which is of $\sim$30% in both models, despite their markedly different nature. As such, we have produced two models for ^{11}Li and ^{10}Li which present the outstanding success of reproducing experimental results for two different reactions at very different energies: $^{11}\mathrm{Li}(p,pn)^{10}\mathrm{Li}$ at 280 MeV/A and $^{11}\mathrm{Li}(p,d)^{10}\mathrm{Li}$ at 5.7 MeV/A. From them, we favour that with spin splitting over that with the d-wave resonance, because the latter is rather disputed in the literature on ^{10}Li, although the experimental data considered here cannot distinguish between them.

In conclusion, the Transfer to the Continuum formalism has been developed and implemented to study (p,pn) and $(p,2p)$ reactions at intermediate and high energies. It has been benchmarked to other reaction formalisms, finding encouraging agreement. A systematic study of recently published (p,pn) and $(p,2p)$ reactions using the Transfer to the Continuum formalism has shown a small dependence of the "quenching factors" on isospin asymmetry, thus providing a solid answer to this open problem. The Transfer to the Continuum formalism has also been extended to study the energy distributions resulting from (p,pn) and $(p,2p)$ reactions on Borromean nuclei. This extended formalism has been applied to the $^{11}\mathrm{Li}(p,pn)^{10}\mathrm{Li}$ reaction, showing that the description of the experimental distribution requires either the inclusion of a low-energy d-wave resonance or the splitting of the resonance and virtual state through interaction with the ^{9}Li spin.

Further extensions of the present work include its application to other (p,pn) and $(p,2p)$ data in order to build a stronger systematics to verify the small asymmetry dependence of the "quenching factors", as well as the study

of other Borromean nuclei, such as ^{14}Be and ^{17}Ne, for which experimental data exist. For the analysis of reaction with Borromean nuclei, the study of other observables, such as momentum distributions or proton-core angular correlations, can provide further constrains on the nuclear models used to describe them.

Appendix A

Details on the calculations for R^3B data

This Appendix supplements the information provided in Sec. 4.2. In Tab. A.1, the states of the residual core considered in the calculation of the cross section are presented along with the orbital from which the nucleon is extracted and the corresponding spectroscopic factor (multiplied by a factor $(A/(A-1))^N$) and the theoretical energy of the state. The two latter quantities were obtained from shell-model calculations using the WBT [15] interaction. When experimental data exist, the experimental energy of the associated state is presented for comparison. Finally the reduced radius r_0 used in the Woods-Saxon potential which generates the bound state is presented. Since the radius only depends on the orbital of the removed nucleon, it is not repeated when the orbital appears multiple times. In general, we have only considered configurations whose spectroscopic factor was greater than 0.1 and which lie under the the neutron and proton emission threshold. When there are states that are unbound theoretically and bound experimentally or vice versa, we have opted to include or exclude them based on the experimental spectrum, although an exception has been made for the $^{23}\mathrm{O}(p,2p)^{22}\mathrm{N}$ case, where a high-lying 2^- state has been excluded, as in [43].

Table A.1: Detailed information on the levels considered in Sec. 4.2. The first column denotes the reaction considered. The second indicates the angular momentum and parity of the residual core, while the third indicates the orbital from which the nucleon is removed. The fourth column shows the spectroscopic factor associated to that state, with the factor $(A/(A-1))^N$ already multiplied. The fifth and sixth show the theoretical and experimental (when available) excitation energy of the state respectively. Finally the seventh column shows the reduced radius used in the computation of the bound state wavefunction.

Reaction	I^π	$n\ell j$	C^2S	E_{th}	E_{exp}	r_0
^{13}O$(p,2p)^{12}$N	1^+	$1p_{1/2}$	0.66	0	0	1.214
^{14}O$(p,2p)^{13}$N	$1/2^-$	$1p_{1/2}$	1.97	0	0	1.258
^{15}O$(p,2p)^{14}$N	1^+	$1p_{1/2}$	1.31	0	0	1.305
	1^+	$1p_{1/2}$	0.29	4.112	3.948	
	1^+	$1p_{3/2}$	0.60	4.112	3.948	1.280
	2^+	$1p_{3/2}$	1.34	6.831	7.029	
^{16}O$(p,2p)^{15}$N	$1/2^-$	$1p_{1/2}$	2.00	0	0	1.335
	$3/2^-$	$1p_{3/2}$	4.09	5.725	6.323	1.316
^{17}O$(p,2p)^{16}$N	2^-	$1p_{1/2}$	0.87	0.049	0	1.351
	3^-	$1p_{1/2}$	1.20	0.541	0.298	
^{18}O$(p,2p)^{17}$N	$1/2^-$	$1p_{1/2}$	2.00	0	0	1.362
	$3/2^-$	$1p_{3/2}$	0.27	1.941	1.373	1.346
	$3/2^-$	$1p_{3/2}$	0.27	4.097	3.906	
	$3/2^-$	$1p_{3/2}$	2.87	6.244	5.515	
^{21}O$(p,2p)^{20}$N	2^-	$1p_{1/2}$	0.77	0		1.376
	3^-	$1p_{1/2}$	1.11	0.932		
^{21}N$(p,2p)^{20}$C	0^+	$1p_{1/2}$	0.72	0		1.387
	2^+	$1p_{3/2}$	0.33	2.177		1.371
^{21}N$(p,pn)^{20}$N	2^-	$1d_{5/2}$	1.97	0		1.145
	0^-	$2s_{1/2}$	0.16	0.584		0.973
	1^-	$2s_{1/2}$	0.49	1.140		
	3^-	$1d_{5/2}$	2.98	0.932		
^{22}O$(p,2p)^{21}$N	$1/2^-$	$1p_{1/2}$	1.87	0	0	1.375
	$3/2^-$	$1p_{3/2}$	0.73	1.861	1.160	1.375

Reaction	I^π	$n\ell j$	C^2S	E_{th}(MeV)	E_{exp}(MeV)	r_0(fm)
^{22}O$(p,pn)^{21}$O	$5/2^+$	$1d_{5/2}$	5.73	0	0	1.173
	$1/2^+$	$2s_{1/2}$	0.25	1.331	1.220	1.001
	$5/2^+$	$1d_{5/2}$	0.16	3.149	3.073	
^{23}O$(p,2p)^{22}$N	0^-	$1p_{1/2}$	0.51	0	0	1.392
	1^-	$1p_{1/2}$	1.49	0.76	0.183	
^{23}O$(p,pn)^{22}$O	0^+	$2s_{1/2}$	0.87	0	0	1.013
	2^+	$1d_{5/2}$	2.27	3.374	3.199	1.182
	3^+	$1d_{5/2}$	3.37	4.829	4.584	
	0^+	$2s_{1/2}$	0.13	4.614	4.909	
	1^-	$1p_{1/2}$	0.81	5.808	5.800	1.239
	0^-	$1p_{1/2}$	0.34	6.059		
	2^+	$1d_{5/2}$	0.26	6.503	6.512	
^{12}C$(p,2p)^{11}$B	$3/2^-$	$1p_{3/2}$	3.49	0	0	1.236
	$1/2^-$	$1p_{1/2}$	0.63	1.938	2.125	1.245
	$3/2^-$	$1p_{3/2}$	0.16	4.288	5.020	

In Table A.2, more detailed information on the computed cross section is presented than in Table 4.4, with the cross sections for each level of the residual core detailed along with the corresponding spectroscopic factor.

Table A.2: Detailed information on the calculation of the cross sections in Sec. 4.2. The first column denotes the reaction considered. The second indicates the angular momentum and parity of the residual core, while the third indicates the orbital from which the nucleon is removed. The fourth column shows the spectroscopic factor associated to that state, with the factor $(A/(A-1))^N$ already multiplied. The fifth, sixth and seventh columns correspond to the single particle, theoretical $\sigma_{th} = C^2S\sigma_{s.p.}$ and experimental cross sections respectively, with the top value resulting from a calculation with Dirac potentials and the lower one to a calculation with PH potentials (See Sec. 4.2.1). Finally the eighth column correspond to the "quenching factor" R_s. Asterisks in $\sigma_{s.p.}$ indicate that it has been taken from other state from the same nucleus.

Reaction	I^π	$n\ell j$	C^2S	$\sigma_{\rm sp}$	$\sigma_{\rm th}$	$\sigma_{\rm exp}$	R_s
^{13}O$(p,2p)$	1^+	$1p_{1/2}$	0.66	10.562	6.975	5.78(0.91)[0.37]	0.829
				10.813	7.140		0.809

Reaction	I^π	$n\ell j$	C^2S	$\sigma_{\rm sp}$	$\sigma_{\rm th}$	$\sigma_{\rm exp}$	R_s
^{14}O$(p,2p)$	$1/2^-$	$1p_{1/2}$	1.97	8.509	16.769	10.23(0.80)[0.65]	0.610
				8.065	15.895		0.644
^{15}O$(p,2p)$	1^+	$1p_{1/2}$	1.31	7.487	9.780	18.92(1.82)[1.20]	0.761
				6.562	8.571		0.881
	1^+	$1p_{1/2}$	0.29	6.771	1.959		
				5.829	1.686		
	1^+	$1p_{3/2}$	0.60	7.044	4.246		
				6.047	3.645		
	2^+	$1p_{3/2}$	1.34	6.624	8.872		
				5.658	7.578		
^{16}O$(p,2p)$	$1/2^-$	$1p_{1/2}$	2.00	6.355	12.710	26.84(0.90)[1.70]	0.739
				5.997	11.994		0.783
	$3/2^-$	$1p_{3/2}$	4.09	5.773	23.598		
				5.452	22.285		
^{17}O$(p,2p)$	2^-	$1p_{1/2}$	0.87	5.777	4.996	7.90(0.26)[0.50]	0.661
				5.064	4.380		0.754
	3^-	$1p_{1/2}$	1.20	5.777*	6.948		
				5.064*	6.091		
^{18}O$(p,2p)$	$1/2^-$	$1p_{1/2}$	2.00	5.165	10.313	17.80(1.04)[1.13]	0.652
				4.312	8.611		0.785
	$3/2^-$	$1p_{3/2}$	0.27	5.296	1.430		
				4.413	1.191		
	$3/2^-$	$1p_{3/2}$	0.27	5.296*	1.407		
				4.413*	1.173		
	$3/2^-$	$1p_{3/2}$	2.87	4.924	14.123		
				4.083	11.710		
^{21}O$(p,2p)$	2^-	$1p_{1/2}$	0.77	4.008	3.082	5.31(0.23)[0.34]	0.705
				3.493	2.686		0.809
	3^-	$1p_{1/2}$	1.11	4.008*	4.450		
				3.493*	3.879		
^{21}N$(p,2p)$	0^+	$1p_{1/2}$	0.72	4.104	2.939	2.27(0.34)	0.529
				3.388	2.426		0.641
	2^+	$1p_{1/2}$	0.33	4.149	1.351		
				3.421	1.113		

Reaction	I^π	$n\ell j$	C^2S	$\sigma_{\rm sp}$	$\sigma_{\rm th}$	$\sigma_{\rm exp}$	R_s
^{21}N(p,pn)	2^-	$1d_{5/2}$	1.97	9.896	19.486	48.52(4.04)	0.862
				10.658	20.987		
	0^-	$2s_{1/2}$	0.16	11.301	1.761		
				11.960	1.863		0.802
	1^-	$2s_{1/2}$	0.49	11.301*	5.557		
				11.960*	5.881		
	3^-	$1d_{5/2}$	2.98	9.896*	29.470		
				10.658*	31.739		
^{22}O$(p,2p)$	$1/2^-$	$1p_{1/2}$	1.87	3.497	6.524	6.01(0.41)	0.646
				2.932	5.471		0.771
	$3/2^-$	$1p_{3/2}$	0.73	3.625	2.651		
				3.039	2.222		
^{22}O(p,pn)	$5/2^+$	$1d_{5/2}$	5.73	8.680	49.733	39.24(2.34)	0.736
				8.112	46.484		0.787
	$1/2^+$	$2s_{1/2}$	0.25	8.925	2.253		
				8.348	2.107		
	$5/2^+$	$1d_{5/2}$	0.16	8.680*	1.389		
				8.112*	1.298		
^{23}O$(p,2p)$	0^-	$1p_{1/2}$	0.51	3.302	1.667	4.93(0.96)	0.762
				2.844	1.436		0.885
	1^-	$1p_{1/2}$	1.49	3.302*	4.909		
				2.844*	4.227		

Reaction	I^π	$n\ell j$	C^2S	$\sigma_{\rm sp}$	$\sigma_{\rm th}$	$\sigma_{\rm exp}$	R_s
^{23}O(p,pn)	0^+	$2s_{1/2}$	0.87	13.841	12.042	54.0(10.8)	0.766
				13.379	11.640		0.787
	2^+	$1d_{5/2}$	2.27	8.419	19.103		
				8.207	18.621		
	3^+	$1d_{5/2}$	3.37	8.419*	28.342		
				8.207*	27.626		
	0^+	$2s_{1/2}$	0.13	13.841*	1.815		
				13.379*	1.755		
	1^-	$1p_{1/2}$	0.81	6.106	4.947		
				5.999	4.861		
	0^-	$1p_{1/2}$	0.34	6.106*	2.043		
				5.999*	2.007		
	2^+	$1d_{5/2}$	0.26	8.419*	2.181		
				8.207*	2.126		
^{12}C$(p,2p)$	$3/2^-$	$1p_{3/2}$	3.49	6.205	21.654	19.2(1.8)[1.2]	0.730
				6.557	22.883		0.690
	$1/2^-$	$1p_{1/2}$	0.63	5.785	3.629		
				6.155	3.861		
	$3/2^-$	$1p_{3/2}$	0.16	6.205*	1.015		
				6.544*	1.073		

Appendix B

Relativistic kinematics

In this appendix, formulae for the relativistic treatment of the kinematics of nuclear reactions are presented, focusing on the quantities required for the development of the Transfer to the Continuum formalism, detailed in Chapter 2.

We will start from a proton with mass m_p impinging with a kinetic energy T_{LAB} on a target with mass m_A at rest. The target A is composed of a nucleon with mass m_N and a core with mass m_C, bound through a binding energy S_n. We will consider the final state leading to an outgoing core and $p-N$ system, with a relative energy between proton and nucleon e_{pN}. We will assume a system of units with $c = 1$ to simplify the notation. As such, we first note

$$m_A = m_N + m_C - S_n, \tag{B.1}$$

through conservation of energy and we will define the effective mass of the $p-N$ system as

$$m^*_{pN} = m_p + m_N + e_{pN}. \tag{B.2}$$

We now define the Mandelstam variable s as

$$s = (\mathfrak{p}_p + \mathfrak{p}_A)^2, \tag{B.3}$$

the square of the sum of the four-momentum of the proton and the target. We note that, as this quantity is built out of Lorentz invariants (the four-momenta), it is conserved in all reference frames. Its computation in the

laboratory frame yields:

$$s = (m_p + m_A)^2 + 2m_A T_{\mathrm{LAB}}. \tag{B.4}$$

It is possible to express the momentum (or the wave number) and energy of proton and target in the center of mass, as a function of s and the rest masses [71, 124]

$$K_{pA} = \frac{1}{\hbar}\frac{\sqrt{(s - m_p^2 - m_A^2)^2 - 4m_p^2 m_A^2}}{2\sqrt{s}} \tag{B.5}$$

$$\epsilon_p = \frac{s + m_p^2 - m_A^2}{2\sqrt{s}} \tag{B.6}$$

$$\epsilon_A = \frac{s + m_A^2 - m_p^2}{2\sqrt{s}}. \tag{B.7}$$

It is easily shown that in the center of mass s corresponds to the square of the total relativistic energy (since the total momentum is 0 in the center of mass). Therefore it is conserved during the reaction, so the final momentum and energy in the center of mass (leading to a certain $p-N$ state with energy e_{pN}) can be computed analogously:

$$K_{n'} = \frac{1}{\hbar}\frac{\sqrt{(s - {m^*_{pN}}^2 - m_C^2)^2 - 4{m^*_{pN}}^2 m_C^2}}{2\sqrt{s}} \tag{B.8}$$

$$\epsilon_{pN} = \frac{s + {m^*_{pN}}^2 - m_C^2}{2\sqrt{s}} \tag{B.9}$$

$$\epsilon_C = \frac{s + m_C^2 - {m^*_{pN}}^2}{2\sqrt{s}}. \tag{B.10}$$

As indicated in Chapter 2 the Transfer to the Continuum formalism produces the cross section to each bin, with energy e_{pN} which can be transformed into a differential cross section on e_{pN} through Eq. (2.39). However, our experimental observable of interest is the distribution for the outgoing core, which can be obtained trivially through Eq. (B.10),

$$\frac{\mathrm{d}\sigma}{\mathrm{d}\epsilon_C} = \frac{\mathrm{d}\sigma}{\mathrm{d}e_{pN}}\left|\frac{\partial e_{pN}}{\partial m^*_{pN}}\frac{\partial m^*_{pN}}{\partial \epsilon_C}\right| = \frac{\mathrm{d}\sigma}{\mathrm{d}e_{pN}} \cdot 1 \cdot \frac{\sqrt{s}}{m^*_{pN}}, \tag{B.11}$$

leading to Eq. (2.52). From the double differential cross section on energy

and angle it is trivial to obtain the momentum distribution through the expression of the relativistic energy:

$$\epsilon_C = \sqrt{m_C^2 + p_C^2} \tag{B.12}$$

$$\frac{\mathrm{d}\sigma}{\mathrm{d}^3\mathbf{p}_C} = \frac{\mathrm{d}\sigma}{\mathrm{d}\epsilon_C \mathrm{d}\Omega_C} \left| \frac{\mathrm{d}p_C \mathrm{d}\Omega_C}{\mathrm{d}^3\mathbf{p}_C} \frac{\mathrm{d}\epsilon_C}{\mathrm{d}p_C} \right| = \frac{\mathrm{d}\sigma}{\mathrm{d}\epsilon_C \mathrm{d}\Omega_C} \frac{1}{p_C^2} \frac{p_C}{\epsilon_C} = \frac{1}{p_C \epsilon_C} \frac{\mathrm{d}\sigma}{\mathrm{d}\epsilon_C \mathrm{d}\Omega_C}. \tag{B.13}$$

Appendix C

Reid93 potential

In this appendix, a brief description of the Reid93 potential [74], used as the $p-N$ interaction in most of the calculations in this work, is presented.

The Reid93 parametrization is based on the Reid68 [75] one, which describes the nucleon-nucleon interaction as composed of three terms: central, spin-orbit and tensor, whose radial shapes depend on the nucleon-nucleon configuration $\alpha = \mathbf{L}, \mathbf{S}, \mathbf{J}$, with $\mathbf{L}$ being the orbital angular momentum between the nucleons, $\mathbf{S}$ their total spin $\mathbf{S} = \mathbf{s}_1 + \mathbf{s}_2$ and J the total angular momentum:

$$V_{alpha} = V_C^{\alpha}(r) + V_T^{\alpha}(r)\mathbf{S}_{12} + V_{LS}^{\alpha}(r)\mathbf{L}\cdot\mathbf{S}, \tag{C.1}$$

where $\mathbf{S}_{12}$ is the usual tensor operator:

$$\mathbf{S}_{12} = 3(\sigma_1\cdot\hat{r})(\sigma_2\cdot\hat{r}) - (\sigma_1\cdot\sigma_2). \tag{C.2}$$

The radial shapes were taken as sums of Yukawians ($V(r) = V_0 e^{-\mu r}/r$) and their derivatives, taking μ as integer multiples of the value corresponding to the pion mass $\mu \sim n\cdot 0.7$ fm^{-1}. The Reid68 potential was adjusted for the existing phase-shift data for $J \leq 2$ and E<350 MeV to avoid pion production and other relativistic effects.

The data was reasonably precise for $p-p$ scattering but rather poor for $p-n$ scattering. As such, the advent of new more abundant and precise $p-n$ data required a revision of the Reid68 to better describe it.

This revision led to the Reid93 parametrization, which we use in this work. In it, as in the Reid68 one, the potential considers only central, spin-

orbit and tensor terms. However for its radial shape it uses sums of regularized Yukawians for the central part, in order to avoid singularities near the origin:

$$V_C^\alpha(r) = \sum_\mu V_C^\mu \phi_C^{0\mu} = \sum_\mu V_C^\mu \frac{e^{-\mu r} - e^{-\Lambda r}\left(1 + \frac{\Lambda^2-\mu^2}{2\Lambda^2}\Lambda r\right)}{\mu r}, \tag{C.3}$$

while the tensor and spin-orbit terms are taken as the derivatives of the shapes for the central part

$$V_T^\alpha(r) = \sum_\mu V_T^\mu \phi_T^{0\mu}(r) = \sum_\mu V_T^\mu \frac{1}{3\mu^2} r \frac{\mathrm{d}}{\mathrm{d}r}\left(\frac{1}{r}\frac{\mathrm{d}}{\mathrm{d}r}\right)\phi_C^{0\mu}(r) \tag{C.4}$$

$$V_{LS}^\alpha(r) = \sum_\mu V_{LS}^\mu \phi_{LS}^{0\mu}(r) = \sum_\mu V_{LS}^\mu - \frac{1}{\mu^2 r}\frac{\mathrm{d}}{\mathrm{d}r}\phi_C^{0\mu}(r). \tag{C.5}$$

As before, the values of μ are taken as integer multiples of the value corresponding of the pion mass, although for this parametrization it is taken as the average mass of the neutral and charged pions:

$$\bar{m} = \frac{1}{3}(m_{\pi^0} + 2m_{\pi^\pm}), \tag{C.6}$$

while the cutoff parameter is taken as $\Lambda = 8\bar{m}$. For all nucleon-nucleon configurations, the potential is separated in a one-pion-exchange (OPE) part and a non-OPE part. The OPE potential is taken as

$$V_{OPE}(pp) = f_\pi^2 V(m_{\pi^0}) \tag{C.7}$$

$$V_{OPE}(pn) = -f_\pi^2 V(m_{\pi^0}) \pm 2 f_\pi^2 V(m_{\pi^\pm}), \tag{C.8}$$

different for $p-p$ and $p-n$ scattering and where:

$$V(m) = \left(\frac{m}{m_{\pi^\pm}}\right)^2 m[\phi_T^{0\mu}(r)\mathbf{S}_{12} + \frac{1}{3}(\phi_C^{0\mu} - 4\pi\delta^3(\mu\mathbf{r}))(\sigma_1 \cdot \sigma_2)], \tag{C.9}$$

while the non-OPE part is fitted through a sum of the regularized Yukawians and their derivatives. The parameters for the potential (50 independent ones) were fitted to $p-p$ and $p-n$ data up to 350 MeV, using the same parameters for all waves with $J \geq 5$, obtaining a very successful fit with a value of $\chi^2/N = 1.03$. The resulting parameters are not presented here but can be

found in [74].

In the implementation of the Reid93 potential in code FRESCO [67], we face a difficulty: FRESCO describes states in a $j-j$ coupling scheme, $[[L, s_1]j_1, s_2]J$. As such, $S = s_1 + s_2$ is not a good quantum number in this scheme, so the implementation of the Reid93 interaction (in which potentials depend on S) cannot be performed directly. Instead we modify the central potential and include a spin-spin term in the potential (which is allowed as an input by FRESCO), which is built according to the following set of equations:

$$V_{S=0} = V_C + V_{ss} \langle S = 0 | s_1 \cdot s_2 | S = 0 \rangle \tag{C.10}$$

$$V_{S=1} = V_C + V_{ss} \langle S = 1 | s_1 \cdot s_2 | S = 1 \rangle \tag{C.11}$$

The matrix element can be computed in a similar way to the spin-orbit terms

$$s_1 \cdot s_2 = \frac{S^2 - s_1^2 - s_2^2}{2}, \tag{C.12}$$

thus yielding:

$$V_{S=0} = V_C - \frac{3}{4} V_{ss} \tag{C.13}$$

$$V_{S=1} = V_C + \frac{1}{4} V_{ss}, \tag{C.14}$$

which leads trivially to

$$V_C = \frac{1}{4} V_{S=0} + \frac{3}{4} V_{S=1} \tag{C.15}$$

$$V_{ss} = V_{S=1} - V_{S=0}. \tag{C.16}$$

As a test of the implementation of the Reid93 interaction in FRESCO we have computed the phase-shifts for various waves of the $p-n$ and $p-p$ systems, and compared them with the ones provided by the Nijmegen webiste [125], with the results being shown in Fig. C.1 for $p-n$ phase-shifts and Fig. C.2 for $p-p$ phase-shifts. As can be seen in both figures, the agreement is excellent, which validates our implementation of the Reid93 potential in FRESCO.

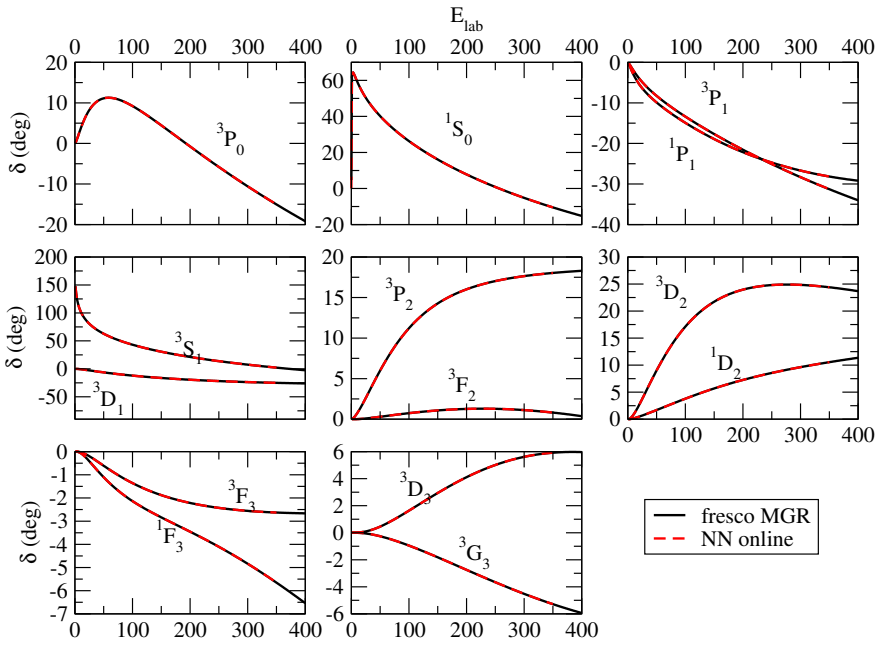

Figure C.1: Phase-shifts for the $p-n$ system for various configurations as a function of laboratory energy. In black solid, the results of our calculations with FRESCO are compared to the results from [125] in red dashed.

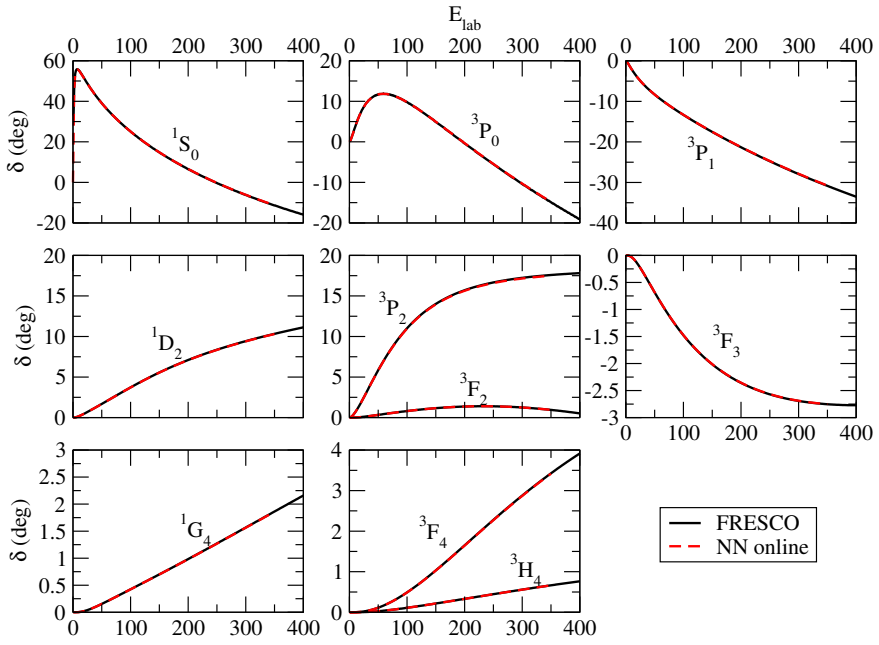

Figure C.2: Phase-shifts for the $p-p$ system for various configurations as a function of laboratory energy. In black solid, the results of our calculations with FRESCO are compared to the results from [125] in red dashed.

Bibliography

[1] M. G. Mayer, Phys. Rev. **75**, 1969 (1949).

[2] E. O. Wiig, Journal of the American Chemical Society **78**, 508 (1956).

[3] A. M. Moro, Phys. Rev. C **92**, 044605 (2015).

[4] C. A. Bertulani and C. De Conti, Phys. Rev. C **81**, 064603 (2010).

[5] T. de Forest Jr. and J. Walecka, Advances in Physics **15**, 1 (1966).

[6] G. JACOB and T. A. J. MARIS, Rev. Mod. Phys. **45**, 6 (1973).

[7] Y. Yasuda *et al.*, Phys. Rev. C **81**, 044315 (2010).

[8] L. Lapikás, Nuclear Physics A **553**, 297 (1993).

[9] W. Dickhoff and C. Barbieri, Progress in Particle and Nuclear Physics **52**, 377 (2004).

[10] B. P. Kay, J. P. Schiffer, and S. J. Freeman, Phys. Rev. Lett. **111**, 042502 (2013).

[11] A. A. Cowley, J. J. Lawrie, G. C. Hillhouse, D. M. Whittal, S. V. Förtsch, J. V. Pilcher, F. D. Smit, and P. G. Roos, Phys. Rev. C **44**, 329 (1991).

[12] O. Benhar, A. Fabrocini, and S. Fantoni, Phys. Rev. C **41**, R24 (1990).

[13] T. Wakasa, K. Ogata, and T. Noro, Progress in Particle and Nuclear Physics **96**, 32 (2017).

[14] S. Cohen and D. Kurath, Nuclear Physics **73**, 1 (1965).

[15] E. K. Warburton and B. A. Brown, Phys. Rev. C **46**, 923 (1992).

[16] B. A. Brown and W. A. Richter, Phys. Rev. C **74**, 034315 (2006).

[17] M. J. W. S. French J.B., Halbert E.C., in *Advances in Nuclear Physics*, edited by V. E. Baranger M. (Springer, Boston, 1969) pp. 193–259.

[18] A. Etchegoyen, W. D. Rae, N. S. Godwin, W. A. Richter, C. H. Zimmerman, B. A. Brown, W. E. Ormand, and J. S. Winfield, MSU-NSCL Report (1985).

[19] E. Caurier and F. Nowacki, Acta Phys. Pol. B **30**, 705 (1999).

[20] S. Okubo, Progress of Theoretical Physics **12**, 603 (1954).

[21] S. K. Bogner, R. J. Furnstahl, and R. J. Perry, Phys. Rev. C **75**, 061001 (2007).

[22] B. R. Barrett, P. NavrÃ¡til, and J. P. Vary, Progress in Particle and Nuclear Physics **69**, 131 (2013).

[23] L. Atar *et al.* (R^3B Collaboration), Phys. Rev. Lett. **120**, 052501 (2018).

[24] G. Hagen, M. Hjorth-Jensen, and N. Michel, Phys. Rev. C **73**, 064307 (2006).

[25] I. Hamamoto and S. Shimoura, Journal of Physics G: Nuclear and Particle Physics **34**, 2715 (2007).

[26] Y. Urata, K. Hagino, and H. Sagawa, Phys. Rev. C **83**, 041303 (2011).

[27] A. Bohr and B. R. Mottelson, *Nuclear Structure* (World Scientific Publishing, 1998).

[28] S. Fortier *et al.*, Physics Letters B **461**, 22 (1999).

[29] P. Hansen and J. Tostevin, Annual Review of Nuclear and Particle Science **53**, 219 (2003).

[30] J. Tostevin, Nuclear Physics A **682**, 320 (2001).

[31] A. Gade *et al.*, Phys.Rev. C **77**, 044306 (2008).

[32] J. A. Tostevin and A. Gade, Phys. Rev. C **90**, 057602 (2014).

[33] J. Lee *et al.*, Phys. Rev. Lett. **104**, 112701 (2010).

[34] R. C. Johnson and P. J. R. Soper, Phys. Rev. C **1**, 976 (1970).

[35] R. Johnson and P. Tandy, Nuclear Physics A **235**, 56 (1974).

[36] J. Lee, J. A. Tostevin, B. A. Brown, F. Delaunay, W. G. Lynch, M. J. Saelim, and M. B. Tsang, Phys. Rev. C **73**, 044608 (2006).

[37] F. Flavigny *et al.*, Phys. Rev. Lett. **110**, 122503 (2013).

[38] M. Kawai, M. Kamimura, and K. Takesako, Progress of Theoretical Physics Supplement **89**, 118 (1986).

[39] T. Ohmura, B. Imanishi, M. Ichimura, and M. Kawai, Progress of Theoretical Physics **43**, 347 (1970).

[40] F. Flavigny, N. Keeley, A. Gillibert, and A. Obertelli, Phys. Rev. C **97**, 034601 (2018).

[41] F. M. Nunes, A. Deltuva, and J. Hong, Phys. Rev. C **83**, 034610 (2011).

[42] V. Panin *et al.*, Physics Letters B **753**, 204 (2016).

[43] P. Díaz Fernández *et al.* (R^3B Collaboration), Phys. Rev. C **97**, 024311 (2018).

[44] S. Kawase *et al.*, Progress of Theoretical and Experimental Physics **2018**, 021D01 (2018).

[45] S. Hama, B. C. Clark, E. D. Cooper, H. S. Sherif, and R. L. Mercer, Phys. Rev. C **41**, 2737 (1990).

[46] E. D. Cooper, S. Hama, B. C. Clark, and R. L. Mercer, Phys. Rev. C **47**, 297 (1993).

[47] K. Amos, P. Dortmans, H. von Geramb, S. Karataglidis, and J. Raynal, in *Advances in Nuclear Physics*, edited by V. E. Negele J.W. (Springer, Boston, 2002) pp. 276–536.

[48] J. Caballero, T. Donnelly, E. M. de Guerra, and J. UdÃas, Nuclear Physics A **632**, 323 (1998).

[49] K. Yoshida, M. Gómez-Ramos, K. Ogata, and A. M. Moro, Phys. Rev. C **97**, 024608 (2018).

[50] K. Ogata, K. Yoshida, and K. Minomo, Phys. Rev. C **92**, 034616 (2015).

[51] R. Glauber and G. Matthiae, Nuclear Physics B **21**, 135 (1970).

[52] T. Aumann, C. A. Bertulani, and J. Ryckebusch, Phys. Rev. C **88**, 064610 (2013).

[53] L. D. Faddeev, Zh. Eksp. Teor. Fiz. **39**, 1459 (1960), [Sov. Phys. JETP **12**, 1014 (1961)].

[54] E. Alt, P. Grassberger, and W. Sandhas, Nuclear Physics B **2**, 167 (1967).

[55] W. Glöckle, *The Quantum Mechanical Few-Body Problem* (Springer, 1983).

[56] E. Cravo, R. Crespo, and A. Deltuva, Phys. Rev. C **87**, 034612 (2013).

[57] E. Cravo, R. Crespo, and A. Deltuva, Phys. Rev. C **93**, 054612 (2016).

[58] A. M. Moro and F. M. Nunes, Nuclear Physics A **767**, 138 (2006).

[59] A. M. Moro, R. Crespo, H. García-Martínez, E. F. Aguilera, E. Martínez-Quiroz, J. Gómez-Camacho, and F. M. Nunes, Phys. Rev. C **68**, 034614 (2003).

[60] E. Nielsen, D. Fedorov, A. Jensen, and E. Garrido, Physics Reports **347**, 373 (2001).

[61] N. Austern, Y. Iseri, M. Kamimura, M. Kawai, G. Rawitscher, and M. Yahiro, Phys. Rep. **154**, 125 (1987).

[62] I. J. Thompson and F. M. Nunes, *Nuclear Reactions for Astrophysics* (Cambridge University Press, 2009).

[63] O. I. Tolstikhin, V. N. Ostrovsky, and H. Nakamura, Phys. Rev. Lett. **79**, 2026 (1997).

[64] T. Matsumoto, T. Kamizato, K. Ogata, Y. Iseri, E. Hiyama, M. Kamimura, and M. Yahiro, Phys. Rev. C **68**, 064607 (2003).

[65] M. Rodríguez-Gallardo, J. M. Arias, and J. Gómez-Camacho, Phys. Rev. C **69**, 034308 (2004).

[66] A. M. Moro, J. M. Arias, J. Gómez-Camacho, and F. Pérez-Bernal, Phys. Rev. C **80**, 054605 (2009).

[67] I. J. Thompson, Comp. Phys. Rep. **7**, 167 (1988).

[68] T. Sawada and K. Thushima, Progress of Theoretical Physics **76**, 440 (1986).

[69] L. Ray, G. Hoffmann, and W. Coker, Physics Reports **212**, 223 (1992).

[70] A. Nadasen, P. Schwandt, P. P. Singh, W. W. Jacobs, A. D. Bacher, P. T. Debevec, M. D. Kaitchuck, and J. T. Meek, Phys. Rev. C **23**, 1023 (1981).

[71] C. Joachaim, *Quantum Collision Theory* (North Holland Publishing Company, 1975).

[72] G. R. Satchler, *Direct Nuclear Reactions* (Clarendon Press, Oxford, 1983).

[73] P. G. Hansen, Phys. Rev. Lett. **77**, 1016 (1996).

[74] V. G. J. Stoks, R. A. M. Klomp, C. P. F. Terheggen, and J. J. de Swart, Phys. Rev. C **49**, 2950 (1994).

[75] R. V. Reid, Annals of Physics **50**, 411 (1968).

[76] A. Koning and J. Delaroche, Nuclear Physics A **713**, 231 (2003).

[77] R. Machleidt, Phys. Rev. C **63**, 024001 (2001).

[78] F. Nunes, I. Thompson, and R. Johnson, Nuclear Physics A **596**, 171 (1996).

[79] Y. Kondo *et al.*, Phys. Rev. C **79**, 014602 (2009).

[80] J.-P. Jeukenne, A. Lejeune, and C. Mahaux, Phys. Rev. C **16**, 80 (1977).

[81] R. Malfliet and J. Tjon, Nuclear Physics A **127**, 161 (1969).

[82] A. E. L. Dieperink and T. d. Forest, Phys. Rev. C **10**, 543 (1974).

[83] H. An and C. Cai, Phys. Rev. C **73**, 054605 (2006).

[84] A. Ozawa *et al.*, Phys. Rev. C **84**, 064315 (2011).

[85] Y. Satou *et al.*, Physics Letters B **660**, 320 (2008).

[86] Z. Elekes *et al.*, Physics Letters B **614**, 174 (2005).

[87] N. Kobayashi *et al.*, Phys. Rev. C **86**, 054604 (2012).

[88] M. Thoennessen *et al.*, Nuclear Physics A **912**, 1 (2013).

[89] Z. Vajta *et al.*, Phys. Rev. C **91**, 064315 (2015).

[90] J. A. Lay, R. de Diego, R. Crespo, A. M. Moro, J. M. Arias, and R. C. Johnson, Phys. Rev. C **94**, 021602 (2016).

[91] Hwang, Jongwon *et al.*, EPJ Web of Conferences **113**, 06014 (2016).

[92] J. A. Lay, A. M. Moro, J. M. Arias, and Y. Kanada-En'yo, Phys. Rev. C **89**, 014333 (2014).

[93] B. Alex Brown, Phys. Rev. C **58**, 220 (1998).

[94] H. Von Geramb and K. Nakano, in *AIP Conf. Proc*, Vol. 97 (1983) p. 44.

[95] L. Rikus, K. Nakano, and H. V. Von Geramb, Nucl. Phys. A **414**, 413 (1984).

[96] J. J. Kelly, LEA code, University of Maryland (unpublished) .

[97] H. O. Meyer *et al.*, Phys. Rev. C **31**, 1569 (1985).

[98] A. Okamoto *et al.*, Phys. Rev. C **81**, 054604 (2010).

[99] K. W. Jones *et al.*, Phys. Rev. **C33**, 17 (1986).

[100] A. Cipollone, C. Barbieri, and P. Navrátil, Phys. Rev. C **92**, 014306 (2015).

[101] M. Zhukov, B. Danilin, D. Fedorov, J. Bang, I. Thompson, and J. Vaagen, Physics Reports **231**, 151 (1993).

[102] I. Tanihata, H. Hamagaki, O. Hashimoto, Y. Shida, N. Yoshikawa, K. Sugimoto, O. Yamakawa, T. Kobayashi, and N. Takahashi, Phys. Rev. Lett. **55**, 2676 (1985).

[103] H. Simon *et al.*, Phys. Rev. Lett. **83**, 496 (1999).

[104] Fortune, H. T., Eur. Phys. J. A **54**, 51 (2018).

[105] H. Bohlen, W. von Oertzen, T. Stolla, R. Kalpakchieva, B. Gebauer, M. Wilpert, T. Wilpert, A. Ostrowski, S. Grimes, and T. Massey, Nuclear Physics A **616**, 254 (1997), radioactive Nuclear Beams.

[106] J. A. Caggiano, D. Bazin, W. Benenson, B. Davids, B. M. Sherrill, M. Steiner, J. Yurkon, A. F. Zeller, and B. Blank, Phys. Rev. C **60**, 064322 (1999).

[107] M. Thoennessen, S. Yokoyama, A. Azhari, T. Baumann, J. A. Brown, A. Galonsky, P. G. Hansen, J. H. Kelley, R. A. Kryger, E. Ramakrishnan, and P. Thirolf, Phys. Rev. C **59**, 111 (1999).

[108] M. Chartier, J. Beene, B. Blank, L. Chen, A. Galonsky, N. Gan, K. Govaert, P. Hansen, J. Kruse, V. Maddalena, M. Thoennessen, and R. Varner, Physics Letters B **510**, 24 (2001).

[109] P. Santi *et al.*, Phys. Rev. C **67**, 024606 (2003).

[110] H. Jeppesen *et al.*, Physics Letters B **642**, 449 (2006).

[111] J. Smith, T. Baumann, J. Brown, P. DeYoung, N. Frank, J. Hinnefeld, Z. Kohley, B. Luther, B. Marks, A. Spyrou, S. Stephenson, M. Thoennessen, and S. Williams, Nuclear Physics A **940**, 235 (2015).

[112] A. Sanetullaev *et al.*, Physics Letters B **755**, 481 (2016).

[113] D. Gogny, P. Pires, and R. D. Tourreil, Physics Letters B **32**, 591 (1970).

[114] I. J. Thompson and M. V. Zhukov, Phys. Rev. C **49**, 1904 (1994).

[115] E. Garrido, D. V. Fedorov, and A. S. Jensen, Phys. Rev. C **68**, 014002 (2003).

[116] I. J. Thompson, B. V. Danilin, V. D. Efros, J. S. Vaagen, J. M. Bang, and M. V. Zhukov, Phys. Rev. C **61**, 024318 (2000).

[117] E. Garrido, D. Fedorov, and A. Jensen, Nuclear Physics A **617**, 153 (1997).

[118] Y. Aksyutina *et al.*, Physics Letters B **666**, 430 (2008).

[119] G. F. Bertsch, K. Hencken, and H. Esbensen, Phys. Rev. C **57**, 1366 (1998).

[120] M. Gómez-Ramos, J. Casal, and A. Moro, Physics Letters B **772**, 115 (2017).

[121] H. Simon *et al.*, Nuclear Physics A **791**, 267 (2007).

[122] R. Kanungo *et al.*, Phys. Rev. Lett. **114**, 192502 (2015).

[123] J. Casal, M. Gómez-Ramos, and A. Moro, Physics Letters B **767**, 307 (2017).

[124] R. Hagedorn, *Relativistic Kinematics: A guide to the kinematic problems of high-energy physics* (W. A. Benjamin, INC., 1963).

[125] "Nn-online," `http://nn-online.org/`, accessed: 2018-06-15.

Publications, contributions and other research activities

Publications

- Authors: **M. Gómez-Ramos**, A.M. Moro, J. Gómez-Camacho and I.J. Thompson
  Title: *Transfer induced by core excitation within an extended distorted-wave Born approximation method*
  Reference: Physical Review C **92** (2015) 014613.
  Article

- Authors: **M. Gómez-Ramos** and A.M. Moro
  Title: *Transfer to the continuum calculations of quasifree* (p, pn) *and* $(p, 2p)$ *reactions at intermediate and high energies*
  Conference: Basic Concepts in Nuclear Physics: Theory, Experiments and Applications: 2015 La Rábida International Scientific Meeting on Nuclear Physics
  Reference: Springer Proceedings in Physics **182** (2016) 171.
  Proceeding

- Authors: **M. Gómez-Ramos** and A.M. Moro
  Title: *Transfer to the continuum calculations of quasifree* (p, pn) *and* $(p, 2p)$ *reactions*
  Conference: 12th International Conference on Nucleus-Nucleus Collisions 2015, EPJ Web of Conferences
  Reference: Italian Physical Society **117** (2016) 06024.
  Proceeding

- Authors: A.M. Moro, J. Lei,**M. Gómez-Ramos**, J.M. Arias, R. de

Diego, J. Gómez-Camacho and J.A. Lay
TITLE: *Recent Developments for the Calculation of Elastic and Non-elastic Breakup of Weakly-bound Nuclei*
REFERENCE: Acta Physica Polonica B **47** (2016) 821.
ARTICLE

- AUTHORS: **M. Gómez-Ramos** and A.M. Moro
  TITLE: *Interplay of projectile breakup and target excitation in reactions induced by weakly bound nuclei*
  REFERENCE: Physical Review C **95** (2017) 034609.
  ARTICLE

- AUTHORS: **M. Gómez-Ramos** and A.M. Moro
  TITLE: *Influence of target deformation and deuteron breakup in* (d, p) *transfer reactions*
  REFERENCE: Physical Review C **95** (2017) 044612.
  ARTICLE

- AUTHORS: J. Casal, **M. Gómez-Ramos** and A.M. Moro
  TITLE: *Description of the* $^{11}Li(p, d)^{10}Li$ *transfer reaction using structure overlaps from a full three-body model*
  REFERENCE: Physics Letters B **767** (2017) 307.
  ARTICLE

- AUTHORS: **M. Gómez-Ramos**, J. Casal and A.M. Moro
  TITLE: *Linking structure and dynamics in* (p, pn) *reactions with Borromean nuclei: The* $^{11}Li(p, pn)^{10}Li$ *case*
  REFERENCE: Physics Letters B **772** (2017) 115.
  ARTICLE

- AUTHORS: K. Yoshida,**M. Gómez-Ramos**, K. Ogata and A.M. Moro
  TITLE: *Benchmarking theoretical formalisms for* (p, pn) *reactions: The* $^{15}C(p, pn)^{14}C$ *case*
  REFERENCE: Physical Review C **97** (2018) 024608.
  ARTICLE

- AUTHORS: **M. Gómez-Ramos** and A.M. Moro
  TITLE: *Binding-energy independence of reduced spectroscopic strengths derived from* $(p, 2p)$ *and* (p, pn) *reactions with nitrogen and oxygen*

isotopes
Reference: Physics Letters B (2018) Submitted.
Article

- Authors: **M. Gómez-Ramos** and N. Timofeyuk
  Title: *Reduced sensitivity of the (d, p) cross sections to the deuteron model beyond adiabatic approximation*
  Reference: Physical Review C (2018) Submitted.
  Article

Contributions to conferences

- Authors: **M. Gómez-Ramos** and A.M. Moro
  Title: *Dynamical effects for thransfer reactions in the DWBA approximation*
  Conference: Euroschool on Exotic Beams 2014
  Place: Padova, Italy
  Date: 7 September 2014, Poster

- Authors: **M. Gómez-Ramos** and A.M. Moro
  Title: *Scattering and structure of quantum systems within few-body models*
  Conference: Complex Systems: from the Nanoscale to the Continuum (CS:N2C)
  Place: Münster, Germany
  Date: 10 February 2015, Talk

- Authors: **M. Gómez-Ramos** and A.M. Moro
  Title: *Transfer to the continuum calculations of quasifree (p, pn) and $(p, 2p)$ reactions at intermediate and high energies*
  Conference: International Scientific Meeting on Nuclear Physics (RABIDA15), "Basic concepts in Nuclear Physics: theory, experiments and applications"
  Place: La Rábida (Huelva), Spain
  Date: 1 June 2015, Talk

- Authors: **M. Gómez-Ramos** and A.M. Moro
  Title: *Transfer to the continuum calculations of quasifree (p, pn) and*

$(p, 2p)$ *reactions*
Conference: 12th International Conference on Nucleus-Nucleus collisions (NN2015)
Place: Catania, Italy
Date: 21-26 June 2015, Poster

- Authors: **M. Gómez-Ramos** and A.M. Moro
  Title: *Transfer to the continuum calculations of* (p, pN) *reactions*
  Conference: Direct Reactions on Exotic Beams 2016 (DREB2016)
  Place: Halifax, Canada
  Date: 11 Jul 2016, Talk

- Authors: **M. Gómez-Ramos** and A.M. Moro
  Title: *Interplay between breakup of weakly bound nuclei and collective excitations*
  Conference: Direct Reactions on Exotic Beams 2016 (DREB2016)
  Place: Halifax, Canada
  Date: 11 Jul 2016, Poster

- Authors: **M. Gómez-Ramos** and A.M. Moro
  Title: *Transfer to the continuum calculations for* (p, pN) *and transfer reactions on Borromean nuclei*
  Conference: XXXVI Reunión Bienal de la Real Sociedad Española de Física
  Place: Santiago de Compostela, Spain
  Date: 17 Jul 2017, Talk

- Authors: **M. Gómez-Ramos** and A.M. Moro
  Title: *Transfer to the continuum calculations of* (p, pn) *and* $(p, 2p)$ *reactions at intermediate and high energies*
  Conference: 3^{rd} International Workshop on Quasifree Scattering with Radioactive-Ion Beams (QFS-RB 17)
  Place: York, United Kingdom
  Date: 24 Jul 2017, Talk

- Authors: **M. Gómez-Ramos**, J. Casal and A.M. Moro
  Title: *Transfer to the continuum calculations of* (p, pN) *reactions on Borromean nuclei*
  Conference: 5^{th} UK Nuclear Theory Meeting

Place: York, United Kingdom
Date: 2 Nov 2017, Talk

- Authors: **M. Gómez-Ramos** and A.M. Moro
  Title: *Study of "quenching factors" for (p, pn) and $(p, 2p)$ reactions through the Transfer to the Continuum formalism*
  Conference: Recent advances and challenges in the description of nuclear reactions at the limit of stability
  Place: Trento, Italy
  Date: 5 Mar 2018, Talk

- Authors: **M. Gómez-Ramos** and A.M. Moro
  Title: *Analysis of isospin dependence of "quenching factors" for (p, pn) and $(p, 2p)$ reactions via the Transfer to the Continuum formalism*
  Conference: Direct Reactions on Exotic Beams 2018 (DREB2018)
  Place: Matsue, Japan
  Date: 4 Jun 2018, Talk

Research stays

- Research Center on Nuclear Physics (RCNP), University of Osaka
  Osaka, Japan
  Duration: 39 days
  Period: January 31 to March 10, 2017
  Supervisor: K. Ogata, Associate Professor

- Center for Nuclear and Radiation Physics, University of Surrey
  Guildford, United Kingdom.
  Duration: 56 days
  Period: October 8 to December 3, 2017
  Supervisor: N. Timofeyuk, Senior Research Fellow

Seminars

- "Transfer to the Continuum calculations of (p, pN) reactions at intermediate and high energies", Dpto. FAMN, Universidad de Sevilla, June

12, 2015.

- "Transfer to the Continuum calculations for (p, pN) reactions. Application to Borromean nuclei", Research Center for Nuclear Physics Osaka (RCNP), February 27, 2017.
- "Probing the structure of Borromean nuclei through (p, pN) reactions", University of Surrey, October 10, 2017.

Courses

- Symmetries in Quantum Physics: Group theory for Physicists, Sevilla, Spain, April 7-April 15, 2015.
- Física y Matemáticas: Dos caras de una misma moneda, Sevilla, Spain, June 29-July 10, 2015.
- ECT* TALENT School: Few-body Methods and Nuclear Reactions, ECT*, Trento, Italy, July 20-August 7, 2015.
- HPC (high performance computing) course, Universidad de Sevilla, Sevilla, Spain, October 21-December 16, 2015.
- Frontiers in Nuclear and Hadronic Physics, Florence, Italy, February 22-March 4, 2016.